University of Alberta

Ultrasonic Imaging and Cortical Thickness Determination of Long Bones

by

Rui Zheng

A thesis submitted to the Faculty of Graduate Studies and Research
in partial fulfillment of the requirements for the degree of

Doctor of Philosophy

Department of Physics & Department of Biomedical Engineering

Fall 2011
Edmonton, Alberta

To my respected father and beloved mother,

Yuqi and Shuzhen,

for your trust and support.

Abstract

Osteoporosis is a bone disease characterized by the degradation of mechanical competence and support of the skeleton, leading to fracture risk of the wrist, vertebrae, and hip. The disease is due to major decrease of mass and deterioration of micro-structure of bone tissues.

In this study, bone imaging methodologies are developed to image the internal structure of long bones and to estimate particularly the top cortical thickness using zero-offset data acquired on the bone surface. The inversion algorithm, which requires a background velocity model, is based on Born scattering theory implemented with conjugate gradient iterative method to seek an optimal solution. In case the velocity model is multilayered, ray tracing through a smooth medium will be used to calculate the travelled distance and travelling time. Using the simulated data, the forward and adjoint operators of the inversion method are validated for its feasibility, accuracy, and quality of the reconstructed images. The values of some inversion variables, such as frequency range, frequency sampling rate, beam aperture, source wavelet, noise level, temporal sampling interval, pixel size, spacing interval of acquisition, and inversion regularization, are also investigated to optimize the quality of the reconstructed

images.

To image the top cortical layer, a good estimate of the background velocity can be obtained by linear regression method using the offset axial transmission data. The inversion algorithm is applied to image four real bone samples *in vitro*. The results demonstrate the top cortical interfaces can be reconstructed and correspond favorably to the CT image. The measurements show the sectional mean thickness (SMT) is a better and robust estimate for the average thickness of the cortex. The thicknesses of the bovine, cervine and ovine samples are 5, 4 and 3 mm, respectively, which correspond to absolute errors of 1.9%, 4.6% and 3.2% in comparison with the CT images.

Due to the tissue absorption, interface curvature, and local heterogeneities, imaging the other interfaces was less successful. However, the current imaging method has successfully recovered the top cortical layer, offering a potential diagnostic tool to estimate cortical thinning for osteoporosis assessment.

Acknowledgments

I would like to thank my supervisor Dr. Lawrence H. Le for the kind support, patience and encouragement. I am deeply appreciated for his valuable and professional guidance during my PhD study and research. I learned a great deal of knowledge, experiences and skills from him, and they will all be the most important fortunes in my future research career.

I would like to thank my co-supervisor Dr. Mauricio D Sacchi. His plentiful knowledge and experience in the seismic imaging guided me to complete the fundamental and theoretical part of my thesis. I am appreciated for Dr. Edmond Lou for his generous help during my graduate study and research.

I would like to thank Alberta Ingenuity Fund for its financial support during my PhD study over the years. I would like to thank Alberta Provincial CIHR Training Program in Bone and Joint Health for the travel allowance support. I would like to thank Department of Physics, Department of Biomedical Engineering and Department of Radiology and Diagnostic Imaging for all the financial assistance during my graduate study.

I also want to thank Drs. Dean Ta and Yuanyuan Wang of Fudan University for the scientific discussion and the opportunity to visit Fudan University, Shanghai.

I am very grateful for all my friends and colleagues, Luning, Chan, Peng, Wei, Hongjiang, Lauren, Ken, Dr. Junhua Zhang, Mary Lou and many other people, for the wonderful time we were together in the laboratory.

Table of Contents

List of Tables

List of Figures

Chapter 1

Introduction

Osteoporosis is a major bone disease occurring in the aged population and especially the postmenopausal women. The disease causes bone thinning and brittle bones leading to high risks of skeleton fractures, negatively impacting the quality of patients' life. To diagnose and assess the state of the disease, ultrasonic imaging using long bones are developed in this thesis. This chapter, which serves as an introduction, begins with a review of the bone structure, bone classification, and osteoporosis. This is followed by a description of the commonly used radiological techniques to diagnose osteoporosis. The two conventional measured parameters, bone mineral density (BMD) and cortical thickness (*c*Th), are discussed. Subsequently, clinical ultrasonic assessment of osteoporosis using transverse transmission method is presented. Finally a survey of the current ultrasonic research for bone relevant to osteoporosis is given. This includes the evaluation of micro-structure, estimation of structure, and properties of long bones, and especially ultrasound wave imaging.

1.1 Bone tissues and osteoporosis

Based on structure, bone tissue can be categorized as cortical (compact, dense) bone and cancellous (spongy) bone. Cortical bone forms the outside layer, or cortex of all bones, and the main body of long bones. Its functions are to protect and support. Due to the concentric ring structure, it has greater density and stronger mechanical properties than cancellous bone. Cancellous bone is mainly

located in the short, flat and irregular-shaped bones, and also in the epiphyses of long bones. It has a structure of irregular lattice network, and the thin plates distributed in cancellous bone are the trabeculae, between which is the red marrow filling the space (Tortora and Grabowski, 1993).

Another classification of human bones is based on the bone shape. They are long bones, short bones, flat bones, and irregular bones. Long bones are long and tube-shaped including several typical appendicular parts in human body, such as femur, tibia, humerus, and radius. The middle part of long bones is called shaft and mostly made of cortical bone. Calcaneus (categorized as short bone) and vertebra (categorized as irregular bone) are commonly used for the osteoporosis and scoliosis studies; they both have the internal cancellous structure and the outside cortex (Tortora and Grabowski, 1993).

Osteoporosis is one of the major musculoskeletal diseases related to mass loss, cortical thinning, and deterioration of bone's micro-architecture, ultimately leading to typical fractures of the wrist, vertebrae, and hip (Werner, 2005; Riggs *et al*, 2004). With aging, two major effects will occur on bone tissues: 1) deterioration of bone matrix structures due to loss of calcium and other minerals and 2) loss of elastic strength in bone due to decrease in protein synthesis (Tortora and Grabowski, 1993). Both effects can lead to the loss of bone mass and bone strength respectively. Bone loss during osteoporosis will highly increase the probability of future fracture risk. A decrease of one standard deviation in bone mineral density (BMD) increases the fracture risk by two-fold in a prospective cohort studies (Klotzbuecher *et al*, 2000).

An estimated 75 million people are affected in the Unites states, Europe, and Japan combined (EFFO and NOF, 1997). In Canada, approximately 1 in 4 women and 1 in 8 men have osteoporosis, and in US, the costs have risen to CAD

17-20 billion per year over the past decade (Jacques *et al*, 2002). In Europe, the disability caused by osteoporosis is greater than that by common cancers with the exception of lung cancer. The osteoporotic fracture causes greater loss in life quality than some of the chronic non-communicable diseases such as rheumatoid arthritis, asthma, and high blood pressure related heart diseases (Johnell and Kanis, 2006).

1.2 The conventional clinical indicator for diagnosis of osteoporosis

Bone densitometry is the most common quantitative technique for the measurement of bone mass and density. The measurements can be applied to different skeletal sites, which can be either central or peripheral. The characterization of each site is unique to densitometry. Conventionally central densitometry applied in the central body is capable to measure the spine and proximal femur. The peripheral sites are commonly indicated as distal appendicular sites including the calcaneus, tibia, metacarpals, phalanges, and forearm (Bonnick and Lewis, 2002). X-ray densitometry provides *in vivo* measurement for the bone mineral content (BMC) and bone mineral density (BMD), two important indicators in the clinical diagnosis of osteoporosis. The parameters measure the amount of mineral matter in bone tissue, which can be expressed in gram for BMC or gram per unit length or unit area for BMD (Bonnick and Lewis, 2002; Langton and Njeh, 2004).

The thickness of cortical shell is another important parameter of interest in bone and osteoporosis research. In an experimental study of osteoporosis using rats, Virtama and Kallio (1961) reported the cortical thickness of long bones was apparently reduced after 10-15 percent loss of bone mineral. For human, the cortical thickness measured from radiographs will decrease after the age of 50 as

compared with people of younger ages (between 20-50 years old) due to cortical thinning. By the age of 75, the cortical thickness will experience an average decrease of 39% in females and 18% in males (Evans *et al*, 1978). A high correlation was present between the cortical thickness of proximal bones and the mineral content of the bones (Virtama and Mahonen, 1960; Virtama and Telkka, 1962). In particular, the cortical thickness of proximal diaphysis is highly related to the bone quality; a cortical thickness less than 4 mm in humerus bones will indicate a low BMD (Tingart *et al*, 2003). The reduced cortical thickness will also result in a substantial decrease in stiffness and strength of bone. When the vertebral cortical shell changes from 0.5 mm to 0.2 mm, the stiffness and strength will reduce by 48% and 62% accordingly. Cortical thinning has a greater influence than trabeculae thinning upon the vertebral stiffness and strength in the late stage of osteoporosis (McDonald *et al*, 2009).

In 1960, Barnett and Nordin (1960) introduced the definition of femoral score as an indicator to diagnose osteoporosis. The femoral score is defined as the ratio between the thickness of the thickest cortex and the diameter of the femoral shaft. Bloom (1970 and 1980) demonstrated that the combined cortical thickness (CCT) of the medial and lateral cortices at the lower shaft of the humerus showed the smallest variation in the healthy female populations; therefore, they suggested the site had an advantage in the diagnosis of osteoporosis. Moreover, Virtama and Mahonen (1960) suggested the fraction of cortex area to the total area in the finger bones could provide an objective way to assess the state of osteoporosis. As an improvement of the methodology, Evan *et al* (1978) found that the metacarpal cortical area could be regarded as an index of bone mass. The areal measurement provides greater reproducibility compared with the linear measurement of cortical width. All these methods are various ways to measure cortical thinning. The measurements are simpler, require less expensive equipments, and correlate well

with BMD.

1.3 The current radiological approaches for bone measurements

Currently, there are two main types of techniques for the physical measurement of bone to assess osteoporosis: the ionizing radiation techniques including DEXA (Dual Energy X-ray Absorptiometry), QCT (Quantitative Computed Tomography), and μCT (micro-Computed Tomography), and the non-ionizing techniques including MRI (Magnetic Resonance Imaging) and QUS (Quantitative Ultrasound).

DEXA is the most commonly used clinical method to measure BMD from the lumbar spine, the proximal femur, and the whole body. X-ray absorptiometry is a mature modality and has an outstanding reproducibility. It is able to measure either the areal or the volumetric bone mineral density. The measurements from DEXA are regarded as the gold standard (Bonnick and Lewis, 2002).

Quantitative computed tomography (QCT) can evaluate BMD in trabecular bones in the vertebral bodies with high degree of accuracy and precision but longer scanning time. Micro computed tomography (μCT) was developed to investigate the trabecular microstructure *in vitro* with ultra-high resolution. Magnetic resonance imaging (MRI) is also used to measure trabecular bone and assess skeletal strength but is mainly restricted to *in vitro* studies and the *in vivo* animal studies. (Langton and Njeh, 2004)

Because radiation-based modalities only detect the bone density and are not capable to provide the elastic strength information in bones, they are not very sensitive to the early stage of osteoporosis. It is reported that changes of bone can be detected on radiographs only after approximate 20-40% of skeletal calcium has

been depleted (Castriota-Scanderbeg and Dallapiccola, 2005). Since 1990s, the use of quantitative ultrasound (QUS) in the assessment of skeletal status to assess osteoporosis and predict fracture risk has gained considerable interest (Genant *et al*, 1996; Wuster and Hadji, 2001; Laugier, 2006; Stiffert and Kaufman, 2007).

1.4 Clinical ultrasound in bone and osteoporosis assessment

It was first reported by Langton *et al* (1984) that QUS provided valuable information about bone structure in clinical assessment. Their study showed that broadband ultrasound attenuation (BUA) was significantly different between the healthy subjects and patients with fractured neck of femur.

When ultrasound travels through a bone sample, the recorded signals are influenced by many ultrasonic parameters such as speed of sound (SOS), broadband ultrasound attenuation (BUA), and the internal structure of the bone sample. During the process of osteoporosis, the bone tissue degenerates, the mineral content decreases, the microstructure changes, and the cortical thickness reduces. These will lead to distinct changes of bone structure and mechanical properties, which will affect other macroscopical physical parameters. For example, with the deterioration of the bone structure, the scattering and absorption will be reduced, leading to the decrease of bone attenuation (Funke *et al*, 1995, Langton *et al*, 1984, Nicholson *et al*, 2001, Hakulinen *et al*, 2006). The ultrasound data should reflect such changes that could be identified through the process of ultrasonic wave propagation.

The ultrasonic approach has several practical advantages over traditional radiological techniques such as DEXA, QCT, μCT and MRI. Ultrasound technique is radiation-free, less costly, portable, and easy to use. It has the

potential to measure bone elasticity and assess cancellous microstructure, which are important parameters contributing to the understanding of bone quality and strength.

The conventional technique to measure bone samples is the transverse transmission method (Langton *et al*, 1984; Langton *et al*, 1990). A pair of transducers is co-aligned and submerged in a water tank. Ultrasound travels from one transducer to another. A reference signal is recorded with no bone sample in the path, and the other signal is recorded with the bone sample in between. This technique was widely used to measure speed of sound (SOS) and attenuation (BUA) of bone *in vitro* and *in vivo* (Strelitzki *et al*, 1999; Chaffai *et al*, 2000; Wear, 2000; Jenson *et al*, 2006). Clinically, the measurement is done at the heel or the phalanges, and the transverse transmission technique has been applied to evaluate bone mineral density during routine health examination (Lin *et al*, 2001).

Baran *et al* (1988) found that BUA was remarkably decreased in women with osteoporosis and hip fractures. The BUA measurements in calcaneus showed correlation with BMD at the femoral neck and lumbar spine (Young *et al*, 1993). The normalized broadband ultrasound attenuation, *n*BUA (BUA normalized by thickness) also showed strong correlation with BMD (Jenson *et al*, 2006). The SOS, another measurable quantity, shows better correlation with elastic modulus and strength than the BUA in a study involving 37 bovine trabecular bone samples (Toyras *et al*, 2002). However, reproducibility is a problem because a small difference of measurement location may result in a significant measurement error when using the transverse transmission technique (Chappard *et al*, 1997); therefore a more robust method is necessary to achieve more accurate and precise assessment of bone quality and diagnosis of osteoporosis.

1.5 Current ultrasonic research in bone and osteoporosis study

To improve the assessment of bone quality, three areas have been considered and explored in recent research activities (Laugier, 2006; Nicholson, 2008): 1) the study of micro-structure, micro-architecture, and micro-fracture, 2) the estimation of geometrical structure and acoustic properties of long bones using bulk and guided waves, and 3) ultrasound wave imaging and tomography of long bones.

1.5.1 Study of micro-structure

The transverse transmission method renders a global measurement of the bone samples through which ultrasound propagates. The method lacks the resolution to unfold the micro-structural information of cancellous bones. The understanding of the micro-structural properties of cancellous bone will lead to a more accurate diagnosis and prediction of bone quality.

Ultrasound backscattering provides a means to study the micro-architectures of cancellous bone samples. By analyzing the interaction between ultrasound waves and trabeculae, the ultrasound echoes are used to acquire the structural properties of the trabeculae. The current research literature has demonstrated that there is a strong correlation between the backscatter coefficients from the cancellous framework and micro-structural parameters. Wear (1999) measured 16 human calcaneus trabeculae bone samples and compared with the long thin cylinder model of small radii approximate to the ultrasonic wavelength. Wear found agreement between the experimental results and theory, and the backscatter coefficient was proportional to cubic frequency at lower frequencies near 500 Hz. Chaffa *et al* (2002) studied 15 human calcanei from cadavers with age ranging between 75 and 90 years old and reported that the broadband ultrasound

backscatter (BUB) was strongly correlated with BMD (r = 0.89). Ta *et al* (2005) studied the *in vitro* and *in vivo* data from bovine tibia and human calcaneus. Their study showed that the BSC was a non-linear function of frequency and the data could be explained by a cellular model. Hakulinen *et al* (2006) reported that the BUB shows approximately a linear relationship with the structural properties such as BV/TV (trabecular bone volume fraction), SMI (structural model index, which is related to the predominant shape of trabeculae), TbTh (mean trabecular bone thickness) at the center frequency of 5 MHz.

Using very high-frequency (20 - 400 MHz) focused ultrasound techniques, the scanning acoustic microscope (SAM) can be used to investigate and image the micro-structures of the bone samples, especially cortical samples (Katz and Meunier, 1993; Bumrerraj and Katz, 2001; Hasegawa *et al*, 1994 and 1995; Zimmerman *et al*, 1994; Raum *et al*, 2004). Katz and his associates (Katz and Meunier,1993; Bumrerraj and Katz,2001) used SAM to survey the structure of bone surface and interior and was able to obtain the resolution as low as 25 μm for human cortical and cancellous bones. Hasegawa *et al* (1994 and 1995) used the acoustic microscope to measure the longitudinal and shear acoustic velocity for bone structure such as the anisotropy ratio (the longitudinal elastic coefficients versus transverse elastic coefficients) and bone volume. Raum *et al* (2004) assessed the acoustic impedance of embedded cortical bone samples and demonstrated that higher frequencies such as 50 and 100 MHz used in SAM were more sensitive for the variation of bone structural and anisotropic elastic properties. The SAM techniques are implemented *in vitro* and its goal is mainly focused on the study of bone micro-structure and the relationship between bone elastic properties and bone macroscopical physical parameters such as SOS and BUA.

1.5.2 Estimation of the structural and acoustic properties of long bones

Besides focusing on small samples of flat and irregular bones, the mechanical strength and elasticity of long bones should be significantly considered to estimate bone qualities and predict fracture. Therefore the study of long bone cortex becomes a rapidly important topic on the osteoporosis and fracture research.

Different from the transverse transmission methods, ultrasonic measurements using an axial transmission technique have been developed to study the cortical shell of long bones such as femur and tibia (Muller *et al*, 2005). The technique has the source and receiver transducers located on the same side of the bone and the time signal is recorded at the same source location (zero-offset case) or several locations with the transducers moving away from the source at a pre-determined spatial interval (offset case). The propagation of ultrasound through long bones will be affected by the mechanical properties of the bone tissue such as elasticity, porosity, and internal micro-structure. The temporal (time) and dynamic (amplitude) characteristics of the recorded echoes will be dictated by the physical properties of the material under investigation. Also, the cortical/marrow interface has a very strong reflection coefficient, and the energy will be reflected to provide more information about the bone structure and properties.

Due to the longer propagating paths, different ultrasonic wave types are possibly generated in long bones. There are two main types of ultrasonic waves propagating in long bones: body waves (bulk waves) and guided waves. Body waves have well defined ray paths and arrival times, which can be determined by ray tracing (Lay and Wallace, 1995). Le *et al* (2010) has successfully used seismological techniques including waveform simulations and travelling time

calculations to investigate the nature of ultrasound wave propagation in long bones at small source-to-receiver distances and times. Their experiments confirm the existence of reflected and converted body waves originating from wave interaction at the internal interfaces of a bone structure by means of a simple, horizontally layered bone model. The first arriving signals (FAS) of three frequencies (200 KHz, 1.0 MHz, and 1.25 MHz) were used to measure the velocities of 41 fresh human radii. Their study shows that the high frequency measurements have better correlation with bone properties while the low frequency (200KHz) measurements are more sensitive to cortical thickness (Muller *et al*, 2005). Camus *et al* (2000) studied the lateral wave (head wave) and found that it had a potential to evaluate the mechanical properties of cortical bone using arrival time and velocity. Zheng *et al* (2007 and 2009) used multiple reflection echoes in the zero-offset case to estimate *n*BUA of cortical bone without recourse to the additional reference signals.

Guided waves are usually generated between bounded interfaces such as in the cortex of long bone. Guided waves are generated by the superposition of the reflections and multiples of the compressional waves, shear waves, and the converted waves within the cortical layers. Since the interfaces are strong reflectors (bounded above by soft tissue and below by marrow), the energy buildup by the summation of these waves is usually strong, allowing the guide wave modes to travel farther distances within the cortical layer. Guided wave analysis usually involves dispersion curves, which describe the change of phase velocity with frequency. Nicholson *et al* (2002) found that the velocity of lowest order Lamb asymmetrical (A_0) mode was significantly different between healthy and osteoporotic subjects in a pilot study; Bossy *et al* (2002 and 2004) and Moilanen *et al* (2007a and 2007b) used thin plates to mimic wave propagation in cortical bone for two-dimensional (2D) and three dimensional (3D) cases, and

used the Lamb wave mode to study the change of the apparent velocity with cortical thickness; Lefebvre *et al* (2002) reported that Lamb wave could be used to retrieve the Young's modulus with low frequency transducer; Moilanen *et al* (2004, 2006 and 2007) demonstrated that low frequency guided waves were sensitive to phantom thickness and suggested the use of guide waves to evaluate cortical thickness for the diagnosis of osteoporosis; Protopappas *et al* (2006) developed a two-dimensional (2D) bone model to mimic bone healing and observe the ultrasound guided wave propagation, especially the change of dispersive characteristics during the healing process.

1.5.3 Ultrasonic wavefield imaging

Wavefield imaging is widely used in geophysics to explore the Earth's interior and extract material properties such as velocity and reflectivity (Weglein, 1982; Miller *et al*, 1987; Beylkin and Burridge, 1990). Youzwishen (2001) and Youzwishen and Sacchi (2006), whose works have provided guidance to the development of this thesis, studied a 2D acoustic, constant density migration/inversion seismic problem using Born approximation and tested different regularization constraints including the edge-preserving constraints using simulated data. Similar principles can be applied to image and characterize bones.

Conventional medical ultrasound considers energy reflecting in the direction of incidence. Wavefield imaging makes use of waves travelling and scattering in all directions to image the bone interior, which leads to more accurate image reconstruction. Bone imaging research uses the transmission data or reflection data or the combination of both to reconstruct the cross-sectional image of long bone shafts (Lasaygues and Lefebvre, 2001).

Greenleaf (1981 and 1983) was the first to use ultrasound computer-assisted transmission tomography to image breast tissue. Using the arriving times and amplitudes of the transmission signals, they managed to estimate the two-dimensional distribution of acoustic velocity and attenuation in the scanned planes of the breast. Devaney (1983) applied diffraction tomography with Rytov approximation to develop the filtered back-propagation algorithm in computer simulation, and obtained a significant improvement in image quality comparing to the time and amplitude imaging method. Using the transmission signals, acquired by a 20-cm-diameter solid-state ultrasound ring array with 256 active and non-beamforming transducers, Pratt *et al* (2007) combined the time-of-flight method and 2D acoustic waveform inversion to image breast tissues and recover spatial distribution of sound speed and attenuation distribution. Duric *et al* (2005) developed a prototype ultrasound tomographic scanner to study breast imaging using phantoms and a cadaver breast. They used a pair of transducers to simulate up to 360 transmitter locations and 1600 receiver positions. Images of reflectivity and sound speed were successfully reconstructed from the scanned phantom data. They concluded that it was possible to image reflectivity with a 0.4 mm spatial resolution and 5 m/s variation in sound speed. The group went further to build a clinical prototype system and performed *in-vivo* studies (Duric *et al*, 2007). Their preliminary result demonstrated the feasibility to image human breast tissues using reflection and transmission ultrasound data. The reconstructed images had an in-plane 0.5 mm spatial resolution in reflection and 4 mm in transmission.

Imaging hard tissues such as bone is a challenging problem. Bone has high acoustic impedance as compared to neighboring soft tissue and marrow. When ultrasound travels from the source, through the bone samples, and to the receiver, the wave front is highly distorted as the wave crosses the tissue/bone or bone/marrow boundaries. A straight ray approach, as normally assumed for soft

tissue tomography, through the bone sample is not valid and Snell's law dictates the amount of refraction at the interfaces (Shearer, 1999).

The research group led by Lasaygues was perhaps the first and leading group to tackle the inverse wave scattering in bones with promising results. Using a 500 kHz nominal frequency and 180 projections, Lasaygues and Lefebvre (2001) reconstructed *in vitro* a human L2 lumber vertebra and a cortical human femur (60 projections applied) using reflected ultrasound tomography. Due to the strong contrast of bone with the soft tissues, low frequency ultrasound was used to improve the Born approximation, which in turn degraded the image resolution. They used a Papoulis super-resolution algorithm (Papoulis and Chamzas, 1979) to extend the spectrum of the signal beyond the frequency range available to enhance the image resolution. Multi-step compensation technique was also developed to enhance the reconstructed images, where the reflection tomography provided the information of the shape of the object and the transmission tomography was used to invert for the spatial variations of the inner structure (Ouedraogo *et al*, 2002; Lasaygues *et al*, 2004). Wavelet analysis was also applied to the transmitted signals to remove noise and enhance signal-to-noise ratio (Lasaygues *et al*, 2004; Lasaygues, 2007). Lasaygues *et al* (2005) used the ultrasonic tomography techniques to image the cross-section of human femur shafts and estimate the cortical thickness of long bone shaft in children using a 2D-ring antenna and mechanical and electronic steering systems (Lasaygues, 2006). The difference between the mechanical and acoustical measurements for thickness was mostly less than 0.5 mm (Lasaygues, 2006). Further Lasaygues and Le Marrec (2008) applied the intercepting canonical body approximation (ICBA) to solve imaging problem involving material with high impedance contrast with the surrounding medium. The ICBA method requires a previously determined model to seek the analytical solution of the forward problem, which is then applied to the iterative

inversion procedures. They found better inversion results than the classical reflection tomography method using simulation data for infinite elastic cylindrical tubes (Lasaygues and Le Marrec, 2008).

1.6 Objective of the thesis

The objective of this thesis is to develop a Born-based inversion technique to reconstruct the internal structure of long bones *in vitro*. The reflection data has been simulated or acquired on the bone surface by the axial transmission technique with zero offset. I use Born scattering and inverse theories to reconstruct 2D bone images and recover physical parameters of long bones such as SOS, interface locations, and cortical thickness. Using the simulated data, the feasibility and robustness of the inversion methodologies has been examined and the results have been used to improve the accuracy and quality of the reconstructed images. Finally, the inversion procedure has been applied to reconstruct real bone images and the recovered cortical thickness has been compared with measurements from X-ray CT images.

1.7 Summary of the thesis

In Chapter 2, I focus on wave propagation in long bones. Firstly, the elastic wave equation is derived; the acoustic wave equation is discussed under the zero-offset case where source and receiver are at the same location and there is no mode conversion. Secondly, I derive the Born approximation to the acoustic wave equation for the constant and variable background velocity. The equation thus derived forms the forward modeling equation for the scattered wavefields. To enhance the computation speed, the concept of beam aperture is introduced to

restrict the mathematical operations to a limited set of pixels within a fan window. Lastly, I describe some fundamentals of ray tracing algorithm in the varying velocity fields, which is used to compute travelled distance and travelling times.

Inversion is described in Chapter 3. Starting from the ill-posed problems, the chapter reviews the regularized least squares methods to solve linear system of equations. To improve the efficiency of the computer resource, this leads to the discussion of using conjugate gradient iterative algorithm to seek least squares solutions. The forward and adjoint operators for the scattered wavefields are derived. The adjoint operator is the inversion operator for the reconstructed image given the observed data. Lastly the imaging resolution and quality are considered for the ideal and real cases.

In Chapter 4, I test the accuracy and robustness of the algorithm using the synthetic data set. The data sets are simulated by the simple convolution method and finite-difference (FD) method. I also investigate how the variations of some inversion parameters and configurations might affect the reconstructed images. To this end, the optimal parameters thus derived are used to invert the FD data set.

In Chapter 5, the inversion algorithm is applied to real bone data. Estimate of SOS through cortex of long bone using offset axial transmission technique is discussed. The SOS measurements thus derived are used for the inversion. Three bone data sets are inverted for the thickness of the top cortical layer. The measured thickness is compared with the measurements from the CT images. The chapter is concluded by presenting a full inversion for all interfaces of a bone data set.

Chapter 6 concludes the thesis with further comments for future directions.

Chapter 2

Wave propagation in long bones

The propagation of ultrasound in a medium is governed by the wave equation, which is a system of second order hyperbolic partial differential equations. The equations are derived from the Newton's second law and Hooke's law, which relates the stress and strain. In this chapter, I derive the general solution to the wave equation. Since the problem at hand is a zero offset case where the transmitter and the receiver are at the same location, and normal incidence is assumed, there is no mode conversion. Only the acoustic wave equation is of our interest in this thesis. Therefore, I discuss further the solution of the acoustic wave equation, the Born approximation to the acoustic wave equation, and ray tracing.

2.1 General wave equation and the solutions

The wave equation governs the propagation of wave disturbance and its solution describes the motion of mechanical waves in a medium. Consider an infinitesimal isotropic, homogenous, and elastic solid cube at a point P(x,y,z), the displacement vector **u**(u,v,w) at the point P is governed by the following system of equations (Fung, 1977)

$$\rho \frac{\partial^2 u}{\partial t^2} = (\lambda + \mu) \frac{\partial \theta}{\partial x} + \mu \nabla^2 u \quad , \tag{2.1a}$$

$$\rho \frac{\partial^2 v}{\partial t^2} = (\lambda + \mu) \frac{\partial \theta}{\partial y} + \mu \nabla^2 v \quad , \tag{2.1b}$$

$$\rho \frac{\partial^2 w}{\partial t^2} = (\lambda + \mu) \frac{\partial \theta}{\partial z} + \mu \nabla^2 w \quad , \tag{2.1c}$$

where λ and μ are the *lam é* constant and rigidity respectively, t is time, and ρ is density. The divergence θ and Laplacian ∇^2 operators are

$$\nabla = \frac{\partial}{\partial x}\mathbf{i} + \frac{\partial}{\partial y}\mathbf{j} + \frac{\partial}{\partial z}\mathbf{k} \quad , \tag{2.2a}$$

$$\theta = \nabla \cdot \mathbf{u} = \frac{\partial u}{\partial x} + \frac{\partial v}{\partial y} + \frac{\partial w}{\partial z} \quad , \tag{2.2b}$$

and

$$\nabla^2 = \nabla \cdot \nabla = \frac{\partial^2}{\partial x^2} + \frac{\partial^2}{\partial y^2} + \frac{\partial^2}{\partial z^2} \tag{2.2c}$$

where **i**, **j**, **k** are the unit vectors along the *x*, *y* and *z* directions. The motion can be regarded as a combination of two kinds of motion (Ewing *et al*, 1957):

1) the equivoluminal motion (divergence free), i.e., $\nabla \cdot \mathbf{u} = 0$ and
2) the irrotational motion (curl free), i.e., $\nabla \times \mathbf{u} = 0$.

With the introduction of a scalar potential φ and a vector potential $\mathbf{\Psi}(\psi_1, \psi_2, \psi_3)$, the displacement vector can be described by

$$\mathbf{u} = \nabla \varphi + \nabla \times \mathbf{\Psi} \tag{2.3}$$

and

$$u = \frac{\partial \varphi}{\partial x} + \frac{\partial \psi_3}{\partial y} - \frac{\partial \psi_2}{\partial z} \quad , \tag{2.4a}$$

$$v = \frac{\partial \varphi}{\partial y} + \frac{\partial \psi_1}{\partial z} - \frac{\partial \psi_3}{\partial x} \quad , \tag{2.4b}$$

$$w = \frac{\partial \varphi}{\partial z} + \frac{\partial \psi_2}{\partial x} - \frac{\partial \psi_1}{\partial y} \quad . \tag{2.4c}$$

By substituting (2.4) into (2.2b), we obtain

$$\begin{aligned}
\theta &= \frac{\partial u}{\partial x} + \frac{\partial v}{\partial y} + \frac{\partial w}{\partial z} \\
&= \frac{\partial}{\partial x}\left(\frac{\partial \varphi}{\partial x} + \frac{\partial \psi_3}{\partial y} - \frac{\partial \psi_2}{\partial z}\right) + \frac{\partial}{\partial y}\left(\frac{\partial \varphi}{\partial y} + \frac{\partial \psi_1}{\partial z} - \frac{\partial \psi_3}{\partial x}\right) + \frac{\partial}{\partial z}\left(\frac{\partial \varphi}{\partial z} + \frac{\partial \psi_2}{\partial x} - \frac{\partial \psi_1}{\partial y}\right) \\
&= \frac{\partial^2 \varphi}{\partial x^2} + \frac{\partial^2 \varphi}{\partial y^2} + \frac{\partial^2 \varphi}{\partial z^2} + \frac{\partial^2 \psi_3}{\partial x \partial y} - \frac{\partial^2 \psi_2}{\partial x \partial z} + \frac{\partial^2 \psi_1}{\partial y \partial z} - \frac{\partial^2 \psi_3}{\partial x \partial y} + \frac{\partial^2 \psi_2}{\partial x \partial z} - \frac{\partial^2 \psi_1}{\partial y \partial z} \\
&= \frac{\partial^2 \varphi}{\partial x^2} + \frac{\partial^2 \varphi}{\partial y^2} + \frac{\partial^2 \varphi}{\partial z^2} \\
&= \nabla^2 \varphi \quad .
\end{aligned} \tag{2.5}$$

Replacing θ by $\nabla^2 \varphi$ in (2.1a) yields

$$\begin{aligned}
\rho \frac{\partial^2 u}{\partial t^2} &= (\lambda + \mu) \frac{\partial \theta}{\partial x} + \mu \nabla^2 u \quad , \\
\rho \frac{\partial^2}{\partial t^2}\left(\frac{\partial \varphi}{\partial x} + \frac{\partial \psi_3}{\partial y} - \frac{\partial \psi_2}{\partial z}\right) &= (\lambda + \mu) \frac{\partial}{\partial x}(\nabla^2 \varphi) \\
&\quad + \mu \nabla^2 \left(\frac{\partial \varphi}{\partial x} + \frac{\partial \psi_3}{\partial y} - \frac{\partial \psi_2}{\partial z}\right) \quad , \\
\rho \frac{\partial}{\partial x}\left(\frac{\partial^2 \varphi}{\partial t^2}\right) + \rho \frac{\partial}{\partial y}\left(\frac{\partial^2 \psi_3}{\partial t^2}\right) - \rho \frac{\partial}{\partial z}\left(\frac{\partial^2 \psi_2}{\partial t^2}\right) &= (\lambda + \mu) \frac{\partial}{\partial x}(\nabla^2 \varphi) + \mu \frac{\partial}{\partial x}(\nabla^2 \varphi) \\
&\quad + \mu \frac{\partial}{\partial y}(\nabla^2 \psi_3) - \mu \frac{\partial}{\partial z}(\nabla^2 \psi_2) \quad , \\
\frac{\partial}{\partial x}\left(\rho \frac{\partial^2 \varphi}{\partial t^2}\right) + \frac{\partial}{\partial y}\left(\rho \frac{\partial^2 \psi_3}{\partial t^2}\right) - \frac{\partial}{\partial z}\left(\rho \frac{\partial^2 \psi_2}{\partial t^2}\right) &= \frac{\partial}{\partial x}[(\lambda + 2\mu)\nabla^2 \varphi] \\
&\quad + \frac{\partial}{\partial y}(\mu \nabla^2 \psi_3) - \frac{\partial}{\partial z}(\mu \nabla^2 \psi_2) \; .
\end{aligned} \tag{2.6}$$

Similarly for (2.1b) and (2.1c),

$$\frac{\partial}{\partial x}(\rho\frac{\partial^2\varphi}{\partial t^2})+\frac{\partial}{\partial y}(\rho\frac{\partial^2\psi_1}{\partial t^2})-\frac{\partial}{\partial z}(\rho\frac{\partial^2\psi_3}{\partial t^2})=\frac{\partial}{\partial x}[(\lambda+2\mu)\nabla^2\varphi] + \frac{\partial}{\partial y}(\mu\nabla^2\psi_1)-\frac{\partial}{\partial z}(\mu\nabla^2\psi_3) \qquad (2.7)$$

and

$$\frac{\partial}{\partial x}(\rho\frac{\partial^2\varphi}{\partial t^2})+\frac{\partial}{\partial y}(\rho\frac{\partial^2\psi_2}{\partial t^2})-\frac{\partial}{\partial z}(\rho\frac{\partial^2\psi_1}{\partial t^2})=\frac{\partial}{\partial x}[(\lambda+2\mu)\nabla^2\varphi] + \frac{\partial}{\partial y}(\mu\nabla^2\psi_2)-\frac{\partial}{\partial z}(\mu\nabla^2\psi_1) \quad . \qquad (2.8)$$

For (2.6), (2.7), and (2.8) to be valid, the following relationship must be satisfied:

$$\nabla^2\varphi=\frac{1}{\alpha^2}\frac{\partial^2\varphi}{\partial t^2} \qquad (2.9a)$$

and

$$\nabla^2\psi_i=\frac{1}{\beta^2}\frac{\partial^2\psi_i}{\partial t^2} \qquad (i=1,\ 2,\ 3) \qquad (2.9b)$$

where

$$\alpha=\sqrt{\frac{\lambda+2\mu}{\rho}} \qquad \text{and} \qquad \beta=\sqrt{\frac{\mu}{\rho}}\ . \qquad (2.10)$$

Eq. (2.9a) describes a curl-free motion travelling with a speed α. The wave is known as a compressional, longitudinal, primary or *P*-wave. The particle motion of compressional wave is parallel to or along the direction of wave energy propagation. The second motion given by (2.9b) is a divergence-free motion and travels with a velocity β. The particle motion defined by the second part of (2.3),

i.e., $\nabla \times \boldsymbol{\Psi}$, is perpendicular to the direction of energy propagation. This motion is known as shear, rotational, transverse, distortional or *S*-wave (Ewing *et al*, 1957).

2.2 Acoustic wave equation

When an ultrasound beam is incident obliquely upon an interface between two solids, waves will be reflected and refracted, and partition of energy will take place at the interface. Mode conversion is also possible, i.e., the conversion from longitudinal wave to shear wave or vice versa. These waves are known as elastic waves and the wave equation governing their propagation in solids is known as the elastic wave equation (Brekhovskikh, 1980). Shear waves cannot propagate in fluid where μ=0. The wave that travels in fluid is compressional in nature and known as acoustic wave. Similarly, the acoustic wave equation governs the propagation of an acoustic wave field.

Solving an acoustic wave equation is much easier than the elastic wave equation because the latter has the compressional and shear wave components coupled with each other. Figure 2.1 illustrates a photograph of a sectioned bovine tibia. In the mid portion of the long shaft, there are three layers: cortical bone, marrow, and cortical bone. The layers are not perfectly stratified but as a first approximation, the structure can be modeled by three layers (Le *et al*, 2010). Figure 2.2 shows an experimental setup for data acquisition. More details about the experimental setup will be provided later in Chapter 5. The transducer is both a transmitter and a receiver. We consider acoustic wave fields in my study based on the following reasons. Firstly, we only consider the zero-offset case, i.e., the transmitter and the receiver are at the same location on the bone surface. Secondly, we consider the mid shaft of the long bone where the layers tend to be more flat and parallel. In this case, the normal incidence condition can be assumed, i.e., the

ultrasound beam goes straight down into the bone and reflects straight back from the interface, thus mode conversions can be neglected in the wave propagation. Lastly, the experimental data are genuine with signals of the same polarity across the records, which indicate those motions vibrating in the same direction of ultrasound wave propagation. The timings of these echoes are consistent with the compressional wave velocities. If a shear wave exists, its contribution is insignificant. Based on these reasons, the use of acoustic wave equation is reasonably justified.

Figure 2.1 A photograph of a sectioned long shaft of a bovine tibia, which was cut in half along the axial direction.

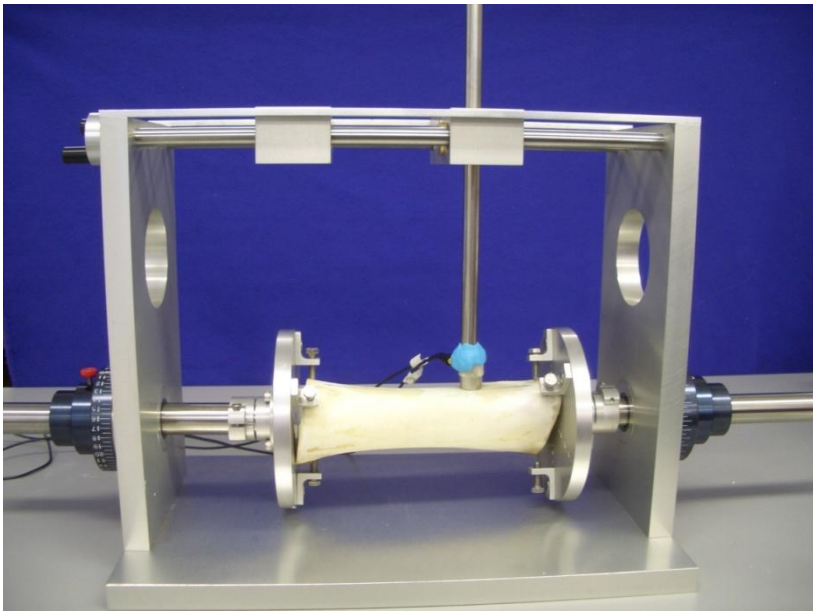

Figure 2.2 A photograph of the experimental setup and transducer used to acquire zero-offset data.

Consider an acoustic wavefield $u(\mathbf{x},\mathbf{s},t)$ in a heterogeneous medium satisfying the inhomogeneous acoustic wave equation with an impulsive point source $\delta(\mathbf{s},t)$

$$\nabla^2 u(\mathbf{s},\mathbf{x},t) - \frac{1}{c^2(\mathbf{x})}\frac{\partial^2 u(\mathbf{s},\mathbf{x},t)}{\partial t^2} = -\delta(\mathbf{x}-\mathbf{s},t) \tag{2.11}$$

where $\mathbf{x}$ is an arbitrary point in the wavefield, $\mathbf{s}$ is the position of the impulsive source, and $c(\mathbf{x})$ is the space-dependent wave speed. By taking the Fourier transform, we rewrite Eq. (2.11) as an inhomogeneous Helmholtz equation:

$$\nabla^2 U(\mathbf{s},\mathbf{x},\omega) + \frac{\omega^2}{c^2(\mathbf{x})}U(\mathbf{s},\mathbf{x},\omega) = -\delta(\mathbf{x}-\mathbf{s}) \tag{2.12}$$

where

$$U(\omega) = \int_{-\infty}^{\infty} u(t) e^{-i\omega t} dt \tag{2.13}$$

is used and ω is the radial frequency.

2.3 Born approximation

The Born approximation (BA) was first introduced by Taylor (Taylor, 1952) to solve scattering problems of electromagnetic waves. Since then, BA has been intensively applied to scattering problems in the fields of quantum mechanics and earth physics. In geophysics, the theory has been used to image the earth's interior using seismic data. The topics in this area are usually known as *seismic migration* (Yilmaz, 1987). The application of BA to bone imaging was pioneered by Lasaygues (Lasaygues and Lefebvre, 2001; Lasaygues *et al*, 2005; Lasaygues, 2006) and is still in its infancy. Since BA forms the foundation of the bone imaging described in this thesis, it deserves a detailed description of the mathematical derivation. The presentation below follows closely the works by Miller *et al* (1987).

2.3.1 Born approximation of acoustical wave equation

We first assume that the velocity field is a combination of background velocity $c_0(\mathbf{x})$ and perturbation velocity profile $p(\mathbf{x})$,

$$\frac{1}{c^2(\mathbf{x})} = \frac{1}{c_0^{\,2}(\mathbf{x})} + p(\mathbf{x}) \tag{2.14}$$

where $p(\mathbf{x})$ is also called the acoustic scattering potential of the medium,

describing the scattering strength of the perturbation between the actual medium and background medium at each point. Replacing $c(\mathbf{x})$ in (2.12) by the background and perturbation velocity fields, we arrive at

$$\nabla^2 U(\mathbf{s},\mathbf{x},\omega) + \omega^2 \left(\frac{1}{c_0{}^2(\mathbf{x})} + p(\mathbf{x}) \right) U(\mathbf{s},\mathbf{x},\omega) = -\delta(\mathbf{x}-\mathbf{s}) \tag{2.15a}$$

or

$$\nabla^2 U(\mathbf{s},\mathbf{x},\omega) + \frac{\omega^2}{c_0{}^2(\mathbf{x})} U(\mathbf{s},\mathbf{x},\omega) = -\delta(\mathbf{x}-\mathbf{s}) - \omega^2 p(\mathbf{x}) \nabla^2 U(\mathbf{s},\mathbf{x},\omega) \ . \tag{2.15b}$$

We define the Green's function $G_0(\mathbf{x},\mathbf{y},\omega)$ to satisfy the nonhomogeneous Helmholtz Eq. (2.12) for the background velocity $c_0(\mathbf{x})$

$$\nabla^2 G_0(\mathbf{x},\mathbf{y},\omega) + \frac{\omega^2}{c_0{}^2(\mathbf{x})} G_0(\mathbf{x},\mathbf{y},\omega) = -\delta(\mathbf{x}-\mathbf{y}) \tag{2.16}$$

where $\mathbf{x}$ and $\mathbf{y}$ are two arbitrary points in the wavefield space. With the introduction of the Green's function G_0, the solution of the wavefield U can be rewritten as an integral equation (Morse and Feshbach, 1953)

$$U(\mathbf{s},\mathbf{y},\omega) = G_0(\mathbf{s},\mathbf{y},\omega) + \omega^2 \int d^3x G_0(\mathbf{x},\mathbf{y},\omega)\, p(\mathbf{x}) U(\mathbf{s},\mathbf{x},\omega) \ . \tag{2.17}$$

The wavefield is governed by two parts: the first part arises from the background medium and the second part is due to the scattering perturbation $p(\mathbf{x})$. Eq. (2.17) is known, in a variant form, as Lippmann-Schwinger equation (Lippmann and Schwinger, 1950). According to the Lippmann-Schwinger equation, if the integral equation has two spatially separate interacting parts resulting from the stable background and the small disturbance, then we can decompose the solution into two corresponding components. These two components are 1) the unperturbed

component corresponding to stimulation from the stable background, i.e., the final state of the system without the perturbation, and 2) the scattering component caused by the small disturbances. We can express these two components in a single equation using the integral Eq. (2.17). If we take the Laplacian of (2.17), we will be able to recover Eq. (2.15b).

Let $D(\mathbf{s},\mathbf{y},\omega)$ be the scattered wavefield travelling from the source, **s** to the scatterer, **x** and back to the observation point, **y** due to the scattering potential $p(\mathbf{x})$

$$\begin{aligned} D(\mathbf{s},\mathbf{y},\omega) &= U(\mathbf{s},\mathbf{y},\omega) - G_0(\mathbf{s},\mathbf{y},\omega) \\ &= \omega^2 \int d^3x G_0(\mathbf{x},\mathbf{y},\omega)\, p(\mathbf{x}) U(\mathbf{s},\mathbf{x},\omega) \quad . \end{aligned} \tag{2.18}$$

To be more specific, the observed wavefield at the receiver position **y** = **r** is related to the potential $p(\mathbf{x})$, i.e., the second term of (2.17)

$$D(\mathbf{s},\mathbf{r},\omega) = \omega^2 \int d^3x G_0(\mathbf{x},\mathbf{r},\omega)\, p(\mathbf{x}) U(\mathbf{s},\mathbf{x},\omega) \quad . \tag{2.19}$$

Eq. (2.19) is a nonlinear equation because $U(\mathbf{s},\mathbf{x},\omega)$ is dependent on the scattered potential $p(\mathbf{x})$. If the scattering perturbation is small, we can approximate the total field $U(\mathbf{s},\mathbf{x},\omega)$ by the background field $G_0(\mathbf{x},\mathbf{y},\omega)$. By doing so, Eq. (2.19) can be linearized as

$$D(\mathbf{s},\mathbf{r},\omega) = \omega^2 \int d^3x G_0(\mathbf{x},\mathbf{r},\omega)\, p(\mathbf{x}) G_0(\mathbf{s},\mathbf{x},\omega) \quad . \tag{2.20}$$

Eq. (2.20) is a single-scattering approximation of the acoustic Helmholtz equation and only holds when the scattering potential field is small. When the background velocity is constant, i.e., $c(\mathbf{x}) = c_0$, the equation is known as Born approximation (BA). When the velocity is spatially varying, the equation is a distorted-wave Born approximation (DWBA) (Taylor, 1952). Eq. (2.20) denotes the impulse response for the scattered wavefield $D(\mathbf{s},\mathbf{y},\omega)$. With a source function

$s(t)$, Eq. (2.20) becomes

$$D(\mathbf{s},\mathbf{r},\omega) = \omega^2 S(\omega)\int d^3x G_0(\mathbf{x},\mathbf{r},\omega)\, p(\mathbf{x}) G_0(\mathbf{s},\mathbf{x},\omega) \tag{2.21}$$

where $S(\omega)$ is the Fourier representation of the source function.

Generally the asymptotic approximation will be used to evaluate the Green's function, G_0. For simple structures, G_0 has a simple analytic expression of a plane wave

$$G_0(\mathbf{x},\mathbf{y},\omega) = A(\mathbf{x},\mathbf{y}) e^{-j\omega\tau(\mathbf{x},\mathbf{y})} \tag{2.22}$$

where $A(\mathbf{x},\mathbf{y})$ is the amplitude and $\tau(\mathbf{x},\mathbf{y})$ is the time it takes the ultrasound to travel from $\mathbf{x}$ to $\mathbf{y}$. Beylkin (1985) provides an explicit form of the Green's function based on the asymptotic expansion of the Hankel function

$$G_0(\mathbf{x},\mathbf{y}) \approx e^{-i(\pi/2)(n+1)/2} \frac{k^{(n-3)/2}}{2\left(2\pi|\mathbf{x}-\mathbf{y}|\right)^{(n-1)/2}} e^{-ik|\mathbf{x}-\mathbf{y}|} \tag{2.23}$$

where n is the number of dimension, k is the wave number and $k = \omega/c$. The travelling time τ in a constant velocity background, $c_0(\mathbf{x})$ is

$$\tau(\mathbf{x},\mathbf{y}) = \frac{|\mathbf{x}-\mathbf{y}|}{c_0} \tag{2.24}$$

and the amplitude, $A(\mathbf{x},\mathbf{y})$ is explicitly given by

$$A(\mathbf{x},\mathbf{y}) = \frac{1}{4\pi|\mathbf{x}-\mathbf{y}|} \tag{2.25a}$$

for the 3D ($n = 3$) case or

$$A(\mathbf{x},\mathbf{y}) = \frac{k^{-1/2}}{2\left(2\pi|\mathbf{x}-\mathbf{y}|\right)^{1/2}} \tag{2.25b}$$

for the 2D (n = 2) case where $k = \omega/c_0$. Further,

$$G_0(\mathbf{x},\mathbf{r},\omega)G_0(\mathbf{s},\mathbf{x},\omega) = A(\mathbf{s},\mathbf{x},\mathbf{r})e^{-j\omega\tau(\mathbf{s},\mathbf{x},\mathbf{r})} \tag{2.26}$$

where

$$A(\mathbf{s},\mathbf{x},\mathbf{r}) = A(\mathbf{s},\mathbf{x})A(\mathbf{x},\mathbf{r}) \tag{2.27a}$$

and

$$\tau(\mathbf{s},\mathbf{x},\mathbf{r}) = \tau(\mathbf{s},\mathbf{x}) + \tau(\mathbf{x},\mathbf{r}) = \frac{|\mathbf{x}-\mathbf{r}| + |\mathbf{s}-\mathbf{x}|}{c_0} \ . \tag{2.27b}$$

Using Eq. (2.26), Eq. (2.21) can be rewritten as

$$D(\mathbf{s},\mathbf{r},\omega) = \omega^2 S(\omega)\int d^3x A(\mathbf{s},\mathbf{x},\mathbf{r})e^{-j\omega\tau(\mathbf{s},\mathbf{x},\mathbf{r})}p(\mathbf{x}) \ . \tag{2.28}$$

Eq. (2.28) can be discretized for computational purpose. For a 2D problem, the discretized form of the scattered wavefield is

$$D(\mathbf{s},\mathbf{r},\omega_i) = \omega_i^2 S(\omega_i)\Delta x\Delta z\sum_k A(\mathbf{s},\mathbf{x}_k,\mathbf{r})e^{-j\omega_i\tau(\mathbf{s},\mathbf{x}_k,\mathbf{r})}p(\mathbf{x}_k) \tag{2.29}$$

where Δx and Δz are the cell or pixel dimensions of the model matrix.

Eq. (2.29) is an important result and forms the forward operator of the inversion procedure. It reveals the relationship between the recorded scattered wavefield, $D(\mathbf{s},\mathbf{r},\omega)$ and the scattered potential, $p(\mathbf{x})$. The recorded wavefield is also related to many inversion parameters, which we explore further in Chapter 4.

According to Eq. (2.29), the scattered wavefield, $D(\mathbf{s},\mathbf{r},\omega)$ is computed by

summing the contribution of the scattering potential at all pixel locations, $\mathbf{x}_k$ below the source-receiver plane. To reduce computational cost, we suggest limiting the computation to a region, which we call an aperture. The pixels which fall within the aperture will be contributed to the scattered wavefield computation. Such an aperture definition has physical meaning, which is related to the transducer's radiation pattern. For a piezoelectric transducer, the transmitting pattern, or known as radiation pattern, has a symmetric lobe with the maximum transmitting strength at the normal direction, which is the vertical direction perpendicular to the transducer's active surface. The transmitting strength decreases as the beam direction is deviated away from the normal. Usually, an aperture of $\pm 60^\circ$ covers a transmitting region, beyond which the transmitting energy is very insignificant. The dominant transmitting strength lies within $\pm 40^\circ$. An example of the radiation pattern of a dual-head P-wave composite transducer is given in Chapter 5 (Figure 5.1C). By reciprocity property, the receiving sensitivity pattern of the transducer is similar. Since the region outside the aperture will not be insonified by the beam and therefore the assumption that the pixels within the aperture contributed mainly to the recorded scattered response is justified.

2.3.2 A pictorial illustration of the scattering formalism

Wave propagation in bone is a complicated phenomenon. Figure 2.3 illustrates a snapshot image at 4 μs of ultrasound wave propagation in a femur with a single point source on the top surface of the bone shaft. The result was simulated using commercial software Wave2000 (CyberLogic, Inc., New York). The figure shows a point source generates the cylindrical wavefronts propagating downward into the bone structure. When the wavefronts encounter a reflector, which can be an interface or small inhomogeneity, the secondary sources are

created by Huygen's principle to generate wavefronts to different directions.

The pictorial description of scattering theory is shown in Figure 2.4. Consider an ultrasound beam incident on a scatterer at (x,z). The energy will be scattered by the scatterer to all directions (Figure 2.4A). The receivers positioned at the surface will pick up the scattered energy and the recorded echoes plotted in a distance-time (x,t) space will demonstrate a diffraction pattern (Figure 2.4B). This is known as the *forward* problem, i.e. from the model space (x,z) to the data (x,t) space. For the *inverse* problem, which will be discussed in Chapter 3, the task is to image the model space (x,z) by inverting the observation (x,t) data. The imaging procedure goes backward as shown in (Figure 2.4B) and can be accomplished by summing the diffracted energy along the diffraction pattern for the position of the scatterer. The location of the scatterer is considered to be the focal point of energy.

The clinical medical ultrasound scanners only consider energy reflecting or scattering in the direction of incidence to form an ultrasound image. In contrast to the conventional techniques, the wave imaging approach presented in this thesis will make use of the coherent wave fields arriving within an aperture, leading to a more accurate reconstruction of the bone image.

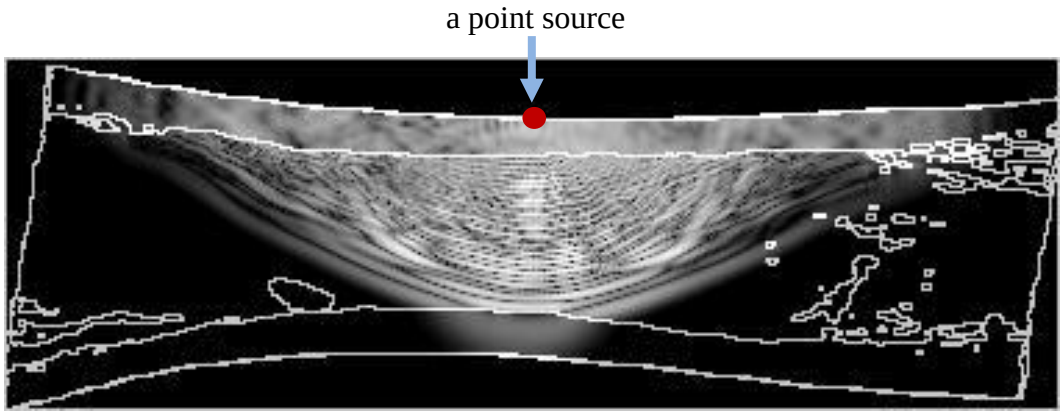

Figure 2.3 A snapshot at 4 μs of ultrasound wave propagating in a bovine femur. The simulated waves are generated by a point source on the bone surface.

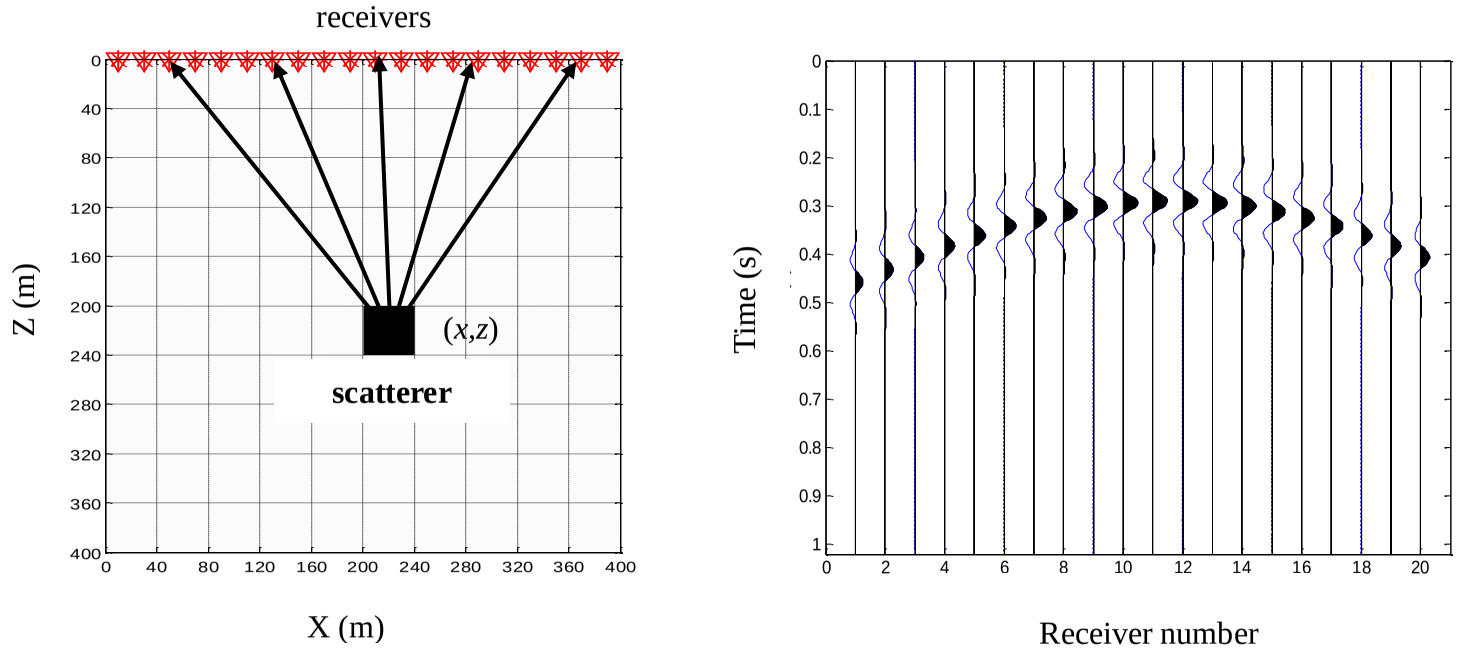

Figure 2.4 The schematic diagram for the scattering formalism: (A) a single scatterer deflecting energy in oblique directions and (B) the time signals recorded by the receivers.

2.4 Ray tracing

In order to compute the Green's functions (Eq. [2.26]) for each grid cell **x**, we need to know the travelled distance, l and time, τ of ultrasound between the source and the cell and the cell back to the receiver. In our case, source and receiver are at the same location. For a constant uniform velocity, the travelled distance and time are easily calculated. For a three layered structure where the layers are not necessarily planar, the ray must bend across the interface according to Snell's law and calculating the two parameters for the structure poses some challenge. Usually ray tracing is the most commonly used method. This section will review the fundamentals of ray tracing.

Following Lay and Wallace (1995) closely, we consider a ray in a (x,z) plane travelling an arc length l and normal to the wavefront $Q(\mathbf{x})$ in a medium where the velocity changes gradually (Figure 2.5). The eikonal equation of the wavefront is governed by

$$\left(\frac{1}{n}\frac{\partial Q(\mathbf{x})}{\partial x}\right)^2+\left(\frac{1}{n}\frac{\partial Q(\mathbf{x})}{\partial z}\right)^2=1 \tag{2.30}$$

where $n=c_0/c(\mathbf{x})$ is the index of refraction. In Eq. (2.30), $\nabla Q(\mathbf{x})$ is normal to the wavefront and parallel to the ray. The directions of the ray are given by the direction cosines (see Figure 2.5),

$$\frac{dx}{dl}=\sin\theta \quad \text{and} \quad \frac{dz}{dl}=\cos\theta \tag{2.31}$$

where θ is the take-off angle. The direction cosines are related by

$$\left(\frac{dx}{dl}\right)^2+\left(\frac{dz}{dl}\right)^2=1 \ . \tag{2.32}$$

Comparing (2.30) and (2.32), we have the system of normal equations

$$n\frac{dx}{dl}=\frac{\partial Q(x,z)}{\partial x} \qquad \text{and} \qquad n\frac{dz}{dl}=\frac{\partial Q(x,z)}{\partial z} \ . \tag{2.33}$$

Taking the derivative of (2.33) with respect to *dl*,

$$\begin{aligned}
\frac{d}{dl}\left(n\frac{dx}{dl}\right) &= \frac{d}{dl}\left(\frac{\partial Q(x,z)}{\partial x}\right) \\
&= \frac{\partial}{\partial x}\left(\frac{dQ(x,z)}{dl}\right) \\
&= \frac{\partial}{\partial x}\left(\frac{\partial Q(x,z)}{\partial x}\frac{dx}{dl}+\frac{\partial Q(x,z)}{\partial z}\frac{dz}{dl}\right) \\
&= \frac{\partial}{\partial x}\left(n\frac{dx}{dl}\frac{dx}{dl}+n\frac{dz}{dl}\frac{dz}{dl}\right) \\
&= \frac{\partial}{\partial x}\left(n\left(\left(\frac{dx}{dl}\right)^2+\left(\frac{dz}{dl}\right)^2\right)\right) \\
&= \frac{\partial}{\partial x}n \ .
\end{aligned} \tag{2.34a}$$

Similarly,

$$\frac{d}{dl}\left(n\frac{dz}{dl}\right)=\frac{\partial}{\partial z}n \ . \tag{2.34b}$$

With (2.31), Eq. (2.34) becomes

$$\frac{d}{dl}\left(n\sin\theta\right)=\frac{\partial}{\partial x}n \tag{2.35a}$$

and

$$\frac{d}{dl}\left(n\cos\theta\right)=\frac{\partial}{\partial z}n\ . \tag{2.35b}$$

If we assume that the velocity changes along the *x* direction, then (2.35a) becomes

$$\begin{aligned}
\frac{d}{dl}\left(n\sin\theta\right)&=\frac{dn}{dx}\\
\sin\theta\frac{dn}{dl}+n\cos\theta\frac{d\theta}{dl}&=\frac{dn}{dx}\\
\sin\theta\frac{dn}{dx}\frac{dx}{dl}+n\cos\theta\frac{d\theta}{dl}&=\frac{dn}{dx}\\
\sin\theta\frac{dn}{dx}\sin\theta+n\cos\theta\frac{d\theta}{dl}&=\frac{dn}{dx}\\
n\cos\theta\frac{d\theta}{dl}&=\frac{dn}{dx}\left(1-\sin^2\theta\right)\\
n\cos\theta\frac{d\theta}{dl}&=\frac{dn}{dx}\cos^2\theta\\
\frac{d\theta}{dt}\frac{dt}{dl}&=\frac{1}{n}\frac{dn}{dx}\cos\theta\\
\frac{d\theta}{dt}&=\frac{1}{n}\frac{dl}{dt}\frac{dn}{dx}\cos\theta\ .
\end{aligned} \tag{2.36}$$

Since

$$\frac{dl}{dt}=c(x,z) \tag{2.37}$$

and the index of refraction by definition,

$$\frac{dn}{n}=-\frac{dc}{c}\ , \tag{2.38}$$

Eq. (2.36) becomes

$$\frac{d\theta}{dt} = c\left(-\frac{dc}{c}\right)\frac{1}{dx}\cos\theta$$

$$= -\frac{dc}{dx}\cos\theta = -c_x\cos\theta \qquad (2.39a)$$

where c_x is the velocity gradient along the x direction. Next, we assume that the velocity changes in z direction and taking the similar step as above, we have

$$\frac{d\theta}{dt} = \frac{dc}{dz}\sin\theta = c_z\sin\theta \qquad (2.39b)$$

where c_z is the velocity gradient along the z direction. Superimposing the increment of take-off angle $d\theta$ in x and z directions yields

$$d\theta = \left(c_z\sin\theta - c_x\cos\theta\right)dt \quad . \qquad (2.40)$$

In summary, for each ray travelling through the medium with a take-off angle θ, the total travelled distance l and the corresponding travelling time t can be calculated by the following algorithm.

Algorithm 2.1: Initially given that a constant sampling interval dt and velocity gradients, c_x and c_z, we set $l = t = 0$, $\theta = \theta_0$, $x = x_0$, and $z = z_0$, then the iteration continues until the difference between the predicted receiver position $\mathbf{r}^{pred}$ and the true position, $\mathbf{r}$ is within a pre-defined tolerance.

(a) $dl = c(x,z)dt$,

(b) $dx = \sin\theta dl$,

(c) $dz = \cos\theta dl$,

(d) $d\theta = \left(c_z \sin\theta - c_x \cos\theta\right) dt$,

(e) $l = l + dl$,

(f) $x = x + dx$,

(g) $z = z + dz$,

(h) $\theta = \theta + d\theta$,

(i) $t = t + dt$.

The ray tracing algorithm is used to calculate the travelled distances and travelling times for a smoothly varying velocity field. During the inversion process, the background velocity does not change and only perturbation velocity does. Therefore to avoid the repetition to compute the travelled distances and travelling times, the strategy is to compute the results once and store them in tables. For each source/receiver pair, there are three tables storing the calculated travelled distance l, the travelling time τ, and the take-off angle θ associated with each grid cell $\mathbf{x}$, and each table is the same size as the background velocity model. The stored information will be retrieved when it is needed.

The ray tracing algorithm is based on the assumption that the change in velocity gradient of the medium between two points, $\mathbf{x}_1$ and $\mathbf{x}_2$ is small with respect to the velocity at $\mathbf{x}_1$ (see Figure 2.5). Therefore the velocity profile is necessarily smooth without sharp discontinuities. In this study, the background velocity profile is smoothed by convolving a 5×5 Boxcar filter with the velocity profile prior to ray tracing. However the smoothed velocity field will create inaccuracy relevant to the reconstructed position of the interfaces. The misplacement will become more serious as the interfaces are deeper. This will be

further discussed in Chapter 4.

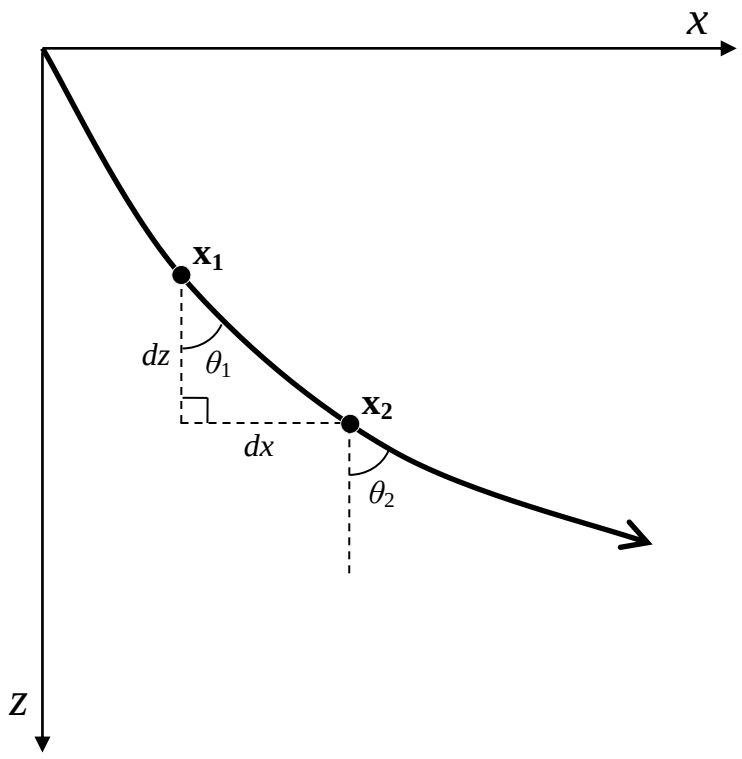

Figure 2.5 A two dimensional ray path in a medium where the velocity changes continuously in both *x* and *z* directions. Also shown is the relationship between $\mathbf{x}_1$ and $\mathbf{x}_2$ where $\mathbf{x}_2 = \mathbf{x}_1 + d\mathbf{x}$ and $\theta_2 = \theta_1 + d\theta$.

2.5 Summary and comment

In this chapter, I have provided a derivation of the Born approximation to the acoustic wave equation. I advocate the use of the acoustic wave equation instead of the elastic wave equation based on the source/receiver configuration and the geometry of the cortical layers. As shown in Figure 2.1, the cortical layers are quite parallel in the mid diaphysis of the long bones. The surface of the bone samples in contact with the transducer is smooth and reasonably flat, enabling the ultrasound beam to penetrate into the bone approximately normal to bone surface. In case of zero-offset where the positions of the source and receivers are the same, the waves are normally incident and mode conversion does not occur.

Figure 2.6A is a sagittal computed tomographic (X-ray CT) image of a bovine tibia. The long bone is consisted of mainly cortical bone and marrow with the cancellous bone at the distal and proximal epiphysis. The cortical layer and marrow are fairly homogenous. In a study of 175 females, Wang *et al* (1997) found that the mean velocity of cortical shell in tibia was 3850.7 ± 119.3 m/s. The velocity of marrow is usually considered to be 1500 m/s, similar to the velocity of soft tissues (Camus *et al*, 2000; Muller *et al*, 2005). On the other hand, the cancellous bone in the diaphysis is not as much as in the proximal and distal epiphysis, but its existence makes the interface between cortex and marrow not as sharp as expected. It is reasonable to model the long bone using a background medium with a small perturbation. As such, BA is quite suitable for the long bone imaging.

Figure 2.6B shows a constructed velocity model for the bovine tibia which will be described in Chapter 4. Cancellous bone is modeled by trabeculae with marrow filling the pores. The trabeculae are the thin plate compact bone with similar properties as cortical bone. To improve the accuracy of imaging in the

case of curved interfaces, ray tracing will be applied to the variable background velocity field.

According to Eq. (2.25), we assume that the amplitude is inversely proportional to the travelling distance based on the 2D Green's function. However, compact bone is a highly damping material. The average nBUA (normalized Broadband Ultrasound Attenuation) value was 4.91 ± 0.65 dB/MHz/cm for bovine cortical bone (Zheng *et al*, 2007). The signal amplitude will be attenuated further due to the intrinsic absorption.

The equations relevant to scattering theory presented so far are derived in the frequency domain. This allows the implementation of absorption if the material through which ultrasound travels is anelastic. However, absorption is not considered in the thesis, therefore the content described below is only used for future implementation.

When an ultrasound pulse travelling through an isotropic and absorptive medium, the spectral amplitude can be described as a superposition of plane waves

$$A(f, \mathbf{x}) = W(f) \exp\left[i \left(\mathbf{k} \cdot \mathbf{x} - 2\pi f t \right) \right] \tag{2.41}$$

where f is the frequency and $\mathbf{k}$ is the wavenumber vector. Because the medium is absorptive, the wavenumber is complex (Waters *et al*, 2000)

$$\mathbf{k} = \mathbf{k}_r + i\boldsymbol{\alpha} \tag{2.42}$$

where $\mathbf{k}_r$ is the real part of the wavenumber, $\boldsymbol{\alpha}$ is the attenuation coefficient in neper/unit length, and $i^2 = -1$. Substituting (2.42) into (2.41) yields

$$A(f,\mathbf{x}) = W(f)\exp(-\boldsymbol{\alpha}\cdot\mathbf{x})\exp\left[i\left(\mathbf{k}_r\cdot\mathbf{x}-2\pi ft\right)\right] \tag{2.43}$$

where each frequency component travels with the phase velocity $V = 2\pi f/|\mathbf{k}_r|$, and its amplitude decays exponentially with $|\boldsymbol{\alpha}|$ due to absorption.

(A)

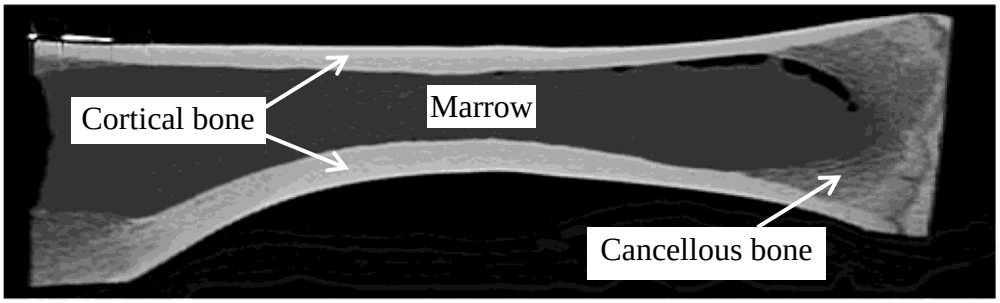

(B)

Figure 2.6 A bovine tibia: (A) an X-ray computed tomographic (CT) image and (B) a constructed velocity model based on (A).

Chapter 3

Inverse theory

In general terms, inverse problems deal with the estimation of model parameters from the observed data. Inverse theories have been widely applied in many branches of science and engineering such as geophysics, medical imaging, remote sensing, astronomy, acoustic tomography and nondestructive testing. In geophysics, inverse theory is used to recover the spatial distribution of material properties within the earth using the data acquired on the Earth's surface or within the boreholes (Parker, 1994). In medical imaging, X-ray tomographic imaging uses the Radon transform and its inverse to back project the X-ray planar images or slices around the body to reconstruct the inner image of the human body (Kak and Slaney, 1988). In this chapter, I first provide an overview of inverse theory (Hansen, 1998； Menke， 1989). I then apply the inverse theory to solve the linear system arising from the acoustic wave propagation through bone as described in Chapter 2.

3.1 Inversion of ill-posed problems

A linear system can be denoted in the discrete matrix form as

$$\mathbf{Gm} = \mathbf{d} \tag{3.1}$$

where **d** is the observed data vector with dimension $N_d \times 1$, **m** is the $N_m \times 1$ vector of model parameters, and **G** is the $N_d \times N_m$ matrix of physical parameters describing the explicit relationship between the model parameters and the

observed data. The forward problem is to compute the predicted data $\mathbf{d}^{pred}$ given the model **m**. The objective of an inverse problem is to seek a best model **m** given the observed data **d**. (Menke, 1989).

For an inverse problem, if the number of observations is more than the number of unknowns, i.e., $N_d > N_m$, the problem is said to be over-determined. The least squares method is usually applied to find the best fit between the observation and the desired model. If $N_d < N_m$, the problem is under-determined and there is not enough data to determine the unknowns. In this case, an additional regularization term is used to determine a solution for the model. However, some real problems are either over- or under-determined, and known as mixed-determined problem (Menke, 1989). An example of a mixed-determined type problem comes from our study; some image cells are sufficiently sampled by several ultrasonic rays while some are totally missed.

When noise exists, Eq. (3.1) will be modified as

$$\mathbf{Gm} + \mathbf{n} = \mathbf{d} \tag{3.2}$$

where **n** is the random noise vector. Comparing (3.1) and (3.2), the solution for physical model **m** is influenced by the presence of noise. A well-posed problem has mainly three conditions for a solution: *existence*, *uniqueness*, and *stability* (Hansen, 1998). Most inverse problems are ill-posed because the solution is non-unique or the solution is not stable and sensitive to small changes in the data (Claerbout, 1992; Hansen, 1998). An example of an ill-posed problem is ultrasound wave propagating through the bone structure. In addition to the electronic noise, scattering from the inhomogeneities of the bone inner structures influences the primary reflections and contributes to the coda of the signals, degrading the signal resolution.

3.2 Least squares solutions

To seek a solution to the inverse problem (3.2), the inversion procedure is to minimize the misfit error, $\mathbf{e} = \mathbf{d} - \mathbf{d}^{pred}$, between the observed data and the predicted data for an optimum model **m**. In general, one would like to seek a solution by minimizing in a least squares sense the cost or objective function, $J = \mathbf{e}\mathbf{e}^T$ where the subscript T denotes the transpose of a vector. Quite often, the data has random noise and other coherent noise. The noise in the data causes error and instability to the solution. To overcome the problem, some *prior* information or relationship between the model parameters is used as a constraint to regularize the solution. Therefore, the general form of the cost function is made up of two terms: (1) the misfit or prediction error term $\|\mathbf{Gm}-\mathbf{d}\|_2^2$ and (2) the regularization term, **Qm**,

$$J = \|\mathbf{Gm}-\mathbf{d}\|_2^2 + \mu\|\mathbf{Qm}\|_2^2 \ . \tag{3.3}$$

In (3.3), the first term represents the L_2 norm misfit between the predicted and observed data. The second term is the regularization term where **Q** is the constraint or regularization matrix or operator and μ is the regularization parameter, also known as Lagrange multiplier, trade-off, weighting or damping parameter. The regularization term provides some degree of smoothness to obtain solution stability.

Generally, the misfit and regularization terms in cost function cannot be both fulfilled with minimization and then the optimal solution is found to satisfy a compromise between these two terms. For the extreme situation, if $\mu = 0$, the regularization term will be totally neglected and the solution will completely fit the observed data, which may be greatly oscillating, unstable, and far away from

smoothness. If μ is set to a very large number, a smooth model solution is found, which may not have any meaning, and the predicted data may not fit the observed data at all. So in the real cases, the optimum regularization parameter should be chosen according to the specific ill-posed problems. The trade-off curve is a very common method to determine the value of regularization parameter (Hansen, 1998). The curve is usually plotted as the misfit versus the norm of regularization term by taking a series of values of μ for a large range, say for example from 10^{-4} to 10^{3}. An example of a trade-off curve is provided in Chapter 5 (Figure 5.5).

Expanding (3.3),

$$\begin{aligned} J &= \|\mathbf{Gm}-\mathbf{d}\|_2^2 + \mu\|\mathbf{Qm}\|_2^2 \\ &= (\mathbf{Gm}-\mathbf{d})^T(\mathbf{Gm}-\mathbf{d}) + \mu(\mathbf{Qm})^T(\mathbf{Qm}) \\ &= \mathbf{m}^T\mathbf{G}^T\mathbf{Gm} - \mathbf{d}^T\mathbf{Gm} - \mathbf{m}^T\mathbf{G}^T\mathbf{d} + \mathbf{d}^T\mathbf{d} + \mu\mathbf{m}^T\mathbf{Q}^T\mathbf{Qm} \quad . \end{aligned} \tag{3.4}$$

Taking the first derivative of (3.4) with respect of **m** and setting it to zero,

$$\begin{aligned} \frac{dJ}{d\mathbf{m}} &= 2\mathbf{G}^T\mathbf{Gm} - \mathbf{G}^T\mathbf{d} - \mathbf{G}^T\mathbf{d} + \mu\mathbf{Q}^T\mathbf{Qm} \\ &= 2(\mathbf{G}^T\mathbf{G} + \mu\mathbf{Q}^T\mathbf{Q})\mathbf{m} - 2\mathbf{G}^T\mathbf{d} \\ &= 0 \end{aligned}$$

or

$$(\mathbf{G}^T\mathbf{G} + \mu\mathbf{Q}^T\mathbf{Q})\mathbf{m} = \mathbf{G}^T\mathbf{d} \quad . \tag{3.5}$$

Seeking the least squares solution to Eq. (3.2) reduces to find the solution of the linear system (3.5). If the matrix ($\mathbf{G}^T\mathbf{G}+\mu\mathbf{Q}^T\mathbf{Q}$) is invertible, the estimated least squares solution, $\mathbf{m}^{est}$ is

$$\mathbf{m}^{est} = (\mathbf{G}^T\mathbf{G} + \mu\mathbf{Q}^T\mathbf{Q})^{-1}\mathbf{G}^T\mathbf{d} \quad . \tag{3.6}$$

Depending on the configuration of regularization matrix **Q**, the solution takes different form. The matrix **Q** can be linear or non-linear. For example, the Edge Preserving Regularization (EPR) constraints are often used to preserve edges of the image (Lobel *et al*, 1997; Youzwishen and Sacchi, 2006), **Q** in this case will be nonlinear. In this thesis, I am focusing on the linear inverse problem.

3.2.1 Unconstrained Least squares (ULS) solution

In this case, **Q** = 0. Eq. (3.6) becomes

$$\mathbf{m}^{\mathbf{est}} = (\mathbf{G}^T\mathbf{G})^{-1}\mathbf{G}^T\mathbf{d}. \tag{3.7}$$

The unconstrained least squares (ULS) solution truly minimizes the misfit or the prediction error. The procedure assumes that the noise in the data does not create any instability of the solution and thus no regularization in model space is required. In most real cases, the ULS solution is not practical and hardly used in actual problems as the noise in the data affects the stability of the solution, causing a meaningless or non-convergent solution in most cases.

3.2.2 Damped least squares (DLS) solution

For DLS case, the regularization matrix is an identity matrix, i.e., **Q** = **I**. The regularization term is simply composed of the L_2 norm of the model vector, $\|\mathbf{m}\|_2^2$. Thus

$$\mathbf{m}^{\mathbf{est}} = (\mathbf{G}^T\mathbf{G} + \mu\mathbf{I})^{-1}\mathbf{G}^T\mathbf{d}. \tag{3.8}$$

The method used the norm of the model vector as a constraint; therefore the procedure does not only minimize the prediction error and therefore, does not provide a model with the least prediction error. If the regularization parameter is

chosen appropriately, the solution reaches a compromise between minimizing the prediction error and the length of the model. The DLS method provides a smoother and practical solution which considers both accuracy and stability of the reconstructed model (Claerbout, 1992).

3.2.3 Weighted least squares (WLS) solution

When regularization other than the identity operator is considered, the method assumes some degrees of dependency among the model elements to achieve smoothness of the solution. In this case, **Q** = **W** where **W** is the weighting operator and

$$\mathbf{m}^{\mathbf{est}} = (\mathbf{G}^T\mathbf{G} + \mu\mathbf{W}^T\mathbf{W})^{-1}\mathbf{G}^T\mathbf{d}. \tag{3.9}$$

The weighting matrix or operator **W** can take any form. A very common type of the weighting matrix is a derivative matrix (Claerbout, 1992), which can either be the first order derivative as

$$\mathbf{D}_1 = \begin{pmatrix} 1 & -1 & & & \\ & 1 & -1 & & \\ & & \ddots & \ddots & \\ & & & 1 & -1 \\ & & & & 1 \end{pmatrix} \tag{3.10}$$

or the second order derivative as

$$\mathbf{D}_2 = \begin{pmatrix} 1 & -2 & 1 & & \\ & 1 & -2 & 1 & \\ & & \ddots & \ddots & \\ & & & 1 & -2 \\ & & & & 1 \end{pmatrix}. \tag{3.11}$$

The derivative operatives are often used to enhance sharp edges or discontinuities.

Figure 3.1 shows an example of the least squares solution. A model (Figure 3.1A) convolves with a 10 Hz Ricker wavelet (Figure 3.1B) with 20% random noise added to yield the time series shown in Figure 3.1C. The solutions were calculated using the conjugate gradient (CG) method, which will be described in the next section. The number of iterations used is 1000 for all solutions. Figure 3.1D shows the ULS solution, which is oscillatory and very unstable. Figure 3.1E shows a much smoother and stable DLS result with $\mu = 0.1$, but the amplitudes are much smaller than the original model because of the smoothness resulting from the regularization term. The WLS solution is shown in Figure 3.1F. The method uses the first derivative operator, $\mathbf{D}_1$ with $\mu = 0.1$ and recovers all the edges with comparable amplitude and without compromising the smoothness of the model.

3.3 Iterative methods

When the matrix **G** is very large, the computation of the solution via Eqs. (3.7) - (3.9) is not effective and sometimes impossible due to the instability when seeking the inverse matrix of a large scale system and limitation in memory storage. Even though **G** is sparse, matrices resulting from matrix factorization are more dense than **G** itself (Aster *et al*, 2005). In most cases, iterative methods are sought to solve the systems of equations. The most commonly used method is the conjugate gradient method developed by Hestenes and Stiefel in 1951 (Hestenes and Stiefel, 1952). This method was initially applied to solve a large sparse linear system with less computation cost and fast convergence speed (Hansen, 1998).

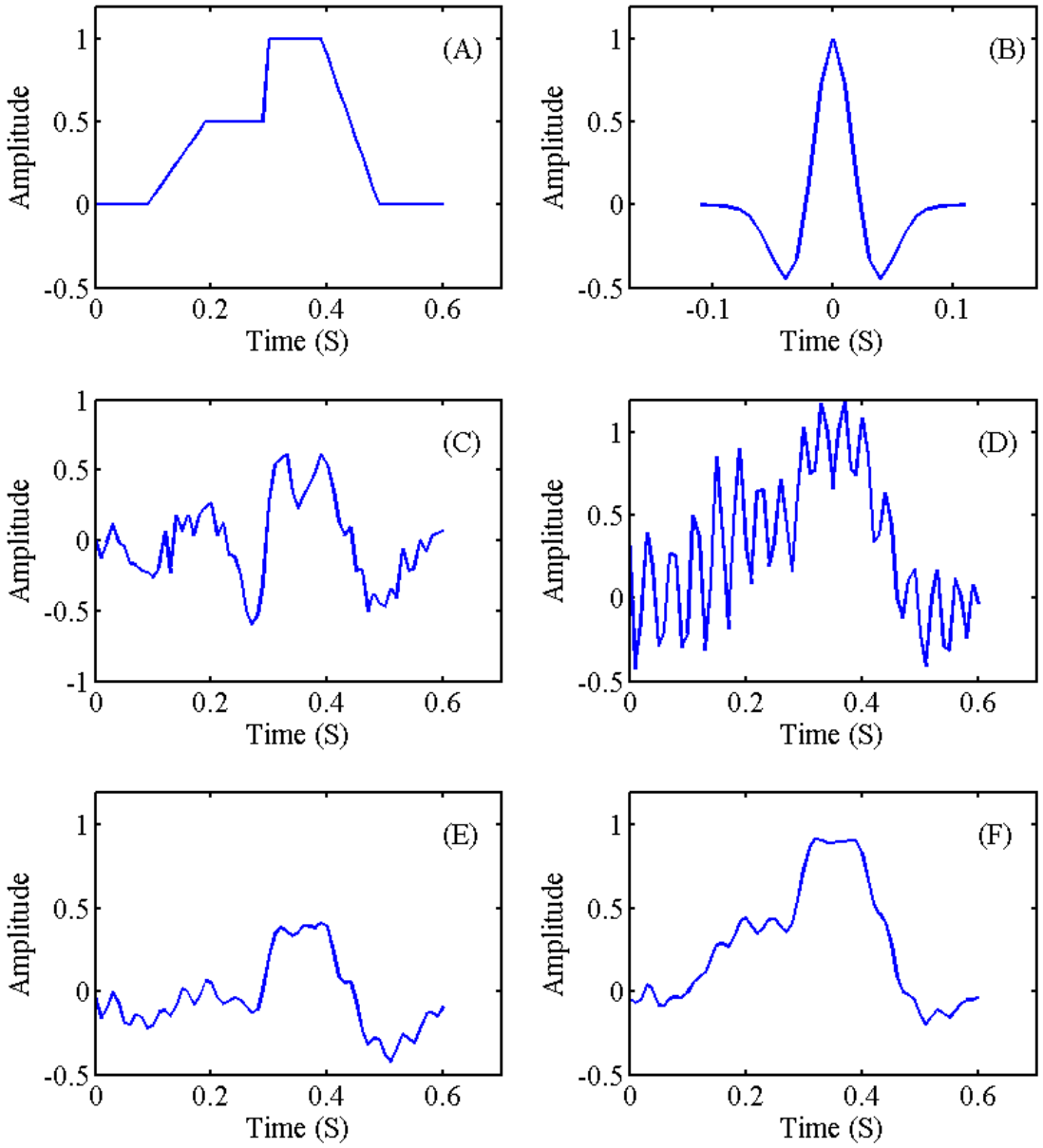

Figure 3.1 The least squares solutions: (A) a model, (B) a 10 Hz Ricker wavelet, (C) a convolved time series with 20% random noise, (D) the ULS solution, (E) the DLS solution with $\mu = 0.1$, and (F) the WLS method with $\mu = 0.1$ and $\mathbf{W} = \mathbf{D}_1$.

3.3.1 Method of conjugate gradient (CG)

Consider a system of linear equations,

$$\mathbf{Lx} = \mathbf{y} \tag{3.12}$$

where **L** is a symmetric and positive-definite matrix, i.e., $\mathbf{z}^T\mathbf{Lz} > 0$ for any nonzero vector **z**. The CG method seeks a solution to **Lx** = **y**, which minimizes the cost function by computing a series of converging model vectors, $\mathbf{x}_0$, $\mathbf{x}_1$, …, $\mathbf{x}_k$ (Aster *et al*, 2005). In the process, the procedure constructs a series of basis vectors, **p** of **x**, and the corresponding coefficients, α_i, i.e.,

$$\mathbf{x} = \sum_{i=0}^{k} \alpha_i \mathbf{p}_i \tag{3.13}$$

where the basis vectors are mutually conjugate with respect to **L,**

$$\left(\mathbf{p}_i, \mathbf{L}\mathbf{p}_j\right) = 0 \quad \text{when } i \neq j \ . \tag{3.14}$$

Also constructed is a series of orthogonal residual (or prediction error) vectors, **r** i.e.,

$$\left(\mathbf{r}_i, \mathbf{r}_j\right) = 0 \quad \text{when } i \neq j \ . \tag{3.15}$$

where $\mathbf{r} = \mathbf{y} - \mathbf{Lx}$**.** The CG algorithm is as follows (Hestenes and Stiefel, 1952; Aster *et al*, 2005).

Algorithm 3.1: Let $\mathbf{x} = \mathbf{x}_0$, $\mathbf{p}_0 = \mathbf{r}_0 = \mathbf{y} - \mathbf{Lx}_0$, and $k = 0$. The following steps will be repeated until number of iterations or the tolerance limit for convergence is reached.

(a) $\alpha_k = \dfrac{\mathbf{r}_k{}^T \mathbf{r}_k}{\mathbf{p}_k{}^T \mathbf{L} \mathbf{p}_k}$.

(b) $\mathbf{x}_{k+1} = \mathbf{x}_k + \alpha_k \mathbf{p}_k$.

(c) $\mathbf{r}_{k+1} = \mathbf{y} - \mathbf{L}\mathbf{x}_{k+1}$.

(d) $\beta_k = \dfrac{\mathbf{r}_{k+1}{}^T \mathbf{r}_{k+1}}{\mathbf{r}_k{}^T \mathbf{r}_k}$.

(e) $\mathbf{p}_{k+1} = \mathbf{r}_{k+1} + \beta_k \mathbf{p}_k$.

(f) $k = k + 1$.

3.3.2 Application of CG method to least squares solutions

The algorithm 3.1 can be applied to different least squares solutions in Section 3.2. Depending on the kind of LS solutions, the operator, **L** takes different form.

3.3.2.1 Unconstrained least squares solution

Recall that the system of linear equations given by (3.5) with **Q** = 0 is

$$\mathbf{G}^T\mathbf{G}\mathbf{m} = \mathbf{G}^T\mathbf{d}. \qquad \text{(from Eq. [3.7])}$$

Comparing (3.7) and (3.12), we have **L = G**^{T}**G**, **y = G**^{T}**d**, where **L** is symmetric and positive definite. The algorithm 3.1 can be modified as follows.

Algorithm 3.2: Let $\mathbf{m}_0 = 0$, $\mathbf{p}_0 = \mathbf{r}_0 = \mathbf{G}^T\mathbf{d} - \mathbf{G}^T\mathbf{G}\mathbf{m}_0 = \mathbf{G}^T\mathbf{d}$, and $k = 0$. The following steps will be repeated until number of iterations or the tolerance limit for convergence is reached.

(a) $\alpha_k = \dfrac{\mathbf{r}_k{}^T\mathbf{r}_k}{\mathbf{p}_k{}^T\mathbf{G}^T\mathbf{G}\mathbf{p}_k} = \dfrac{\mathbf{r}_k{}^T\mathbf{r}_k}{(\mathbf{G}\mathbf{p}_k)^T(\mathbf{G}\mathbf{p}_k)}$.

(b) $\mathbf{m}_{k+1} = \mathbf{m}_k + \alpha_k\mathbf{p}_k$.

(c) $\mathbf{r}_{k+1} = \mathbf{G}^T\mathbf{d} - \mathbf{G}^T\mathbf{G}\mathbf{m}_{k+1} = \mathbf{G}^T(\mathbf{d} - \mathbf{G}\mathbf{m}_{k+1})$.

(d) $\beta_k = \dfrac{\mathbf{r}_{k+1}{}^T\mathbf{r}_{k+1}}{\mathbf{r}_k{}^T\mathbf{r}_k}$.

(e) $\mathbf{p}_{k+1} = \mathbf{r}_{k+1} + \beta_k\mathbf{p}_k$.

(f) $k = k + 1$.

The **G**-matrix multiplication takes place once in (a) and twice in (c) for a total of three times in each iteration. The multiplication can be reduced to twice for each iteration by introducing two intermediate vectors:

$$\mathbf{q}_k = \mathbf{G}\mathbf{p}_k \tag{3.16a}$$

and

$$\begin{aligned}\mathbf{s}_{k+1} &= \mathbf{d} - \mathbf{G}\mathbf{m}_{k+1} \\ &= \mathbf{d} - \mathbf{G}(\mathbf{m}_k + \alpha_{k+1}\mathbf{p}_k) \\ &= \mathbf{d} - \mathbf{G}\mathbf{m}_k - \alpha_{k+1}\mathbf{G}\mathbf{p}_k \\ &= \mathbf{s}_k - \alpha_{k+1}\mathbf{q}_k \quad .\end{aligned} \tag{3.16b}$$

Thus algorithm 3.2 can be revised as follows.

Algorithm 3.3: Let $\mathbf{m}_0 = 0$, $\mathbf{p}_0 = \mathbf{r}_0 = \mathbf{G}^T\mathbf{d}$, $\mathbf{s}_0 = \mathbf{d}$, $\mathbf{q}_0 = \mathbf{G}\mathbf{p}_0$, and $k = 0$. The following steps will be repeated until number of iterations or the tolerance limit for convergence is reached.

(a) $\alpha_k = \dfrac{\mathbf{r}_k{}^T \mathbf{r}_k}{\mathbf{q}_k{}^T \mathbf{q}_k}$.

(b) $\mathbf{m}_{k+1} = \mathbf{m}_k + \alpha_k \mathbf{p}_k$.

(c) $\mathbf{s}_{k+1} = \mathbf{s}_k - \alpha_k \mathbf{q}_k$.

(d) $\mathbf{r}_{k+1} = \mathbf{G}^T \mathbf{s}_{k+1}$.

(e) $\beta_k = \dfrac{\mathbf{r}_{k+1}{}^T \mathbf{r}_{k+1}}{\mathbf{r}_k{}^T \mathbf{r}_k}$.

(f) $\mathbf{p}_{k+1} = \mathbf{r}_{k+1} + \beta_k \mathbf{p}_k$.

(g) $\mathbf{q}_{k+1} = \mathbf{G}\mathbf{p}_{k+1}$.

(h) $k = k + 1$.

The method discussed in this section is also known the conjugate gradient least squares (CGLS) algorithm (Hansen, 1998).

3.3.2.2 Damped least squares solution

The system of linear equations given by (3.5) with **Q** = **I** is

$$(\mathbf{G}^T\mathbf{G} + \mu\mathbf{I})\mathbf{m} = \mathbf{G}^T\mathbf{d} \qquad \text{(from Eq. [3.8])}$$

where we identify $\mathbf{L} = \mathbf{G}^T\mathbf{G} + \mu\mathbf{I}$. The algorithm is the same as algorithm 3.3 with the steps (a) and (d) replaced by the following:

(a) $\alpha_k = \dfrac{\mathbf{r}_k{}^T \mathbf{r}_k}{\mathbf{p}_k{}^T (\mathbf{G}^T\mathbf{G}+\mu\mathbf{I})\mathbf{p}_k} = \dfrac{\mathbf{r}_k{}^T \mathbf{r}_k}{\mathbf{q}_k{}^T \mathbf{q}_k + \mu \mathbf{p}_k{}^T \mathbf{p}_k}$.

(d) $\mathbf{r}_{k+1} = \mathbf{G}^T\mathbf{d} - (\mathbf{G}^T\mathbf{G}+\mu\mathbf{I})\mathbf{m}_{k+1} = \mathbf{G}^T\mathbf{s}_{k+1} - \mu\mathbf{m}_{k+1}$.

3.3.2.3 Weighted least squares solution

The system of linear equations given by (3.5) with **Q** = **W** is

$$(\mathbf{G}^T\mathbf{G} + \mu\mathbf{W}^T\mathbf{W})\mathbf{m} = \mathbf{G}^T\mathbf{d} \qquad \text{(from Eq. [3.9])}$$

where we identify $\mathbf{L} = \mathbf{G}^T\mathbf{G} + \mu\mathbf{W}^T\mathbf{W}$. Similarly, the algorithm is the same as algorithm 3.3 with the steps (a) and (d) replaced by the following:

$$\text{(a)} \quad \alpha_k = \frac{\mathbf{r}_k{}^T\mathbf{r}_k}{\mathbf{p}_k{}^T(\mathbf{G}^T\mathbf{G}+\mu\mathbf{W}^T\mathbf{W})\mathbf{p}_k} = \frac{\mathbf{r}_k{}^T\mathbf{r}_k}{\mathbf{q}_k{}^T\mathbf{q}_k + \mu(\mathbf{W}\mathbf{p}_k)^T(\mathbf{W}\mathbf{p}_k)} \quad .$$

$$\text{(d)} \quad \mathbf{r}_{k+1} = \mathbf{G}^T\mathbf{d} - (\mathbf{G}^T\mathbf{G}+\mu\mathbf{W}^T\mathbf{W})\mathbf{m}_{k+1} = \mathbf{G}^T\mathbf{s}_{k+1} - \mu\mathbf{W}^T\mathbf{W}\mathbf{m}_{k+1} \, .$$

In WLS method, the weighting matrix **W** will increase the computational effort in comparison with ULS and DLS methods. Particularly in calculating the residual **r**, the **W**-operation will be performed twice at each step, which can greatly increase the computation cost especially in case of large scale systems.

3.4 Forward and adjoint operators

A mathematical operator is considered a mapping from a vector space to another. Forward operator maps the model space to the data space. Instead of using an inverse to seek a solution of the model space, we consider here adjoint operator to back-project the wavefield to obtain the image. An adjoint operator, which is a matrix transpose, is not an inverse. According to Claerbout (1992), an adjoint operator is better than an inverse because the former can accommodate incompleteness and imperfection of the data. Claerbout also provides some forward and adjoint operators commonly used in the imaging and inversion problems:

Matrix multiply	<< >>	Conjugate transpose matrix multiply
Convolution	<< >>	Cross-correlation

Zero padding	<< >>	Truncation
Diffraction modeling	<< >>	Imaging by migration

A given operator **L** is adjoint to $\mathbf{L}^T$ if $(\mathbf{x}, \mathbf{Ly}) = (\mathbf{y}, \mathbf{L}^T\mathbf{x})$ for any two vectors, **x** and **y**. This is known as the dot-product test (Claerbout, 1992). In this thesis, the operators are all numerically defined and not implicitly formulated matrix, therefore the dot-product test is applied to verify the forward/adjoint pair.

3.4.1 Operators of the scattered wavefields

Recall the 2D discretized form of the scattered wavefield for a single frequency ω_i at source position **s** and receiver position **r** is

$$D(\mathbf{s},\mathbf{r},\omega_i) = \omega_i^2 S(\omega_i)\Delta x\Delta z \sum_k A(\mathbf{s},\mathbf{x}_k,\mathbf{r}) e^{-j\omega_i \tau(\mathbf{s},\mathbf{x}_k,\mathbf{r})} p(\mathbf{x}_k) \quad , \quad \text{(from Eq. [2.29])}$$

which can be casted in a matrix form for each frequency ω_i:

$$\mathbf{D}(\omega_i) = \mathbf{L}(\mathbf{s},\mathbf{r},\mathbf{x},\omega_i) \times \mathbf{P} \,, \tag{3.17}$$

where **L** is the forward operator related to the source/receiver positions (**s**,**r**), and the scatterer position (**x**) and **P** is the perturbation matrix.

In Eq. (3.17), the operator **L** can be regarded as a large scale matrix with dimension $N_d \times N_m$, where N_d is equal to the number of the signal records, and N_m is equal to the number of model pixels. Then the forward procedure is the matrix multiplication of the forward operating matrix **L** and the model vector **P**. Based on the complex matrix multiplication property, the adjoint operator $\mathbf{L}^T$ will be its conjugate transpose. To find the adjoint of $\mathbf{G}_0$ in (2.22), $\mathbf{G}_0$ is replaced by its complex conjugate $\mathbf{G}_0^*$ as

$$\mathbf{G}_0^*(\mathbf{x},\mathbf{y},\omega) = A(\mathbf{x},\mathbf{y})e^{j\omega\tau(\mathbf{x},\mathbf{y})}.$$

To implement the transpose transformation, the index of source/receiver pairs replaces the index of model cells. Then the adjoint operator can be approximated by

$$\tilde{p}(\mathbf{x},\omega_i) = \omega_i^2 S(\omega_i)\Delta x\Delta z\left(\sum_j A(\mathbf{s}_j,\mathbf{x},\mathbf{r}_j)e^{j\omega_i\tau(\mathbf{s}_j,\mathbf{x},\mathbf{r}_j)}d(\mathbf{s}_j,\mathbf{r}_j,\omega_i)\right) \tag{3.18}$$

or in matrix form

$$\tilde{\mathbf{P}}(\omega_i) = \mathbf{L}^T(\mathbf{s},\mathbf{r},\mathbf{x},\omega_i)\times\mathbf{D}(\omega_i). \tag{3.19}$$

The operators, $\mathbf{L}$ and $\mathbf{L}^T$ are adjoint operators based on the dot-product test. Both Eq. (3.17) and (3.19) play an important role for the inversion process.

3.4.2 The derivative operator

In a two-dimensional system, the differentiation of a set of discrete data can be presented by the data matrix convolving with the derivative operator matrix shown as below

$$\mathbf{D}_f = \begin{pmatrix} c & a & c \\ a & b & a \\ c & a & c \end{pmatrix} \tag{3.20}$$

where *a*, *b*, *c* are the predetermined constants. The value of constants can be set as zero or nonzero, but the sum of all the elements in operator matrix must be zero. For example, for the first derivative operator, it can be

$$\mathbf{D}_f = \begin{pmatrix} 0 & -1/4 & 0 \\ -1/4 & 1 & -1/4 \\ 0 & -1/4 & 0 \end{pmatrix}$$

or

$$\mathbf{D}_f = \begin{pmatrix} -1/8 & -1/8 & -1/8 \\ -1/8 & 1 & -1/8 \\ -1/8 & -1/8 & -1/8 \end{pmatrix}$$

for five- or nine-point differentiation.

To illustrate the differentiation process, matrix **M** on the right of the Figure 3.2 shows the value of m_{ij}, the center of a 9-cell grid, is a weighted sum of the 8 neighboring cells and itself with the derivative operator (3.20):

$$m'_{ij} = \begin{pmatrix} c & a & c & a & b & a & c & a & c \end{pmatrix} \begin{pmatrix} m_{i-1,j-1} \\ m_{i-1,j} \\ m_{i-1,j+1} \\ m_{i,j-1} \\ m_{i,j} \\ m_{i,j+1} \\ m_{i+1,j-1} \\ m_{i+1,j} \\ m_{i+1,j+1} \end{pmatrix}. \tag{3.21}$$

Since the adjoint of matrix multiplication is its conjugate transpose, the adjoint operator of the derivative can be calculated as

$$\begin{pmatrix} m_{i-1,j-1} \\ m_{i-1,j} \\ m_{i-1,j+1} \\ m_{i,j-1} \\ m_{i,j} \\ m_{i,j+1} \\ m_{i+1,j-1} \\ m_{i+1,j} \\ m_{i+1,j+1} \end{pmatrix} = \begin{pmatrix} c \\ a \\ c \\ a \\ b \\ a \\ c \\ a \\ c \end{pmatrix} m_{ij}' \,. \tag{3.22}$$

What Eq. (3.22) does is to reverse the process of (3.21) by appropriately allocating (or weighting) the value of m_{ij}' to the 9 neighboring cells m_{ij} (including itself) of the grid (see Figure 3.2). Any mapping from **M′**-space to **M**-space will involve the same cell in **M**-space nine times and, therefore, the allocated values to the same cell will be accumulated accordingly. This leads to the following algorithm.

Algorithm 3.4: Let the values of the 9 cells, m_{ij}, be zero.

```
for i = 2:n_i-1
        for j = 2:n_j-1
                m(i,j)      =  m(i,j)      +  b × m′(i,j);
                m(i-1,j-1)  =  m(i-1,j-1)  +  c × m′(i,j);
                m(i-1,j+1)  =  m(j-1,j+1)  +  c × m′(i,j);
                m(i+1,j-1)  =  m(i+1,j-1)  +  c × m′(i,j);
                m(i+1,j+1)  =  m(i+1,j+1)  +  c × m′(i,j);
                m(i-1,j)    =  m(i-1,j)    +  a × m′(i,j);
                m(i+1,j)    =  m(i+1,j)    +  a × m′(i,j);
                m(i,j-1)    =  m(i,j-1)    +  a × m′(i,j);
                m(i,j+1)    =  m(i,j+1)    +  a × m′(i,j);
        end
end
```

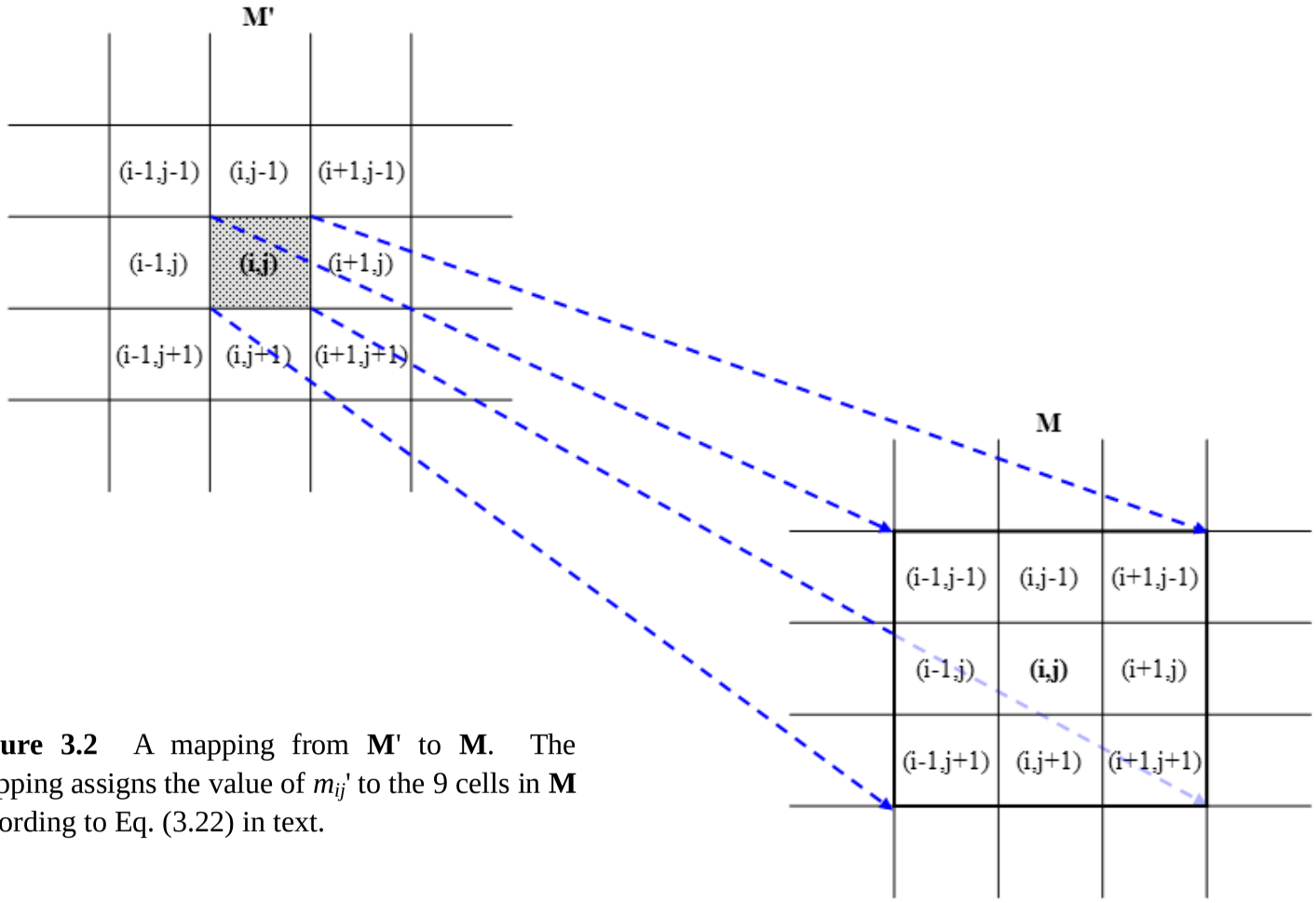

Figure 3.2 A mapping from **M'** to **M**. The mapping assigns the value of m_{ij}' to the 9 cells in **M** according to Eq. (3.22) in text.

3.5 Imaging resolution and quality

A complete model reconstruction can be established with the knowledge of a continuous data set. But in reality, digital data restrict the reconstruction results to the discretized form. The data are sampled in time and the signal records are measured in discrete spacing interval. The digital data are subject to the Nyquist sampling theorem (Shannon, 1949). Therefore, the spatial resolution is an important parameter of consideration during the inversion procedure to avoid aliasing artifacts.

The mapping from the data space to the model space is related to the background velocity field and the frequency contents of signals (Beylkin, 1985). Figure 3.3 shows two reflected rays from the neighbouring scatterers within a constant velocity field. The schematic is simple because it does not consider the spatially-varying velocity field where the rays bend. However the simplicity of the schematic is sufficient to illustrate the concept of spatial resolution of the reflections. The spatial separation, Δl, between the two reflected rays at an incident (or reflected) angle, θ is given by

$$\Delta l = \frac{c_0(\mathbf{x})\Delta t}{2\cos\theta} \tag{3.23}$$

where Δt is the sampling time interval related to the Nyquist frequency. For zero-offset case where $\theta = 0$, then (3.23) simplifies to

$$\Delta l = \frac{c_0(\mathbf{x})\Delta t}{2} \quad . \tag{3.24}$$

Either Eq. (3.23) or (3.24) provides a guidance for a theoretical minimum spatial resolution for the reconstructed image.

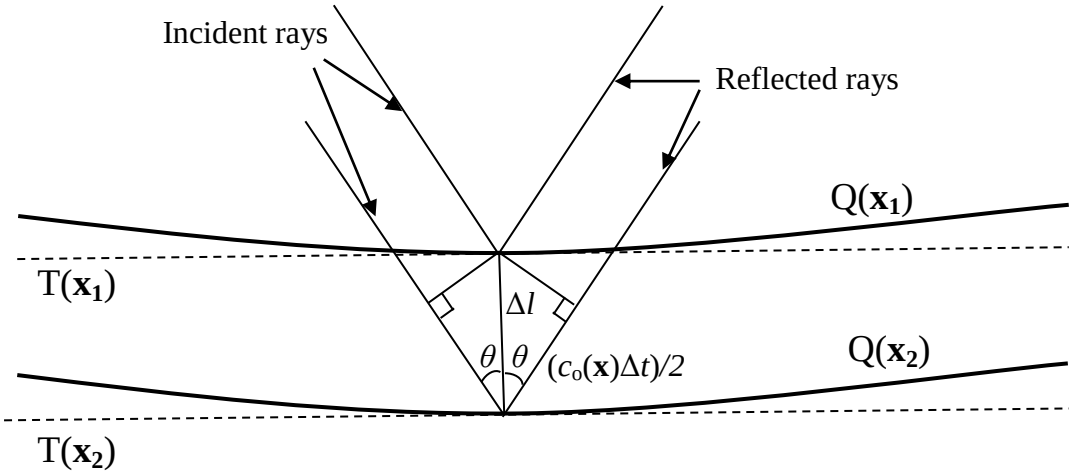

Figure 3.3 Geometry shows the spatial separation, Δl, between the two wavefronts $Q(\mathbf{x}_1)$ and $Q(\mathbf{x}_2)$ in a constant velocity field $c_0(\mathbf{x})$. T are the tangents to the wavefronts at the points of incidence. (modified from Miller *et al*, 1987).

According to (3.23) and (3.24), the spatial resolution for inversion is not related to the number of signal records. However, the bone samples should be adequately sampled along the acquisition axis so that sufficient ultrasound rays will pass through the pixels in the imaging space. This is to warrant a better reconstruction of the images when there is enough data to solve for the unknowns. On the other hand, if there are more rays passing through a scatterer, the signal-to-noise (SNR) of the corresponding reconstructed image is greatly increased by means of superposition. Figure 3.4 shows a set of three wavefronts (isochron surfaces) passing through the same point **x** (the scatterer) in the imaging space. The superposition of these three wavefronts will reduce random noise and enhance the SNR of the signals registered by the pixel. This will lead a reconstructed pixel image with better contrast.

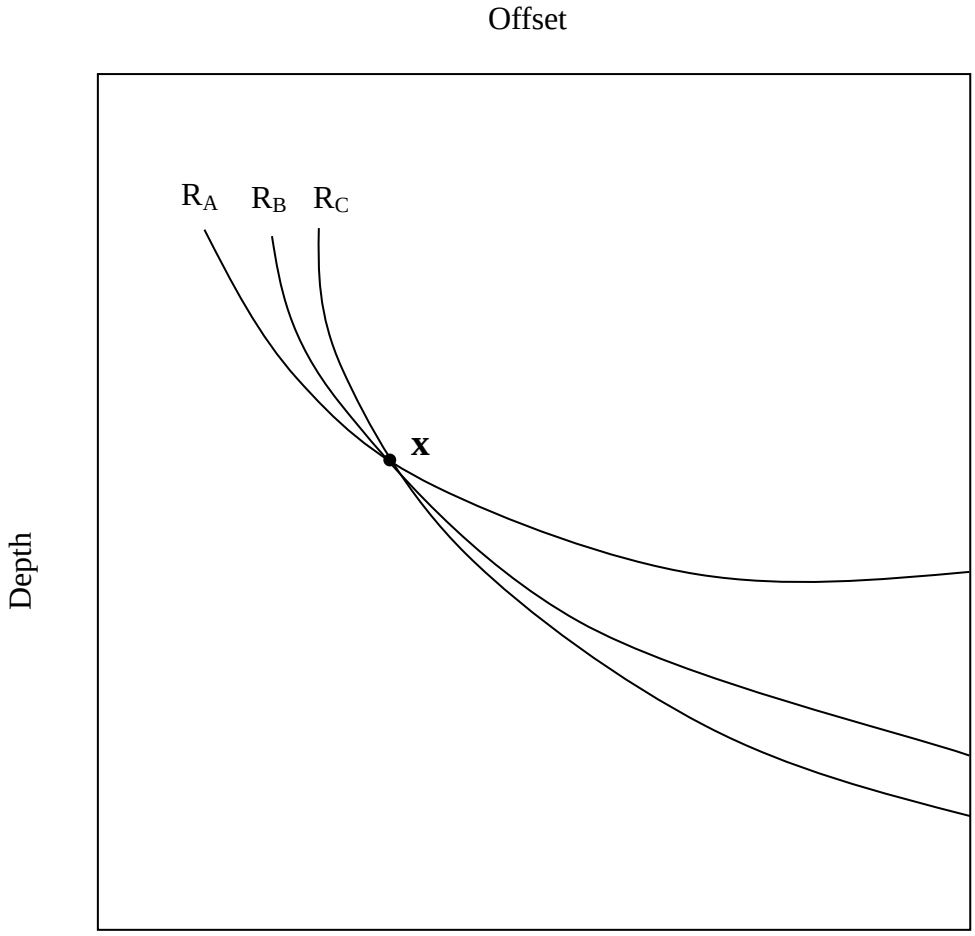

Figure 3.4 Three ray paths (R_A, R_B and R_C) pass through a point **x** in the model or image space.

3.6 A flow chart of the imaging procedure

Figure 3.5 shows the flow chart for the imaging process. We start with the data acquisition. The data undergoes signal processing and editing. The major goal of this step is to increase signal-to-noise ratio and remove the unwanted events such as multiple reflections. The processed data will be the input data, **D** ready for the inversion process. In parallel to this, the input background velocity is used to compute the travelled distance and travelling time between the pixel and the source/receiver pair. These parameters are then used to assemble the forward and adjoint operators, **L** and $\mathbf{L}^T$ according to Eq. (2.29) and (3.18). The data, **D** and the operators are then fed into the inversion engine to seek an optimal solution. For the inversion, one can choose the type of regularization such as ULS, DLS or WLS. The output of the iterative inversion procedure is the reconstructed image. Further image processing such as thresholding and interface enhancement will be used to display the reconstructed image.

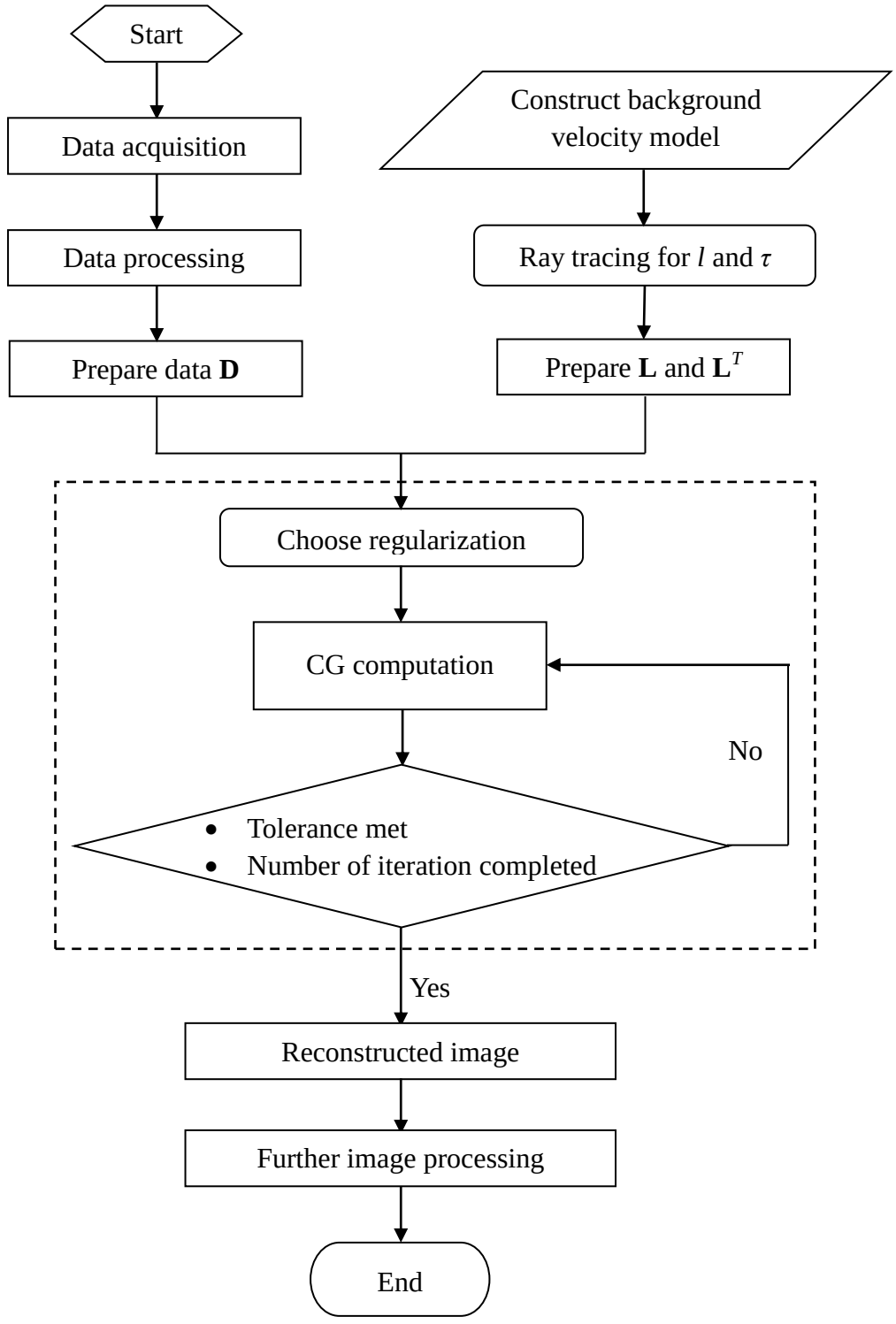

Figure 3.5 The flow chart for the imaging process. The box outlined in dashed line is the engine for the iterative regularization method. Tolerance is defined by the misfit error. In this thesis, we only use the number of iterations as the stopping criterion.

Chapter 4

Numerical validation and parameter analysis of the imaging algorithm

Numerical simulation is an important tool to verify the mathematical algorithms and theories. The simulated data are useful to assess the influence of various parameters upon the imaging results without the unwanted disturbance such as electronic noise from acquisition devices and scattering due to material inhomogeneities in real data. In this chapter, the inversion algorithms and methods are validated by applying the forward and inverse operators to the simulated data. The influence of several parameters such as frequency range, frequency sampling rate, beam aperture, source wavelet, noise level, temporal sampling interval, pixel size, spacing interval of acquisition, and inversion regularization, are investigated. Lastly, the inversion results using the optimal parameters and configurations are compared with the original model.

4.1 Inversion I: Verification of the inversion algorithm

In this section, the feasibility of the imaging algorithms and methodologies is verified by using the forward operator to simulate a numerical data set and using the inversion operations to reconstruct the images. The predicted data from the inversion result is compared with the synthetic data and the discrepancy is commented.

4.1.1 A bovine bone model

An X-ray CT image of a bovine femur was acquired (Figure 4.1A). The image matrix is 159×478 with the pixel dimension of 0.4 mm and each pixel position is set at the center of the grid cell. The CT image was converted into a velocity model by assigning appropriate speed of sound (SOS) to each grid cell proportional to the gray scale. In this example, the SOS of cortical bone is 4000 m/s, marrow is 1500 m/s and air is zero based on the experimental measurement and literatures (Camus *et al*, 2000; Muller *et al*, 2005). The velocity model was then transferred to a reflectivity model by taking the vertical difference of the image (Figure 4.1B). The background velocity model is made up of three layers where the top and bottom layers are cortex and the middle layer mimics marrow (Figure 4.1C).

4.1.2 Simulation and Inversion

The forward operator (Eq. [2.29]) was applied to simulate the numerical data set. The perturbation model used is the bone model shown in Figure 4.1B. Ray tracing was performed using the background velocity model (Figure 4.1C). The source wavelet is a negative Ricker pulse (Ricker, 1953) with a central frequency of 1 MHz. The sampling interval is 0.1 μs with a Nyquist frequency of 5 MHz. Two hundred and one records were simulated with a 0.8 mm spatial interval and each record has 1024 data points. An aperture of $\pm 40°$ and 0.1 – 3.0 MHz frequency range are used for both forward and inversion procedures. Figure 4.2 shows the simulated records. The forward operator simulates the primary arrivals from the three major interfaces (cortical/marrow, marrow/cortical and cortical/air) while ignoring the multiple reflections; the responses due to the heterogeneities at the right end of the bone model are also simulated.

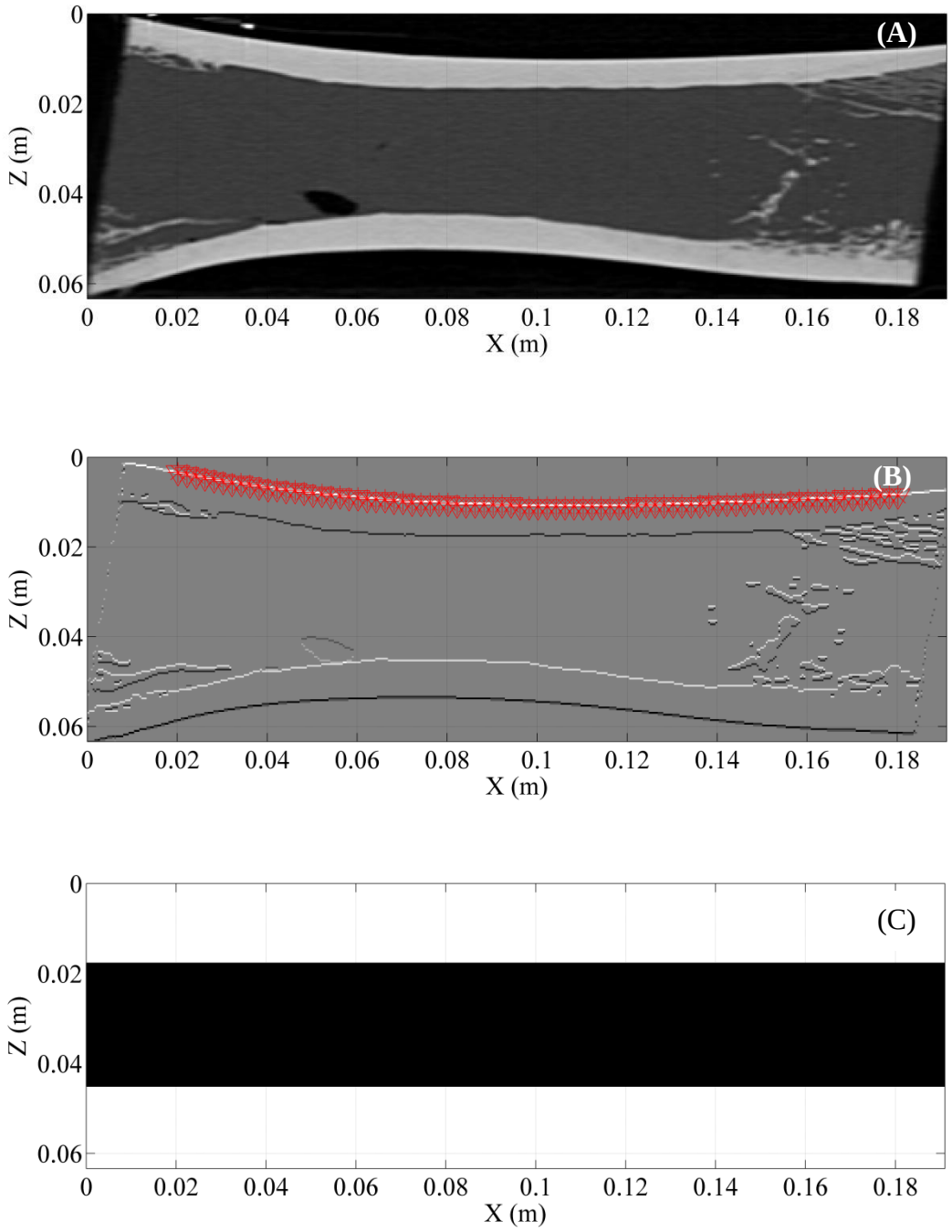

Figure 4.1 A bovine femur: (A) an X-ray CT image; (B) a reflectivity model. The asterisks and triangles indicate the source/receiver locations on the bone surface; (C) a background velocity model.

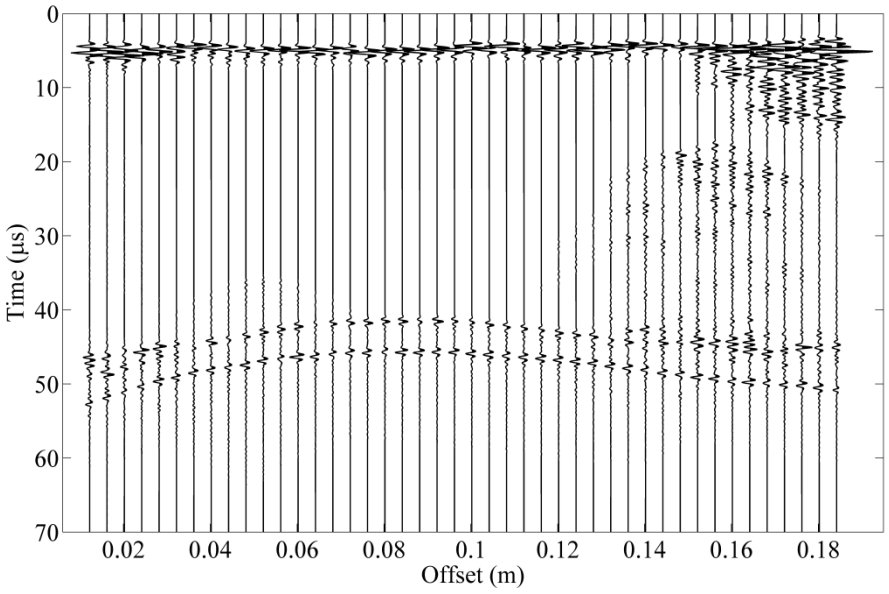

Figure 4.2 The synthetic data using the forward operator (Eq. [2.29]) and the bone model shown in Figure 4.1B.

Figure 4.3 shows the reconstructed image using the adjoint operator. The image shows a strong reconstructed upper cortex/marrow interface. The scattered inhomogeneities on the right side of the image around z = 0.02 m are also imaged. The lower marrow/cortex and cortex/air interfaces are visible but weak. Figure 4.4 shows the reconstructed results using the ULS and CG (ULSCG) methods with 28 iterations (Figure 4.4A). The CG method apparently provides a better reconstructed image which is closer to the original model (Figure 4.1B) than the adjoint operator. The upper cortex/marrow interface is much better defined with good resolution. The lower marrow/cortex and cortex/air interfaces are also reconstructed with strong reflectivities. The CG-reconstructed interfaces and edges are more distinct from the background and the image illustrates clearly the

details of the inhomogeneities. Nevertheless, both (adjoint and ULSCG) show reconstructed artifacts. The artifacts are apparent at both ends of the lower interfaces (between z = 0.04 and 0.06 m, x < 0.02 m and x > 0.18 m) where the recovered interfaces are curving upwards instead of downward as in the original model. The misfit (Figure 4.4B) is significantly reduced after 5 iterations and trends to a comparably stable level after 10 iterations. The predicted data were computed by applying the forward operator to the reconstructed reflectivity model (Figure 4.4A) using the same parameters as those for the synthetic data. Figure 4.5 shows the comparisons between the synthetic and predicted data. The reconstructed error, which is the difference between these two data sets, is amplified 20 folds (Figure 4.5C).

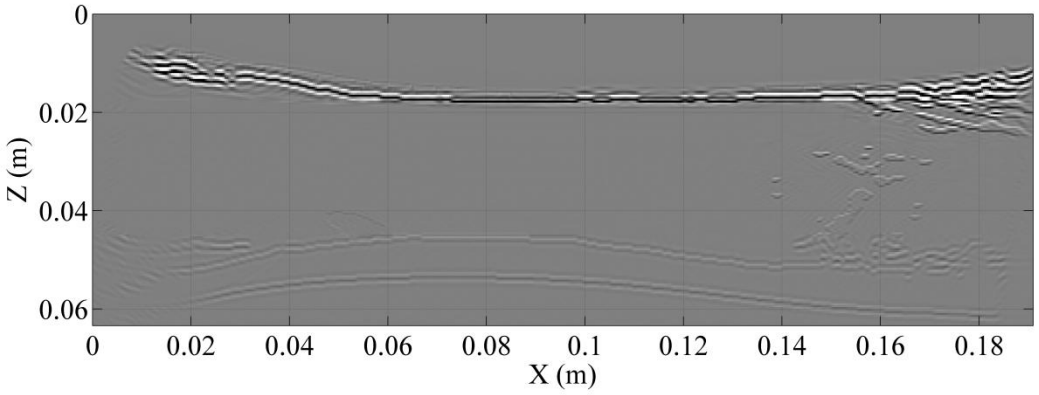

Figure 4.3 The reconstructed image of the synthetic data shown in Figure 4.2 using the adjoint operator.

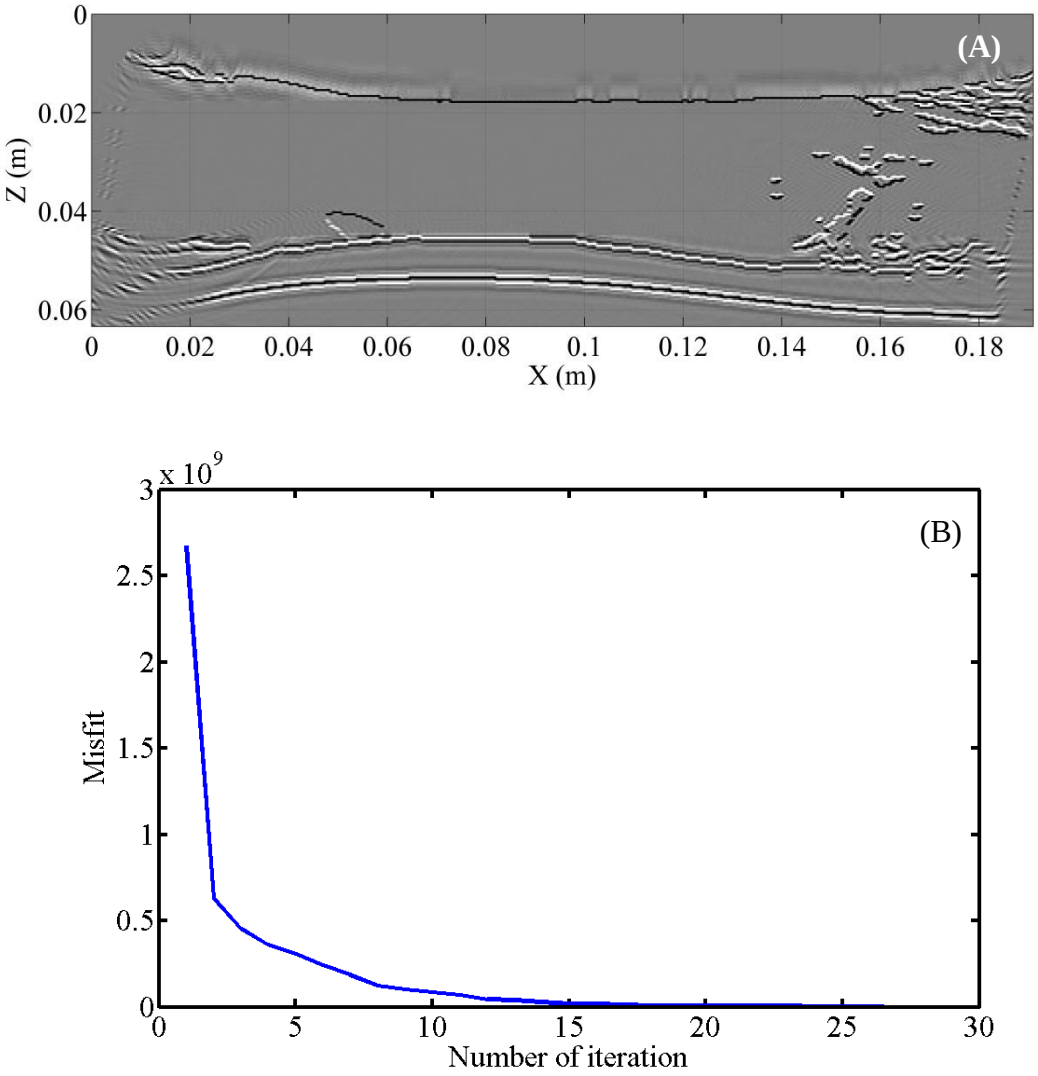

Figure 4.4 Inversion of the synthetic data shown in Figure 4.2 using the ULSCG method: (A) The reconstructed image (28 iterations) and (B) the misfit curve.

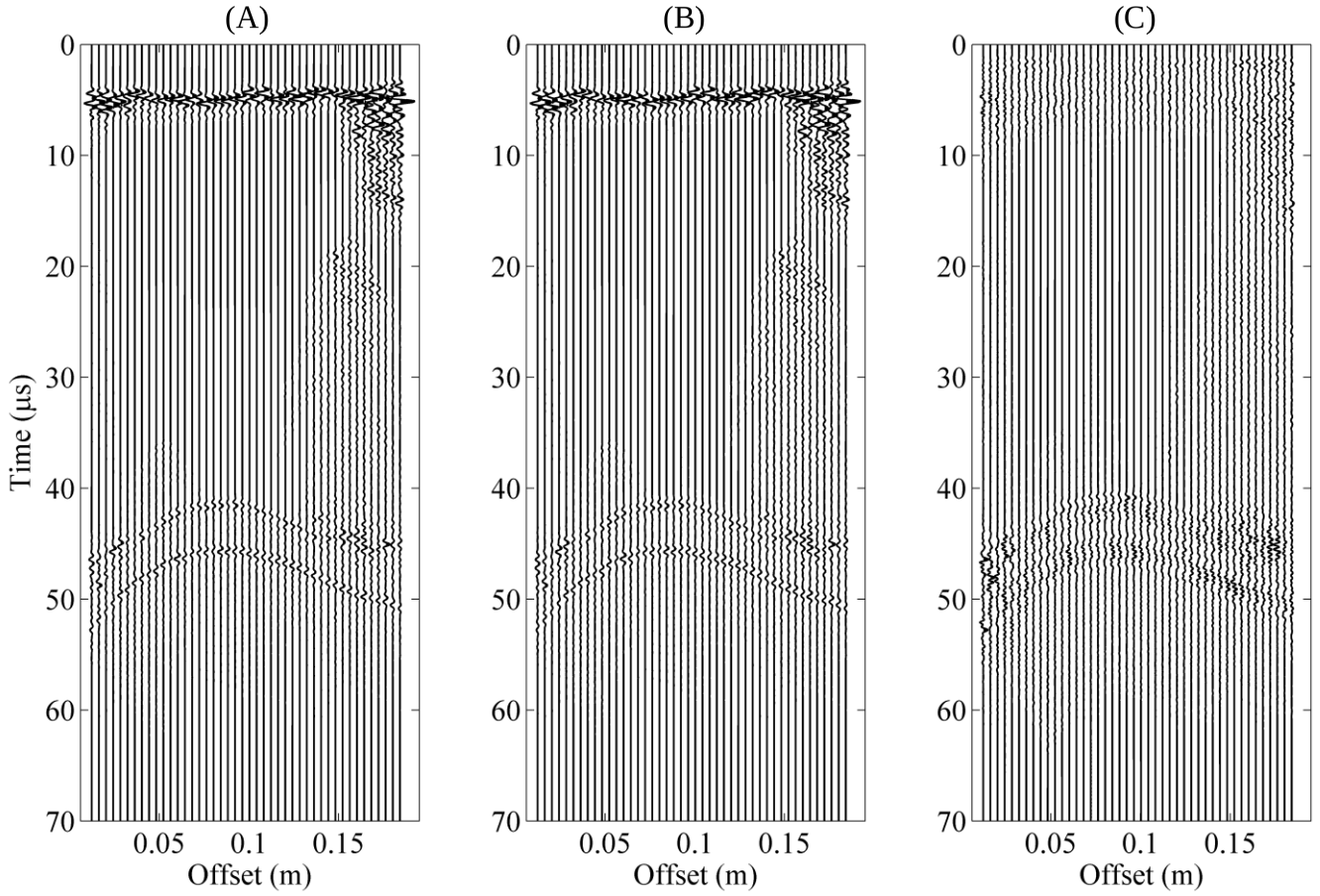

Figure 4.5 Comparison between the synthetic and predicted data: (A) the synthetic data from Figure 4.2; (B) the predicted data computed using the forward operator and the reconstructed image (Figure 4.4A); (C) the difference between the synthetic and predicted data. The image is amplified by a factor of 20 to illustrate the reconstructed errors.

There are two areas where the reconstructed errors are bigger. The first area is the lower marrow/cortical and cortical/air curved interfaces. This corresponds to the area bounded between 40 – 50 μs in the time section (Figure 4.5C). The data has low signal-to-noise ratio due mainly to signal attenuation by spherical divergence. The second area is close to the right end of the bone sample where many small scattering inhomogeneities exist. The area is around 10 μs at offset greater than 0.15 m in the time-offset section (Figure 4.5C). In this region, scattered signals from the small inhomogeneities give rises to the incoherent waveforms, which is difficult for the algorithm to back-project the wavefields perfectly. However, the errors are very small and are not noticeable without amplification.

Based on the simulation experiment, the forward and adjoint operators appear to be effective operators to reconstruct the image. The reconstructed interfaces compare well with the reflectivity model. However, at the edges of the image, the algorithm has difficulty to reconstruct the interfaces properly.

4.2 Inversion II: Analysis of inversion parameters

In this section, the influence of some inversion parameters on the reconstructed images has been studied. These parameters are variables of the forward (Eq. [2.29]) and adjoint operators (Eq. [3.18]). They are frequency range, frequency sampling rate, beam aperture, source wavelet, and noise level. The numerical data was simulated by the convolution of the source wavelet with the reflectivities. Only primary arrivals were simulated without multiple reflections. As compared to finite difference method, which renders a full wave solution, the convolved data provide a less sophisticated and undisturbed numerical set to study the relevant parameters.

The adjoint operator with an aperture of $\pm 5^\circ$ was used in all the inversion operation unless specified otherwise in the later part of this chapter. For all the simulation and real bone experiments, the first interface of the bone images, which is the air/cortical interface, is predetermined by the source/receiver locations. This interface is indicated as a solid black curve in the subsequent reconstructed images. For the reconstructed image matrix, the depth (z) series at a fixed x position shows oscillatory waveforms. The amplitude of the waveforms close to the top interfaces is usually strong. In order to extract an interface from the waveforms, we applied two thresholds to pick the peaks and troughs of the waveforms. The two thresholds are not the same in absolute value but the positive threshold is usually larger than the negative threshold in value. Ideally, the levels of thresholds are set such that only a peak or trough is picked. Then the peak is indicated by red color while the trough by blue color. The colors used in this context emphasize the locations and continuities of the interfaces and do not have any relation to reflectivities. The threshold levels, once determined, are fixed for all the reconstructed images in this chapter.

The computer used is a desktop PC with an Intel® Core™ 2 Duo 2.66 GHz processor with Windows XP operating system. The programming software is MATLAB R2009a.

4.2.1 The simulated records

The sample is a bovine tibia and 237 mm long, 35.2 mm thick in the mid shaft, and 51.1 mm thick at the left end. An X-ray CT image of the sample was acquired (Figure 4.6A). The image was then converted to a velocity model (Figure 4.6B) by assigning different colors to different gray scales: air (white pixel), bone marrow (gray pixel) and cortical bone (black pixel) with the cancellous bone at

the both ends removed. Figure 4.6B shows the velocity model with three distinct layers: upper cortex, marrow, and lower cortex, which will be used as a background velocity model for ray tracing.

To seek a better estimation of the velocities for the cortex and marrow, we used a similar experimental method described by Zheng *et al* (2007). The reflection times of the echoes from the cortex/marrow and the marrow/cortex interfaces were measured using a group of time signals in the mid-shaft where the cancellous bone is less and the cortical tissue is more homogenous. The one-way travelling time is half of the reflection times. The thickness of the upper cortex and the marrow layer were measured in the relevant portion of the CT image. The one-way travelling time versus thickness data were best fitted by linear regression. The estimated cortical velocity is 3441 m/s and the marrow is 1434 m/s. The velocity of air is considered as zero to simplify the inversion procedure.

Given a source/receiver pair, the arrival time of the echoes for normal incidence can be calculated by

$$t_i = \sum\left(\frac{2h_i}{V_i}\right) \quad (i = 1, 2, 3) \tag{4.1}$$

where h_i is the thickness of the ith layer in the model image and V_i is the corresponding velocity of the ith layer. At the arrival times of the echoes, unit impulses are assigned to mimic reflectivity, $r(t)$. Then the simulated signals $d(t)$ for any source wavelet $s(t)$ are

$$d(t) = r(t) \otimes s(t) \tag{4.2}$$

where $\otimes$ is the convolution operator.

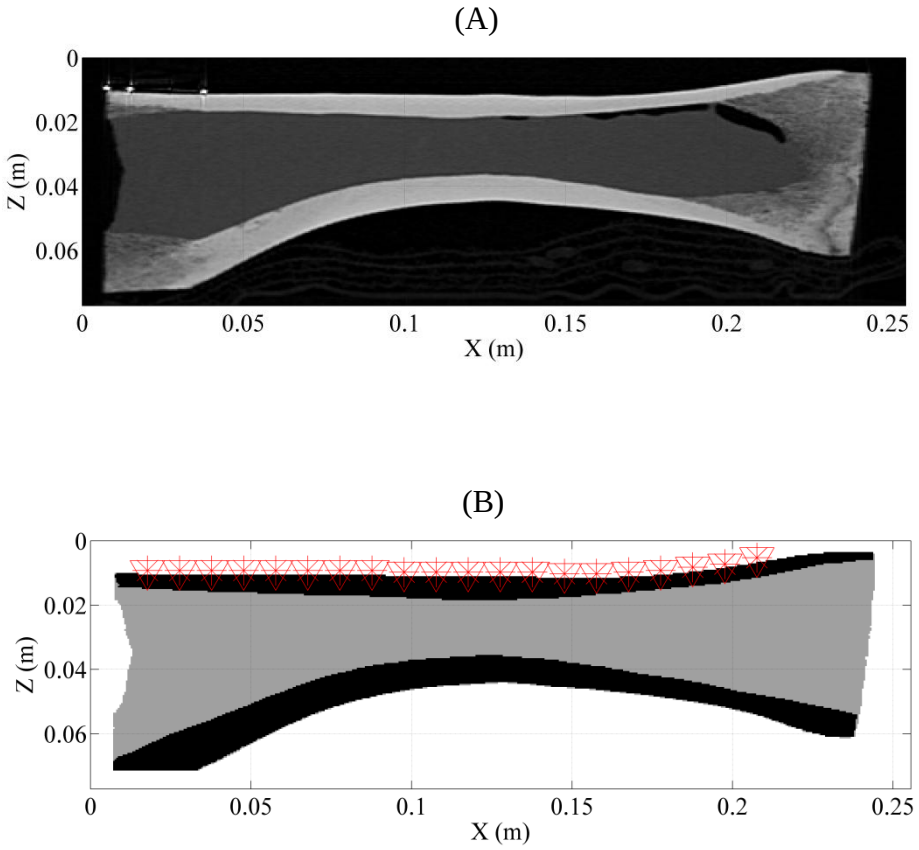

Figure 4.6 A bovine tibia sample: (A) a CT image, and (B) a velocity model converted from the CT image. The asterisks and triangles indicate the source/receiver pairs.

The source wavelet used was generated by a Panametrics CHC706 (Panametrics, Waltham, MA) dual-head *P*-wave composite transducer. Figure 4.7 shows the time signal (Figure 4.7A) and the amplitude spectrum (Figure 4.7B) respectively. The nominal center frequency of the transducer is 2.25 MHz but the spectrum peaks at 2.02 MHz. The useful frequency range is 0-4 MHz.

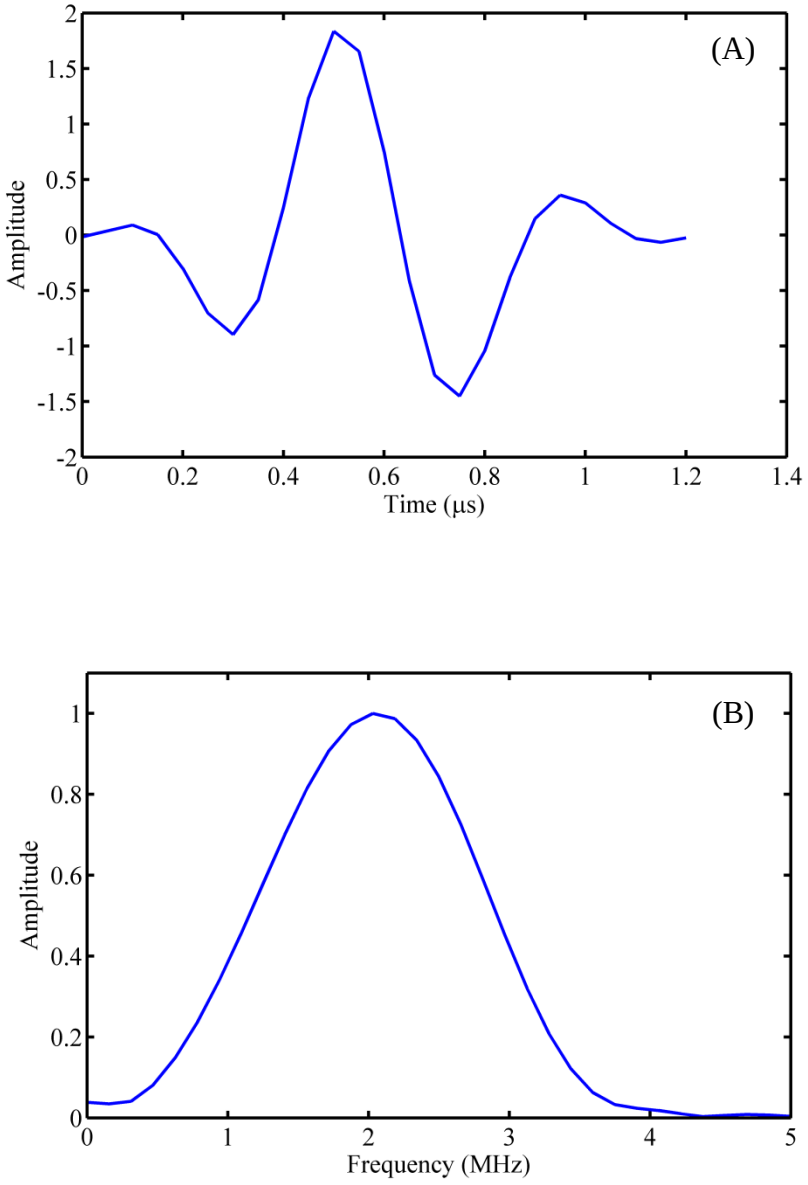

Figure 4.7 An experimental source wavelet in (A) time domain and (B) frequency domain.

395 records were simulated with a spatial interval of 0.5 mm. Each record has 1800 data points with a time step of 0.05 μs ($f_{Nyquist}$ = 10 MHz), i.e., the length of the signal is 90 μs. The first measurement station is 17.7 mm from the left edge of the bone sample (see Figure 4.6B) and the last measurement station is 214.6 mm away. Figure 4.8A and 4.8B show a simulated signal and its frequency spectrum. Figure 4.8C shows a portion of the simulated time records with self-normalization. The reflections from three major interfaces were simulated. For this simulated data set, spherical divergence, partition of ultrasound energy at the interface, attenuation, and multiple reflections were not considered. The ultrasound beams were considered to travel straight down through interfaces without refraction due to interface curvatures.

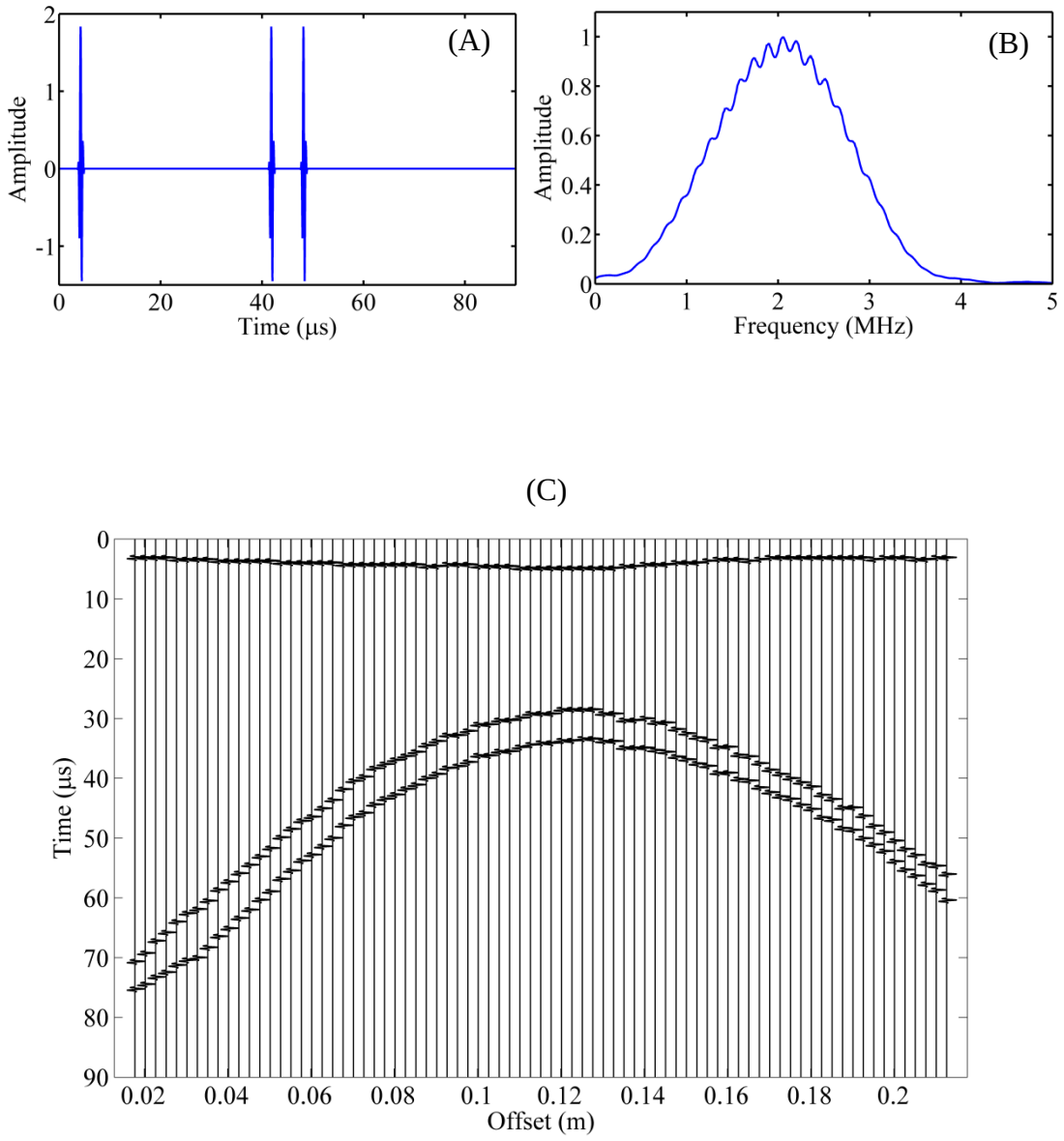

Figure 4.8 The simulated data using the convolution method: (A) a single convolved signal; (B) the amplitude spectrum of the signal shown in (A); (C) a section of 395 simulated records with each record self-normalized by itself.

4.2.2 Analysis of inversion parameters

In this section, the influence of five parameters upon the reconstructed results will be examined. The five parameters are frequency range, frequency sampling rate, beam aperture, source wavelet, and noise level. In order to better present the reconstructed details of the interfaces, the inverted images were subsequently plotted in a 1:2 scale in the (x,z) space. The discussion is mainly based on the visual observations of the reconstructed images and the computation cost of the inversion operation.

4.2.2.1 Frequency range

Figure 4.9 shows the inversion results for three different frequency ranges. In Figure 4.9A, the 1-3 MHz range is used, which covers about 80 percent of the signal spectrum (0.1-5 MHz) shown in Figure 4.8B. The artifacts, as indicated by the arrows, are apparently observed within the boundaries of the first cortical layer in the reconstructed image. This is due to the frequency cut-offs at both ends. As shown in Figure 4.9B, when the 0.1-5 MHz range is used, the artifacts disappear. When the frequency range expands to 0.1-10MHz, the reconstructed image is not significantly improved (Figure 4.9C) but the computation time is doubled and increases from 1588 seconds to 3226 seconds.

Properly selected frequency range could reduce the computation cost without compromising the image quality. For example, comparing with the full range inversion (up to Nyquist frequency), the half range (0.1-5MHz) reduces the computation time to half. However the selected frequency range should cover the major portion of the signal spectrum; otherwise the aliasing due to the frequency cut-off will introduce artifacts.

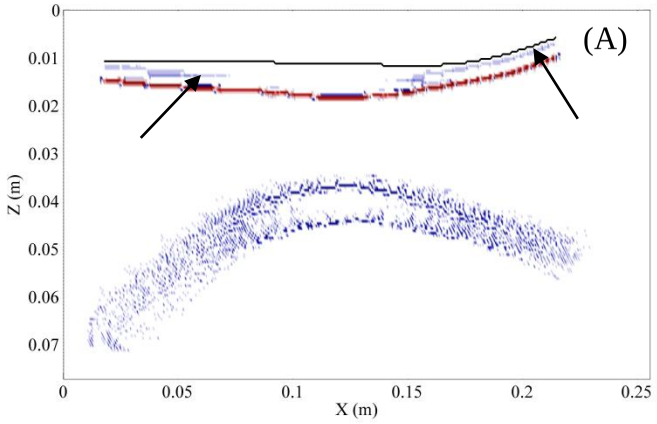

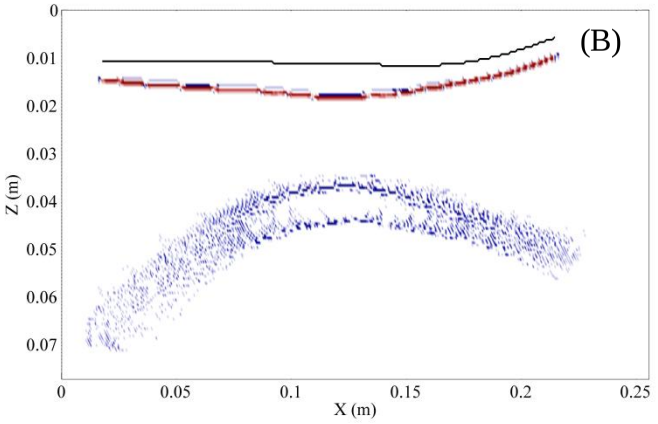

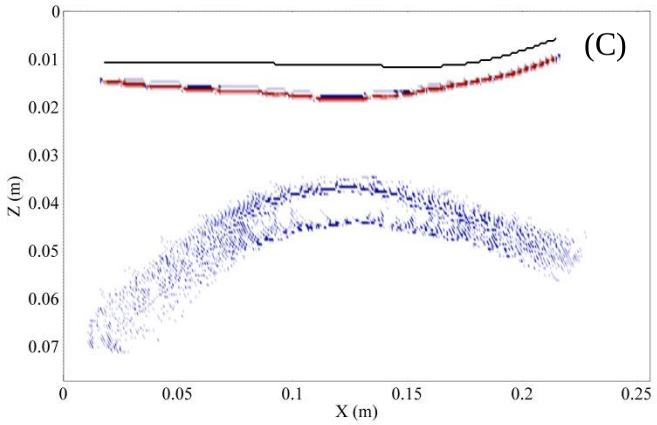

Figure 4.9 The reconstructed images under different frequency ranges: (A) 1-3 MHz; (B) 0.1-5 MHz ; (C) 0.1-10 MHz. The arrows in (A) indicate the artifacts.

4.2.2.2 Frequency sampling rate

With the Nyquist frequency fixed at 10 MHz, three cases are studied with different frequency sampling rates (i.e. different number of FFT points): 90 points/MHz, 180 points/MHz, and 360 points/MHz respectively. Given the same frequency range of 0.1-5MHz, the numbers of frequency components used to calculate each pixel value for each sampling rate are 441, 882, and 1764 respectively and therefore the computation cost increases accordingly. Figure 4.10 shows the inversion results for three frequency sampling rates. The image with the most FFT points (Figure 4.10C) provides the best image with sharp interfaces. Nonetheless the other two images (Figures 4.10A & B) also recover the major structures with less calculation. In this case, increasing the number of frequency points or decreasing the frequency interval only improves the inversion results marginally. The inversion results with 90 points/MHz are acceptable.

Having more data points for the signals does not seem to pose a challenge in real case. We always acquire more data points than we need during the acquisition with a fixed temporal sampling interval. Padding with zeros is also a possibility. This will guarantee enough number of FFT points to be used in the inversion procedure.

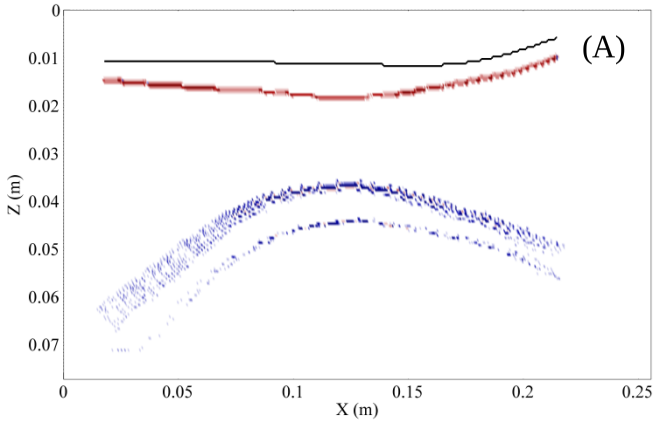

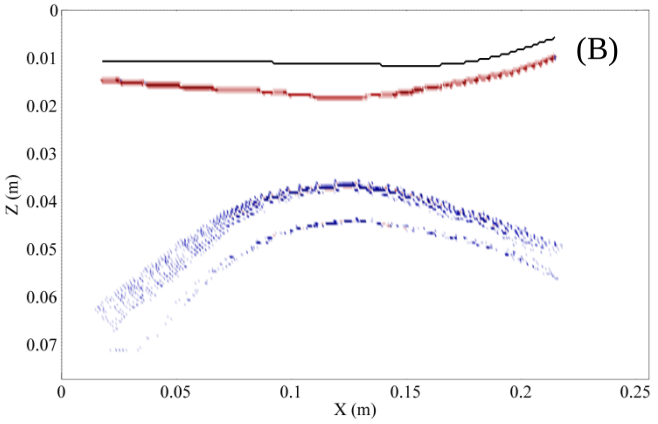

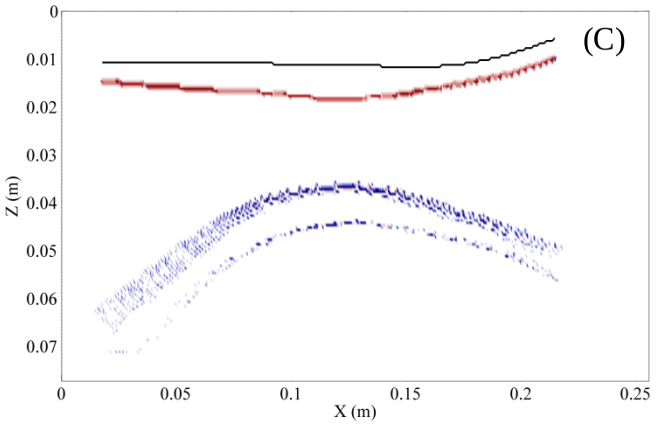

Figure 4.10 The reconstructed images using different frequency sampling rates where the Nyquist frequency is 10 MHz (Δt = 0.05 μs): (A) 90 points/MHz, (B) 180 points/MHz, and (C) 360 points/MHz

4.2.2.3 Beam aperture

As discussed in Section 2.3.1, the use of beam aperture will reduce computational effort; it also has physical relevance to the beam characteristics of a transducer. The larger the aperture window, the more pixels will be used for the inversion. Here, I would like to investigate the effect of the aperture from $\pm 1°$ to $\pm 60°$ on the quality of the reconstructed images

Figure 4.11 shows the inversion results for six ultrasound beam apertures: $\pm 1°$, $\pm 5°$, $\pm 10°$, $\pm 20°$, $\pm 40°$, and $\pm 60°$. For $\pm 1°$ aperture (Figure 4.11A), the reconstructed interface of the top cortical/marrow appears discontinuous lengthwise, which is evident due to polarity changes across the interface. The interface artifact arises because the amount of data used for inversion is limited due to small aperture coverage and thus provides insufficient information for the reconstruction, especially in the part of the structures with large curvature. For example the discontinuity is more serious at the right end of the first interface where the interface is more curved as compared to the middle section.

Contrarily, if the aperture is large such as $\pm 20°$ (Figure 4.11D), $\pm 40°$ (Figure 4.11E), and $\pm 60°$ (Figure 4.11F), more data within the aperture window are available for the reconstruction. The drawback is that by including more pixels, scattering and averaging will be enhanced, leading to serious blurring of the interfaces. The reconstructed interfaces start to lose sharpness especially at large apertures. The blurring effect is evident in all three reconstructed images, especially in Figure 4.11F where the aperture is the largest.

With all other parameters held constant except the beam aperture, the computation times for $\pm 1°$, $\pm 5°$, $\pm 10°$, $\pm 20°$, $\pm 40°$, and $\pm 60°$ are 103 sec, 409 sec, 799 sec, 1588 sec, 3666 sec, and 7651 sec respectively.

In summary, for zero-offset case, small apertures such as ±5-10° are relatively suitable for inversion procedure because the reconstruction operation is more efficient, faster, and yields better image quality. The 5° aperture will be used for all subsequent inversion experiments hereafter.

4.2.2.4 Source Wavelet

Figure 4.12 shows the inversion results for two source wavelets: the experimental wavelet and Ricker wavelet. As described in Section 4.2.1, the experimental wavelet was generated by a commercial transducer used in our experiment. The Ricker wavelet has a center frequency of 2.0 MHz. The two results are comparable in terms of image quality while the reconstructed image using the experimental wavelet is more emphasized against the background, i.e., the recovered interfaces have greater strength as shown in Figure 4.12A. The experimental wavelet is easily measured for any transducer and, in situation where the source wavelet is not known, can be used for the inversion of more complex model.

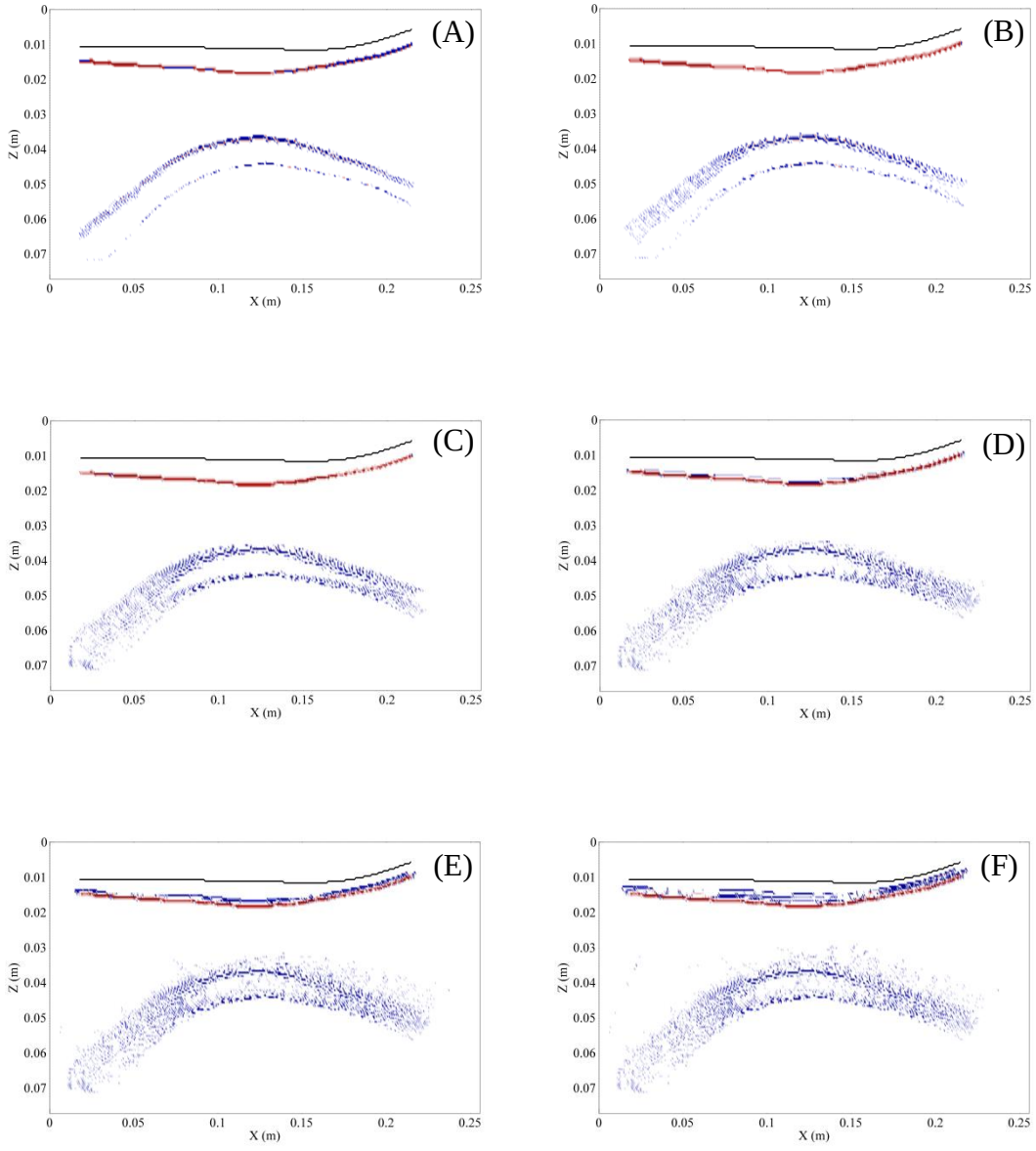

Figure 4.11 The reconstructed images with different beam apertures: (A) ±1 °, (B) ±5 °, (C) ±10 °, (D) ±20 °, (E) ±40 °, and (F) ±60 °.

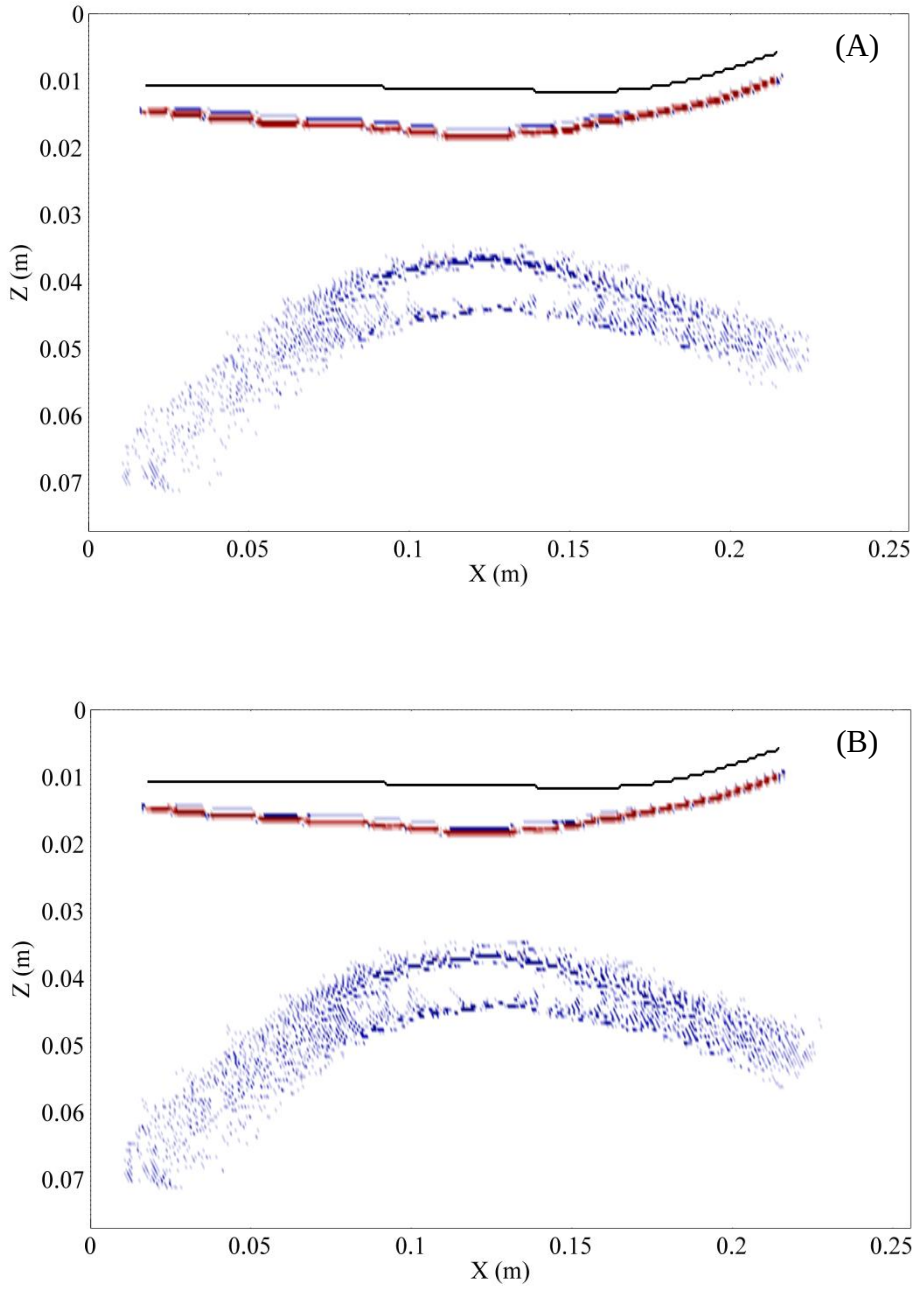

Figure 4.12 The reconstructed images with different source wavelets: (A) the experimental wavelet (Figure 4.7) and (B) the Ricker wavelet.

4.2.2.5 Noise level

To study the influence of noise level upon the inversion results, three noisy data sets were generated by adding normally distributed random noise to the noise-free signal. The simulated time signals for noise-free case, 5%, 10%, and 20% noise level are presented respectively in Figure 4.13A-D. Figure 4.13E shows the group of data set with 20% noise level. The percentage refers to the noise-to-signal peak ratio.

Figure 4.14 shows the inversion results for different noise levels. Comparing to the noise-free reconstructed image (Figure 4.14A), the quality of the reconstructed images is reduced with the increase of noise level. In Figure 4.14D, the noise can be clearly seen in the reconstructed cortex layer. The experiment demonstrates that the noise is detrimental to the image quality. However, the image quality is acceptable for noise up to 5% level. But for higher noise level, filtering should be used to reduce noise and enhance signal-to-noise ratio in order to improve image quality.

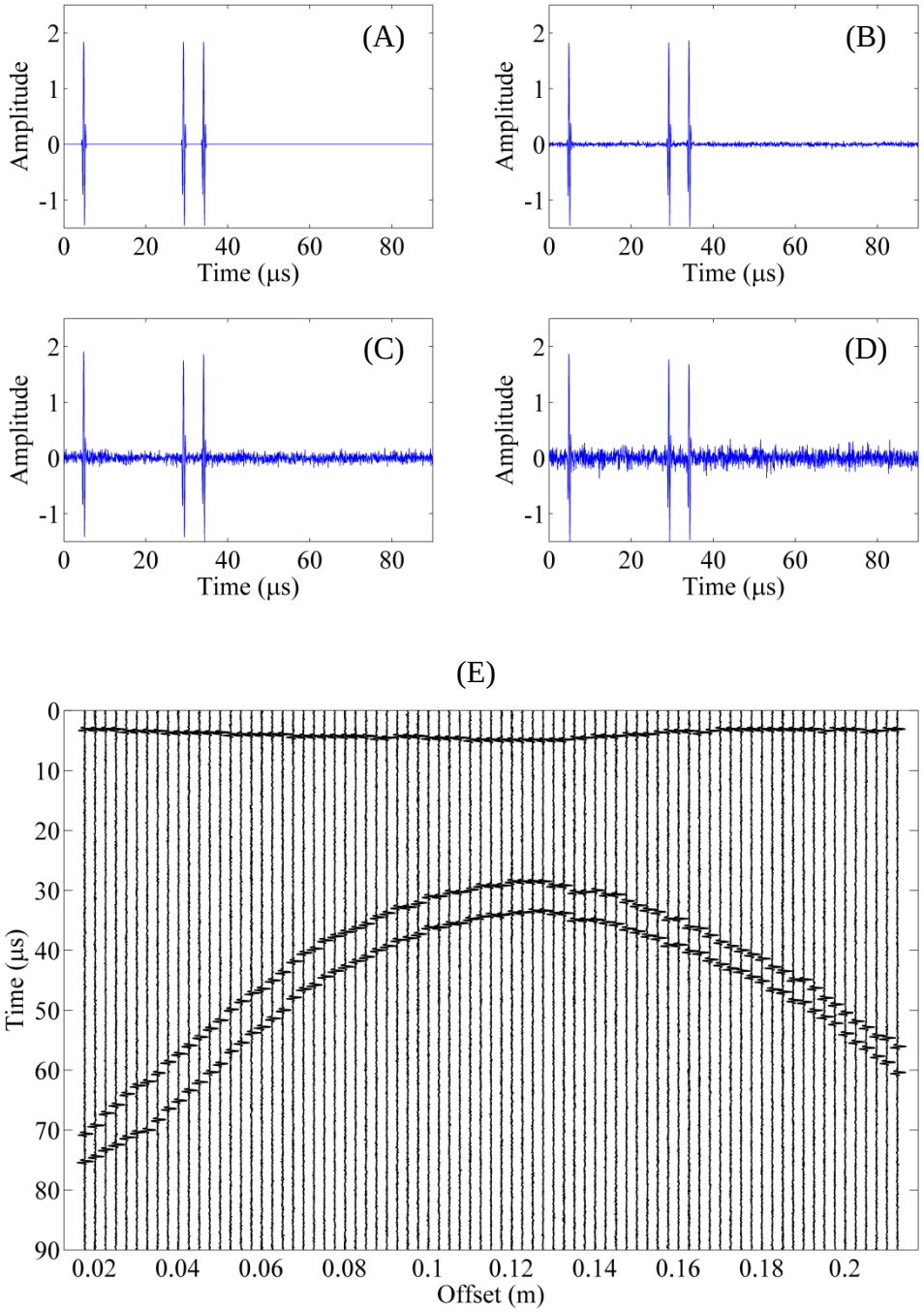

Figure 4.13 The simulation data using the convolution method with different noise level: (A) noise free record, (B) 5% noise, C) 10% noise, (D) 20% noise, and (E) a section of 199 records with 20% noise level. The time records for the section are self-normalized.

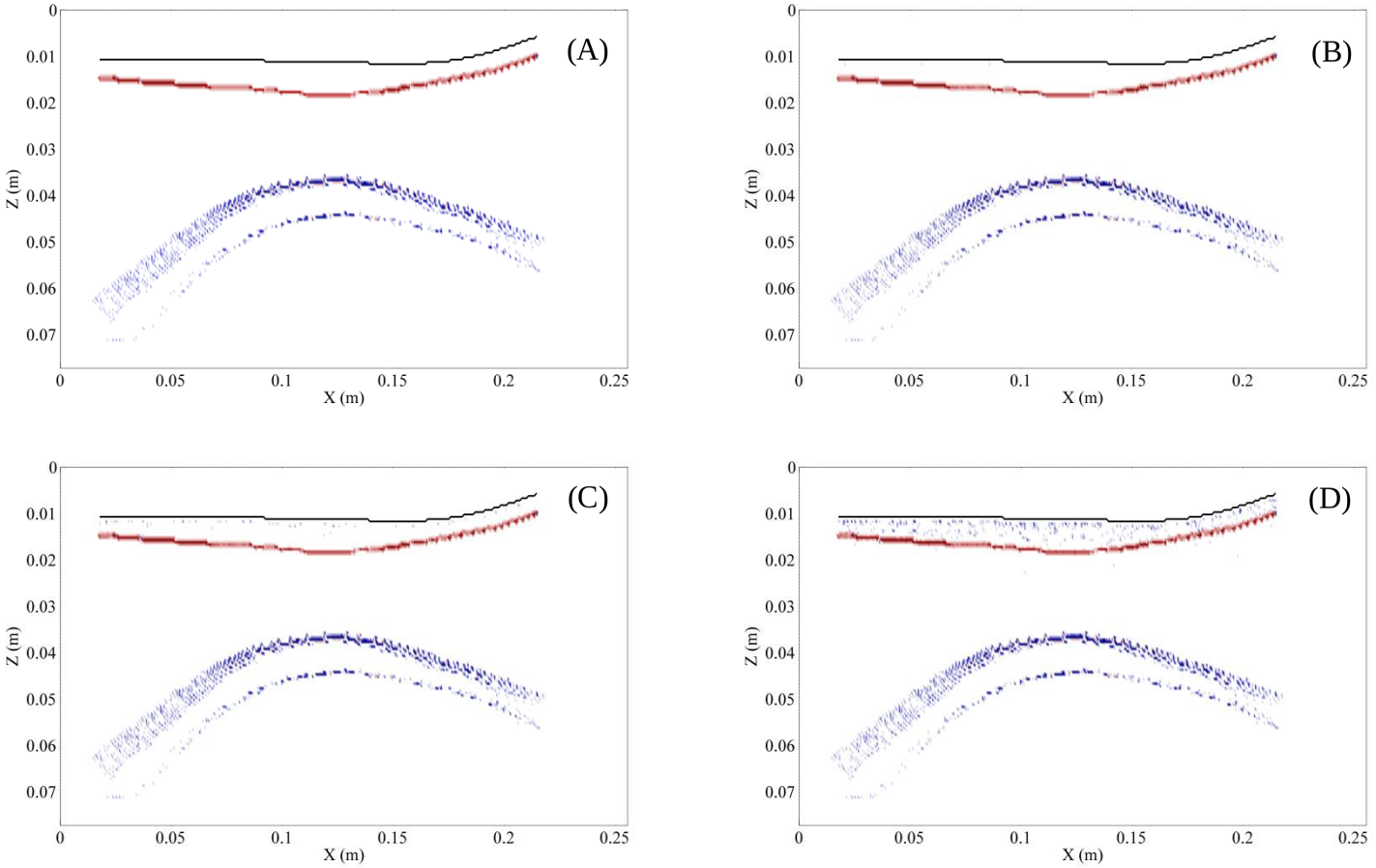

Figure 4.14 The reconstructed images for different noise level: (A) noise free, (B) 5% noise, (C) 10% noise, and (D) 20% noise.

4.3 Inversion III: Analysis of inversion parameters

In this experiment, a data set was simulated using a commercial software package, Wave2000 (CyberLogic Inc., New York, NY). The software is based on the finite difference (FD) implementation of elastic wave equation; however only the acoustic condition was applied in this case. The simulated data set is close to the real bone data and contains all wave phenomena such as spherical divergence, multiple reflections, absorption, scattering, and refraction at the curved structures. With this data set, I further examine the influence of some other inversion parameters upon the image quality of the reconstructed images. These parameters are temporal sampling interval, pixel size of the image matrix, acquisition spatial interval (number of the signal records) and regularization methods.

4.3.1 The simulated records

The bone model used is shown in Figure 4.6, the same model used for previous convoluted data set (Section 4.2). The SOS values remain to be 3441 m/s, 1434 m/s, and 0 m/s for cortical bone, marrow, and air respectively. The assigned attenuation coefficients are 4.91 dB/MHz/cm (Zheng *et al*, 2007), 0.1 dB/MHz/cm, and 93.4 dB/MHz/cm for cortical bone, marrow, and air. Pulse/echo mode was used to imitate the zero-offset configuration; the signal records were computed for one transducer's position at a time to simulate the real acquisition situation with one single transducer. Due to the full wave simulation of FD algorithm, the receiver was supposed to receive all scattered signals including specular reflections from all directions due to any inhomogeneities. The same experimental source wavelet as shown in Figure 4.7 was used. 199 records were calculated with a spatial interval of 1 mm. Each record is 90 μs long with 6667 data points and a time step of 0.0135 μs.

Figure 4.15A shows a simulated section of 199 records. Besides the primary reflection from the top cortex/marrow interface, the multiply reflected energy following the primary event is also seen (indicated by red arrows). The presence of material absorption, energy diminishing with travelled distance, and energy partition at the interface during wave propagation reduces the amplitudes of the reflection signals significantly, especially from the two lower interfaces. The small amplitudes of the late arrivals can influence the inversion results and reduce the image quality, even greatly affecting the reconstruction accuracy.

Several signal processing steps were applied to the simulated data. Firstly, all the records were decimated 3 times, leaving a record length of 2224 data points with a time interval of 0.0405 μs. The Nyquist frequency is about 12.5 MHz. A 0.5/0.7/2.5/3.0 MHz bandpass filter was used to remove the low and high frequency noise. The multiple reflection from the top cortical/marrow interface (the small responses after the primary reflection as indicated by the red arrows in Figure 4.15A) was also removed because only primary reflections from the structures are considered in the Born-based algorithm. The data were also time-gain compensated. Figure 4.15B shows the data after signal processing. The three reflection events correspond to the three interfaces in Figure 4.6. There is evidence of signal loss, which is lacking in the convolution-based data (see Figure 4.8C); for example the reflections from the marrow/cortical and the cortical/air interfaces (see blue circles in Figure 4.15B) are highly attenuated and not visible without significant time-gain compensation. In real bone data, it is unlikely the echoes from these areas will be observed due to curvature of the interfaces and the receiving aperture of the transducer. This will be discussed in Chapter 5.

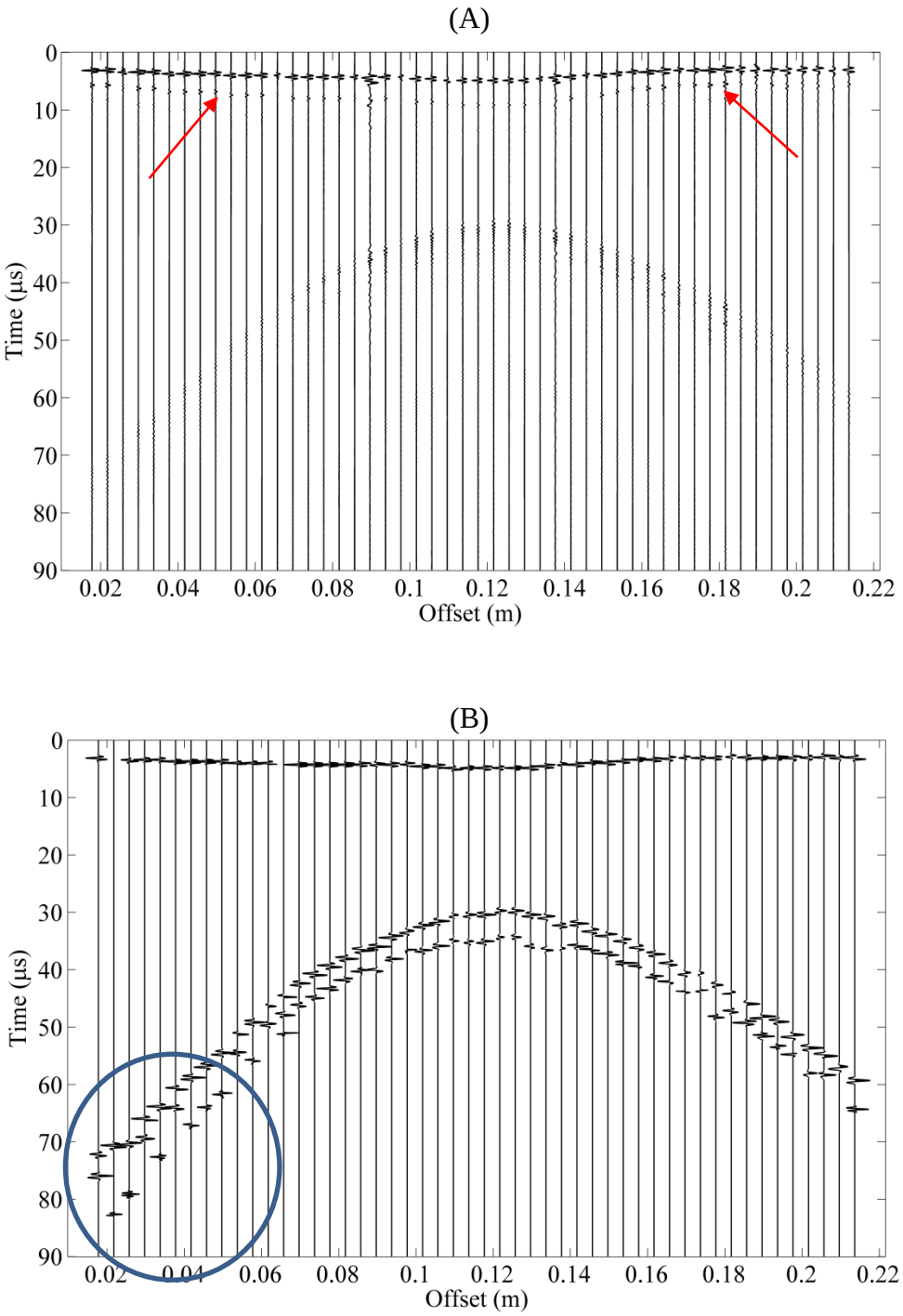

Figure 4.15 Simulation using the commercial finite difference software (Wave2000, CyberLogic, NY): (A) the simulated data with the red arrows indicating the multiple reflections and (B) the data after signal processing with self-normalization, while the blue circle indicates the signal loss in the reflection from the cortical/air interface comparing to Figure 4.8C.

4.3.2 Analysis of inversion parameters

Similarly to Section 4.2, the same background velocity model (Figure 4.6B) was used for ray tracing. The frequency range is set to 0.5-3 MHz, and correspondingly 222 frequency components were used for the inversion process. The beam aperture is $\pm 5°$. Four parameters have been examined: temporal sampling interval, pixel size, spacing interval of acquisition (number of the signal records) and different inversion regularizations.

4.3.2.1 Temporal sampling interval

The Nyquist frequency determines the sampling interval of the signal and vice versa. Figure 4.16 shows two reconstructed images based on two sampling intervals: 0.040 μs (f_{Nyquist}=12.5 MHz) and 0.081 μs (f_{Nyquist}=6.25 MHz). Even though the latter sampling frequency is half of the former, the 3 MHz frequency spectrum of the signal is well below the allowable maximum frequency. However as illustrated in Figure 4.16B, the coarse time interval results in blurred reconstructed interfaces. Comparing to Figure 4.16A with finer Δt, the first reconstructed cortical/marrow interface is broader with at least two cycles of waveform. For the lower interfaces, the reconstructed interfaces are less sharp and not well defined, especially where the interfaces are curved. Also the lower structures lost more information, for example the missing part of the cortical/air interface as indicated with red circle.

The loss of resolution results from the reduced signal data points due to bigger sampling interval Δt. Moreover, if we recall the spatial resolution Eq. (3.24), the spatial resolution of reconstructed image decreases with the increase of Δt.

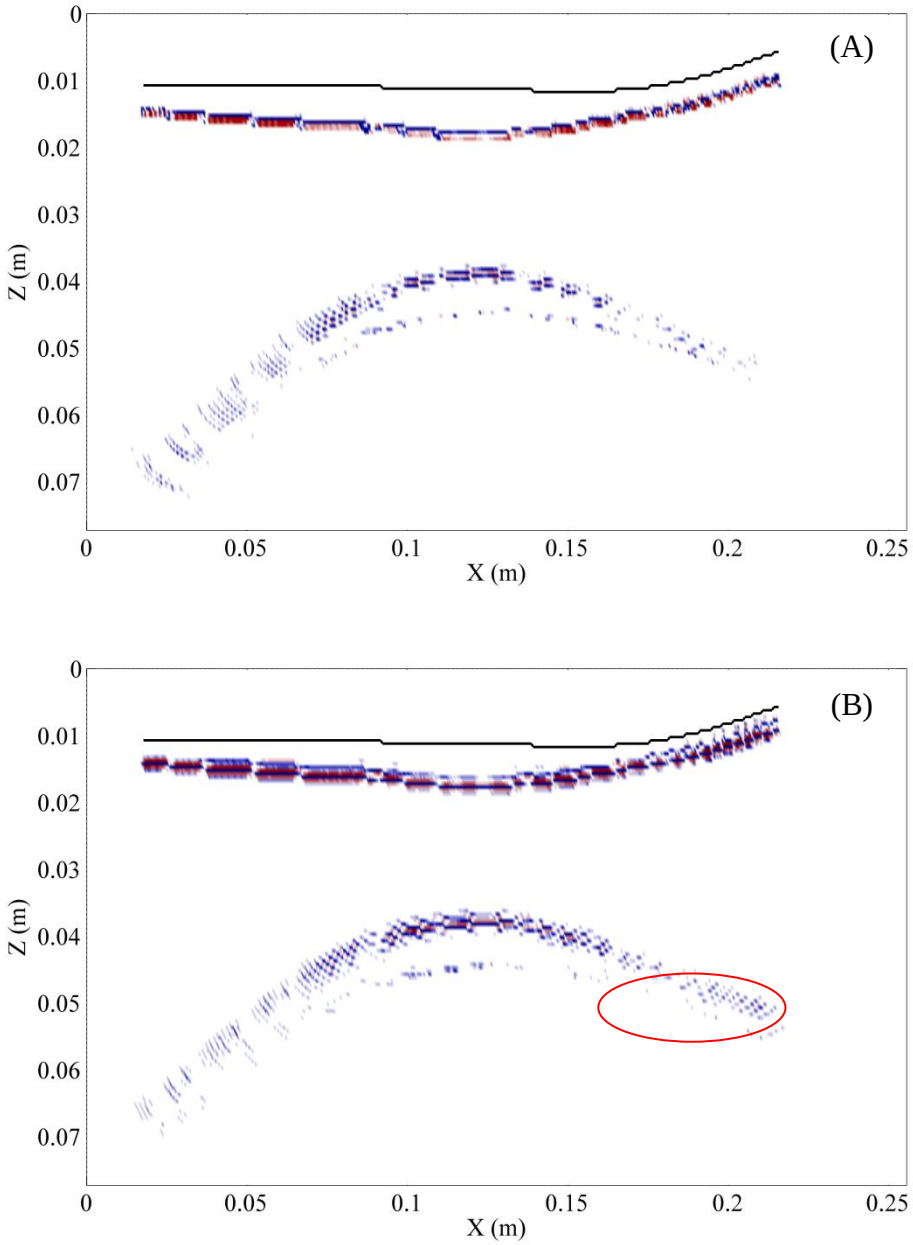

Figure 4.16 The reconstructed images when applying the different temporal sampling interval: (A) Δt = 0.40 μs; (B) Δt = 0.81 μs, while the red circle indicates the missing information comparing to (A).

4.3.2.2 Pixel dimension of the image matrix

Prior to the inversion, the size of an initial image matrix must be determined. The compromise should be considered among imaging quality, imaging resolution, and computation cost. The pixel size Δx and Δz influence imaging resolution directly. Intuitively, the smaller pixel size indicates a better resolution for the reconstructed images; yet simultaneously implies more unknowns during inversion according to Eq. (3.17); subsequently, the image quality will be reduced.

Figure 4.17 shows the inversion results for two pixel sizes: $\Delta x = \Delta z = 0.50$ mm and (B) $\Delta x = \Delta z = 0.25$ mm. Comparing the two reconstructed images, the large pixel size offers better contrast (Figure 4.17A) while the small pixel size yields sharper interfaces (Figure 4.17B). On the other hand, the computing time increases by 4 folds from 205 seconds to 846 seconds when the pixel dimension is halved.

Eq. (3.24) offers a theoretical minimum size of the image pixel when the background velocity is provided,

$$\text{mininum size of } \Delta x,\ \Delta z = \frac{\max\left[c_0(\mathbf{x})\right] \times \Delta t}{2}$$

which can be used as a guidance to determine the matrix size.

4.3.2.3 Spatial interval of acquisition

The spatial interval of acquisition determines the number of acquired records for a fixed scan length. As discussed in Chapter 3, when the pixel element is sufficiently sampled by the ultrasound rays, i.e., more ultrasound rays passing through the pixel element, the pixel value will be properly reconstructed to be

more close to the true value of the pixel. This will greatly improve the image quality.

Figure 4.18 shows the inversion results for different acquisition spatial interval or different number of signal records. Figure 4.18A and C are the reconstructed images using 100 and 199 original signal records respectively. For Figure 4.18B and D, the F-X interpolation method (Spitz, 1991; Naghizadeh and Sacchi, 2009) was used to increase the number of records from 100 to 199 (Figure 4.18B) and from 199 to 397 (Figure 4.18D).

When 100 signal records are used (Figure 4.18A), the reconstructed cortical/marrow interface appears to be discontinuous and the image has low contrast. When the acquisition spatial interval is halved by interpolation, the discontinuity of the interface is less noticeable. However the reconstructed noise is not notably reduced (see circled area in Figure 4.18B). When 199 original signal records are used (Figure 4.18C), the noise level of the reconstructed image is reduced but the overall image quality is not much different from the interpolated section (see Figure 4.18B). The 199 records were further interpolated to double the number of records and reduce spatial interval to 0.5 mm. Figure 4.18D shows the reconstructed image with 397 records. The image shows better contrast and continuity of the interfaces.

Even though more signal records provide better image quality, a compromise should be reached among accuracy, image quality, and computational cost. The interpolation method cannot be unlimitedly applied; it is shown that the unexpected artifacts are introduced to the signal data after being interpolated more than once.

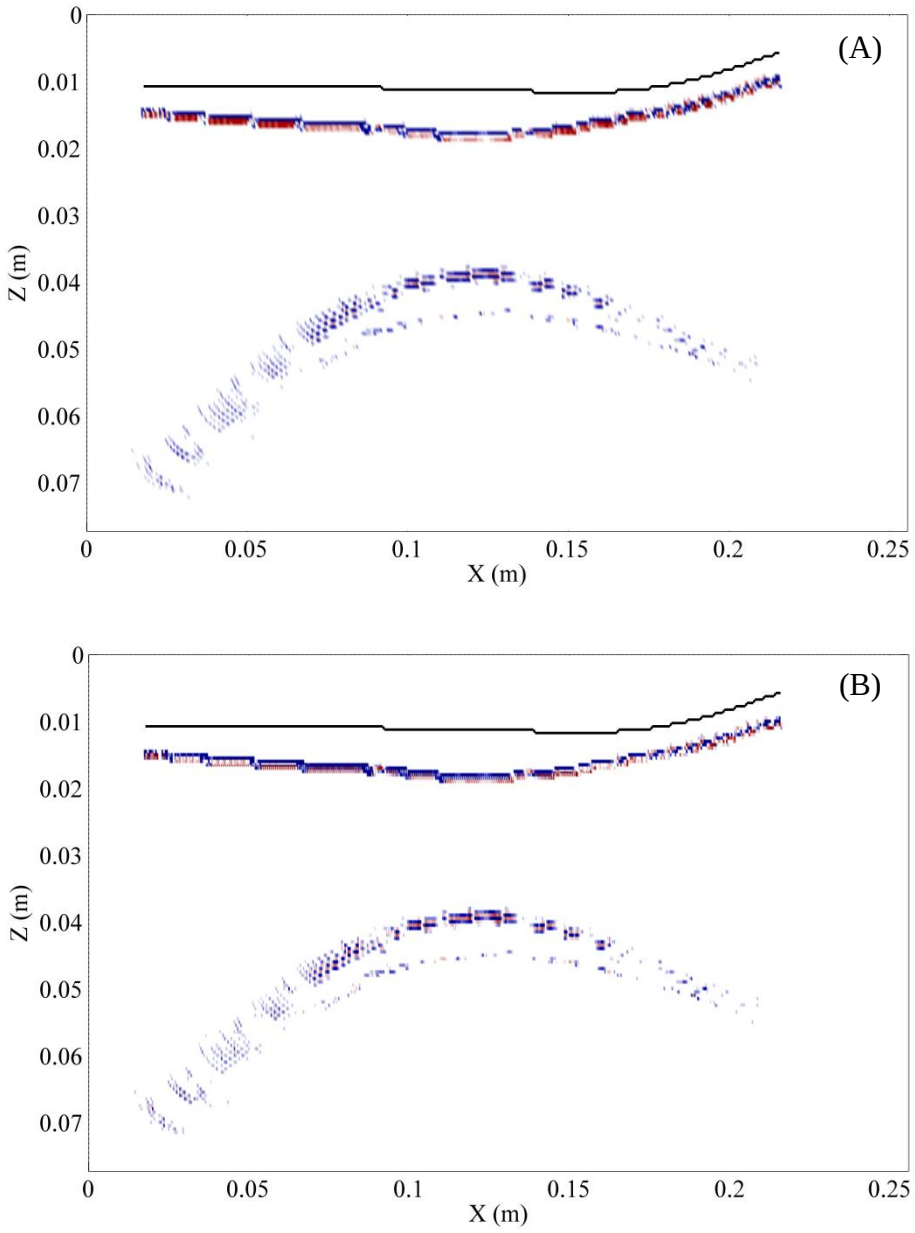

Figure 4.17 The reconstructed images when applying the different pixel size: (A) $\Delta x = \Delta z = 0.50$ mm; (B) $\Delta x = \Delta z = 0.25$ mm.

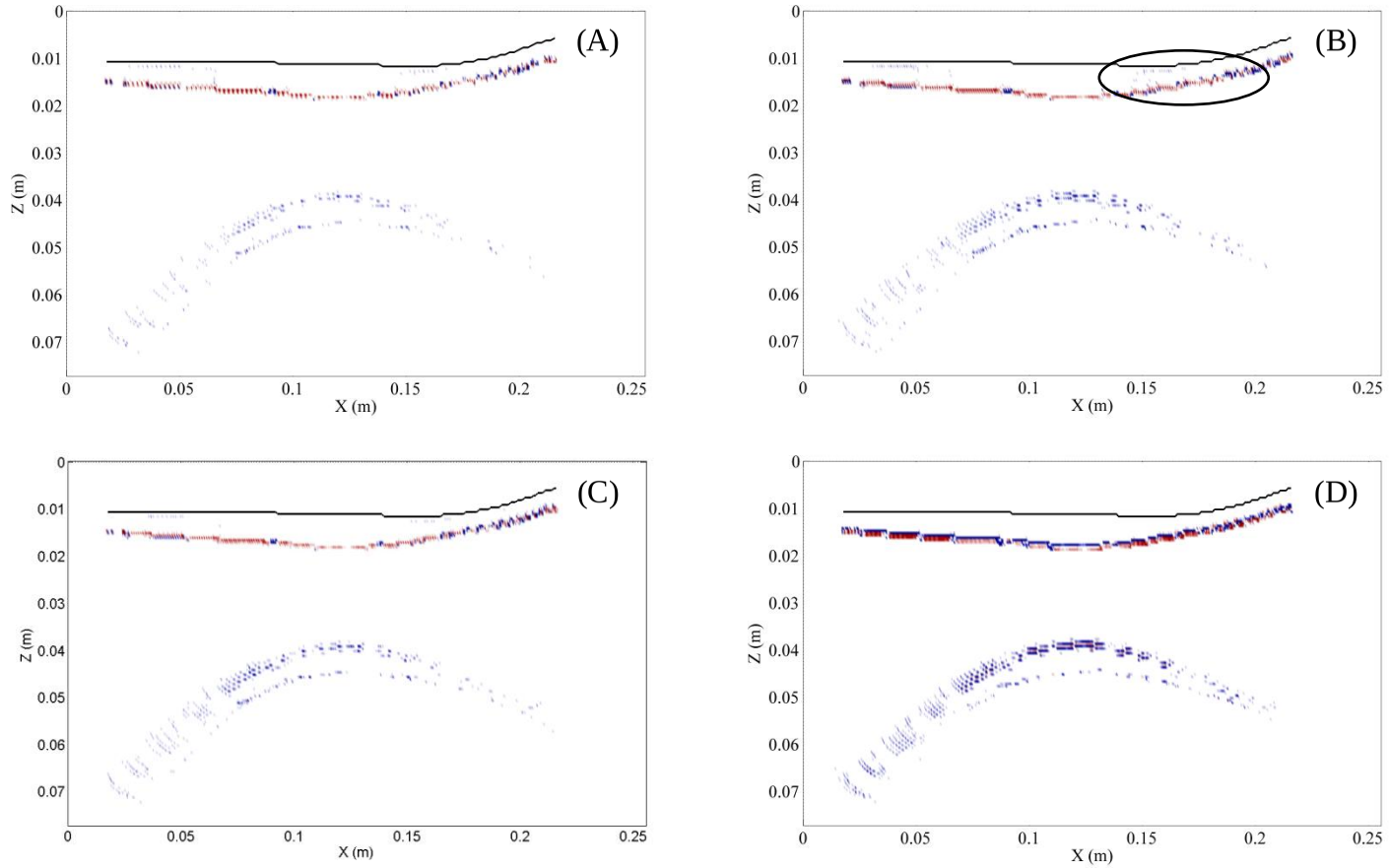

Figure 4.18 The reconstructed results for different acquisition spatial intervals: (A) 100 records (2 mm), (B) 199 records (1 mm after interpolation) while the dark circle indicates the unwanted noise comparing to (C), (C) 199 records (1 mm) and (D) 397 records (0.5 mm after interpolation).

4.3.2.4 Inversion regularizations

In this section, four different inversion algorithms as described in Chapter 3, will be examined. There are four typical methods: adjoint operator, unconstrained least squares solution (ULS), damped least squares solution (DLS), and weighted least squares solution (WLS). Based on the previous study of the trade-off curves, 10 iterations were chosen for the CG method (see Figure 4.4B); the values of the regularization parameters were 4 and 0.1 for DLS and WLS methods respectively.

Figure 4.19 shows the reconstructed images using different inversion algorithms. Among the methods, the adjoint operator yields the least favorable result. The images are blurred and the reconstructed interfaces are fuzzy with low contrast (Figure 4.19A). Relatively, the ULS method improves the accuracy of interfaces (Figure 4.19B). Since the method contains only the misfit term in the cost function without the consideration of model smoothness, the reconstructed image is very noisy; both left and right ends of the first interface cannot be completely reconstructed due to great amount of interferences resulted from the low signal-to-noise ratio of the time records. For the WLS method, the two first-derivative operators were considered. We recall the derivative operator given by Eq. (3.20)

$$\mathbf{D}_f = \begin{pmatrix} c & a & c \\ a & b & a \\ c & a & c \end{pmatrix}.$$

Various operators can be constructed by assigning different values to the matrix elements, (a, b, c), for example (-1, 4, 0) and (-1, 8, -1). The latter is shown to yield better reconstructed results (Figure 4.19C). Theoretically the derivative

operator should emphasize the edge information during the inversion procedure. Comparing the other three reconstructed images, the WLS method provides the sharpest reconstructed interfaces with better contrast especially for the first cortex/marrow interface (see Figure 4.19C). However, the discontinuities, indicated by the dark arrows in the figure, are also enhanced with edge artifacts. Among all the reconstructed images, the DLS method provides the most reasonable results with clearer interfaces, better contrast, less noise, and smoother images (Figure 4.19D), striking a balance between image smoothness and accuracy.

4.4 Inversion IV: Optimal reconstruction

In this inversion example, the optimal values of those parameters examined in the previous sections were used to invert the FD data set. These values are

frequency range: 0.5-3 MHz

frequency sampling rate: 89/MHz

aperture: $\pm 5^{\circ}$

source wavelet: experimental

bandpass filter: 0.5/0.7/2.5/3.0 MHz

temporal sampling interval (Nyquist): 0.04 μs (12.5 MHz)

pixel size: 0.5 mm

spatial interval of acquisition: 0.5 mm

inversion method: DLS with $\mu = 4$ and 10 iterations.

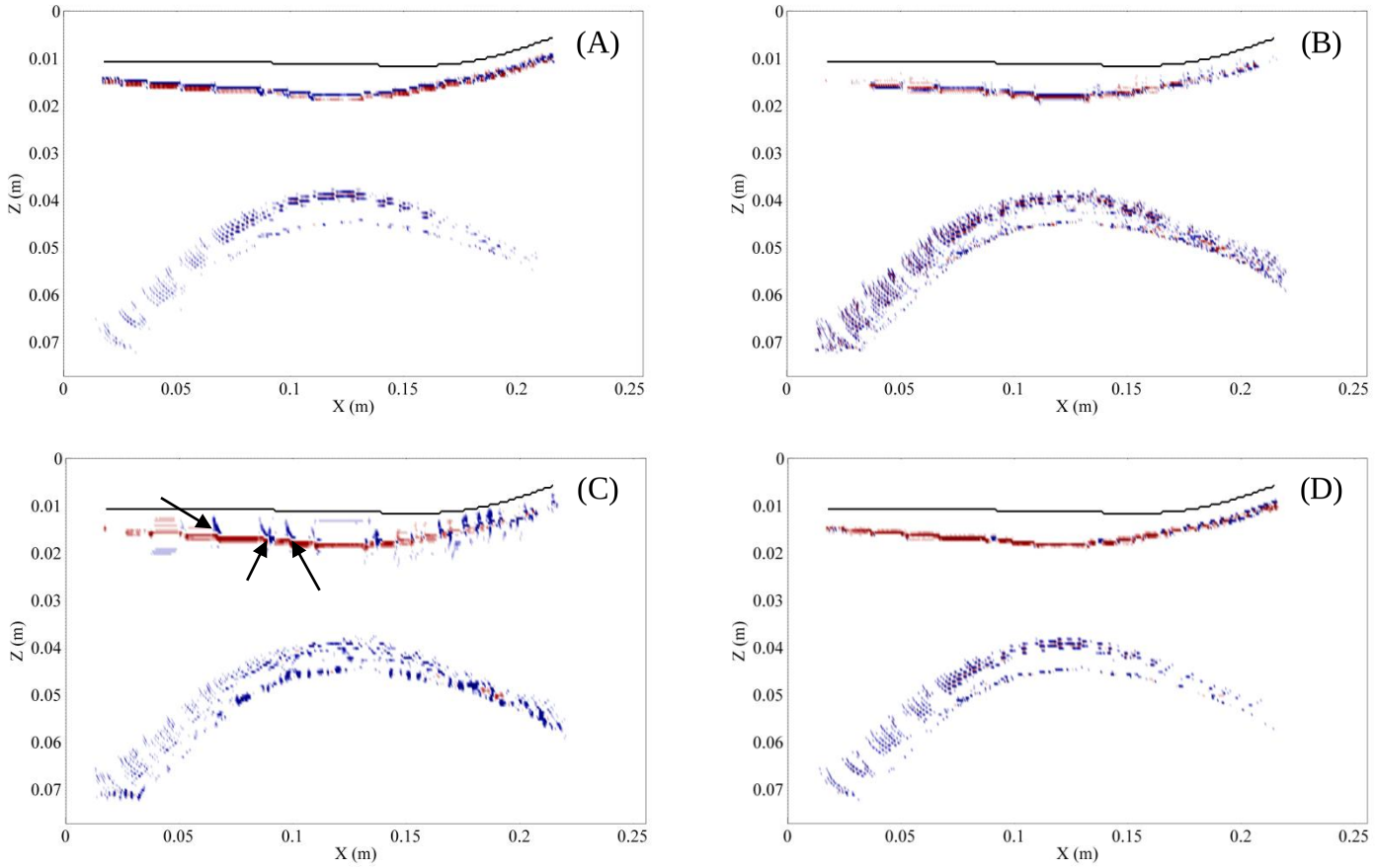

Figure 4.19 The reconstructed images for different inversion algorithms: (A) adjoint method, (B) ULS method, (C) WLS method (μ=0.1) where the arrows indicate the enhanced discontinuities comparing to (D), and (D) DLS method (μ=4). Ten iterations were used for (B) – (D).

Figure 4.20A shows the reconstructed image. Three major interfaces are identified: cortex/marrow, marrow/cortex and cortex/air. Due to the small $5°$ aperture used, only the area directly below transducer can be reconstructed, therefore the reconstructed interfaces are shorter at both ends than those of the original bone model. Very similar to the previous results, the first cortex/marrow interface is denser, sharper, more continuous and smooth, much better resolved than the other two interfaces. For the lower interfaces, the middle part of the bone is better reconstructed than both ends. As discussed in Section 4.1.2, this discrepancy between the reconstructed image and original model is slightly attributed to the small amplitudes due to spherical divergence, structural inhomogeneities, and beam refraction from large curvatures. Another important reason for the low signal-to-noise ratio is the pulse dispersion due to material absorption. The absorptive mechanism not only attenuates the signal amplitudes, but also makes the signal pulses broader and dispersive, which results in ringing waveforms of several cycles and leads to less sharp reconstructed interfaces.

As the interfaces are assumed to be continuous and smooth, a seven-order polynomial was used to best-fit the reconstructed interfaces in the regions where the reconstructed images can be seen and are mainly located between 0.05 m and 0.2 m. The best-fitted interface curves are superimposed on the reconstructed image (see Figure 4.20A) and the original bone model (see Figure 4.20B). The first cortex/marrow interface is perfectly located and identified. For the other two interfaces, there is visible discrepancy between the reconstructed and the original interfaces. The middle parts of the interfaces are better reconstructed than the ends.

There are two main reasons for this discrepancy. First, the discrepancy partly arises from the replacement of a true velocity profile by its smooth version

for ray tracing. As discussed in Section 2.4 of Chapter 2, the ray tracing algorithm requires a small velocity gradient to calculate the travelled distance and travelling times properly. Smoothing a velocity model will introduce small inaccuracy or error to the calculated quantities when the travelled path is small. However, the error will accumulate when the travelled distances are longer, especially for the deeper structures. Therefore the lower interfaces are not imaged or mapped accurately. Secondly, we have replaced an inhomogeneous bone by a three homogeneously-layered bone model. The inhomogeneity of the real bone samples due to existence of cancellous bone will also influence the accurate reconstruction of the lower marrow/cortex and cortex/air interfaces.

However, the reconstruction of upper cortical layer should not be seriously affected as long as the cortical velocity is accurately determined. The determination of the velocity and the reconstruction of the cortex using real animal bone samples will be the subject of Chapter 5, which leads to a feasible and robust method to assess the thickness of cortical layer.

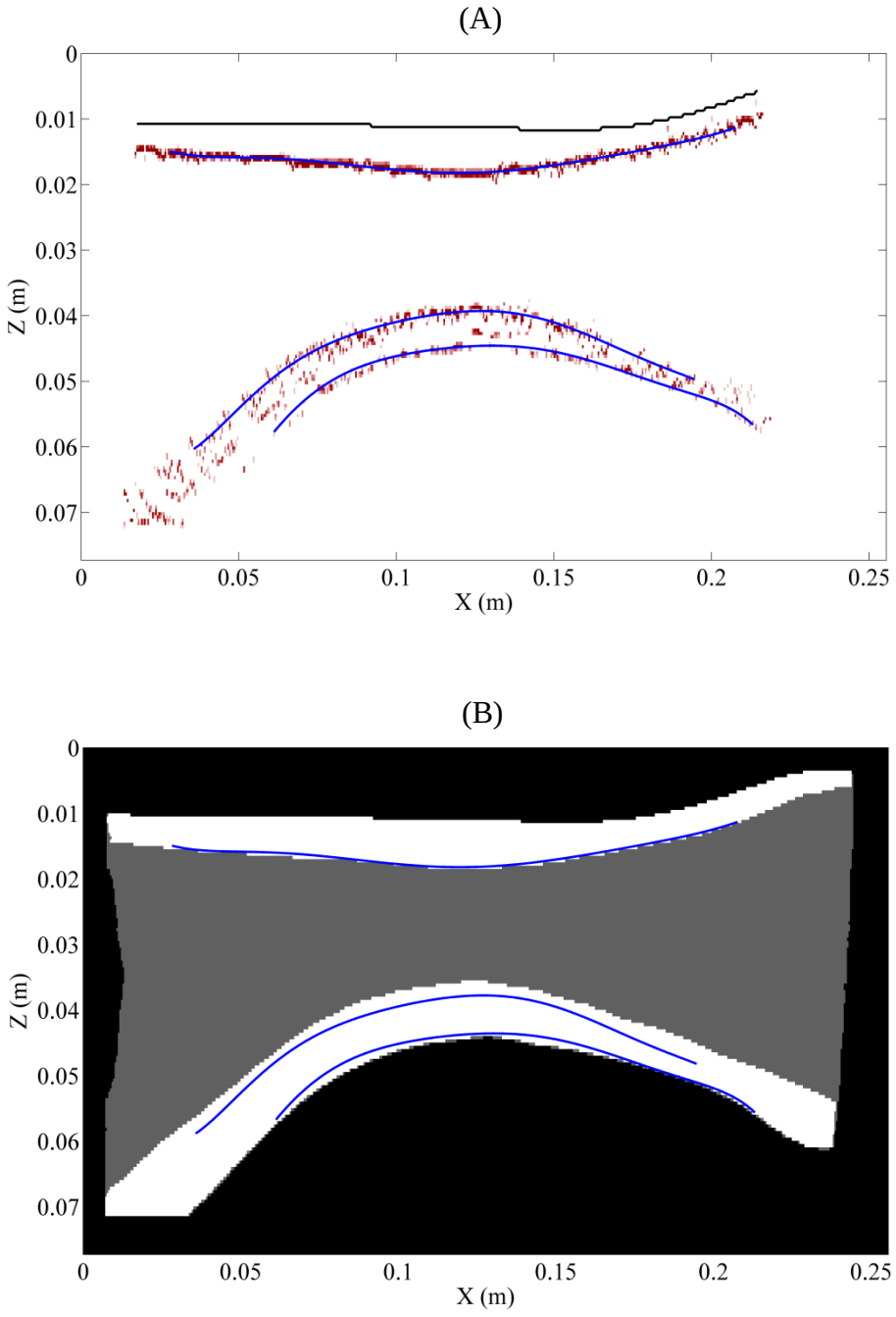

Figure 4.20 The reconstructed images for the FD data using the optimal inversion parameters: (A) the reconstructed image superimposed by the best-fitted curves for the interfaces; (B) the original bone model (Figure 4.6) superimposed by the interface curves

Chapter 5

In vitro application to real bone data

Different from the simulated data, imaging real bone data is more challenging as the data is noisier and less predictable due to many factors, notably, electronic noises from acquisition and heterogeneities of bone tissues. In this chapter, we image real bone sample *in vitro*. I start this chapter with a discussion on sample preparation and experimental setup for zero-offset measurements. As a digression, I then describe the offset axial transmission method to estimate cortical velocity, which is an important input parameter for the imaging algorithms. The inversion of three bone samples is presented using the estimated velocities and the accuracy of the recovered thickness of the first cortical layer is assessed based on the CT images. Finally, a full inversion for all interfaces is performed for a real bone data set.

5.1 Materials and methods

To assure that all the signal records only register the information caused by the internal structure, the experimental conditions，such as equipment setup, acquisition protocol design, and data analysis after acquisition should be as identical as possible when collecting and processing the data. Therefore, one set of equipment was specially designed.

5.1.1 Preparation of bone samples

Four fresh long bone samples were prepared: two from bovine tibia (labeled as Sample 1 and 4), one from cervine tibia (Sample 2), and one from ovine femur (Sample 3). The samples were cleaned and the soft tissue was removed. Most of proximal epiphyses were removed and the samples were cut to 200-250 mm long except the ovine sample, which was kept for full length.

The samples were scanned by a multislice CT scanner (Siemens Somaton 64) and 1-mm thick sagittal images were reconstructed using high resolution. The dimension of the image matrix is approximately 500×1400 with 0.18 mm pixel size. Except for Sample 4, the pixel size is much bigger at 0.5 mm. The CT image of Sample 4 was previously used in Chapter 4 to construct the bone velocity model. Based on the CT images, the minimum diameters of the samples, which were measured at the mid-shaft, range from 19.4 mm to 33.5 mm with mean cortical thickness of top cortex from 3 to 7 mm. Table 5.1 lists the geometrical properties of the bone samples and some information relevant to the data acquisition. Since the receiver was translated in the mid-line of the coronal plane along the long axis during the experiment, the sagittal images with the largest cross-section area of the bone samples will be used to compare with the inversion results.

The samples were stored in a freezer before the experiments. To achieve the best reconstructed images and comparison, one day before the CT-scanning, the samples were defrosted overnight at room temperature of 20^{o}C, cleaned to remove the soft tissue, and then preserved in a 70% alcohol. The ultrasound data were acquired right after CT-scanning to avoid any change of internal structure and material properties due to the preservation process. However, during preservation, the marrow in the samples shrank and therefore some cavities were formed in the

structure; the properties of cortical bone changed because of dehydration, which would result in decreased velocity and increased attenuation in the bone tissue because of the intruded air.

5.1.2 Experimental setup

Figure 2.2 shows a specially designed device for data collection. The bone samples sat firmly on the brackets of the two wheels, which were fixed by tightening the knobs at the end. A Panametrics CHC706 dual-head P-wave composite transducer (Panametrics, Waltham, MA) with center frequency of 2.25 MHz was used to transmit and receive the signal using the transmission mode (Figure 5.1A). Two piezoelectric crystal elements are housed in the same case acting as transmitter and receiver separately. The source signal was previously shown in Figure 4.7. Figure 5.1B illustrates the function of the transducer. The diameter of the active surface is 0.5 inch (13 mm). Figure 5.1C shows the measured beam radiation pattern indicating the beam strength is mainly focused within $\pm 20^\circ$ aperture.

Figure 2.2 shows the schematic of the experimental setup. The transducer was directly positioned on the bone surface coupling with the ultrasound gel at room temperature of 20^oC. A steel bar was placed on top of the transducer to provide constant pressure between the transducer and the sample. A Panametrics 5800 computer controlled Pulser/Receiver (Panametrics, Waltham, MA) was used to pulse the transducer and a LeCroy wavesurfer 422 oscilloscope (LeCroy, Chestnut Ridge, NY) was used to receive and store the time signals. Time signals were collected along the axial direction of long bone samples with step interval of 1 mm. Each signal was averaged 128 times in real time.

Table 5.1 The dimensions of the bone samples and data acquisition parameters.

Sample no.	Bone type	Length (mm)	Minimum diameter* (mm)	Image size ($nz \times nx$)	Pixel size (Δx or Δz) (mm)	Closest offset (mm)	Number of records acquired	Spacing interval (mm)	Note
1	Bovine Tibia	257.9	30.5	512 × 1497	0.18	30.4	211	1.0	Figure 5.6A
2	Cervine Tibia	227.3	19.4	450 × 1418	0.18	50.9	163	1.0	Figure 5.7A
3	Ovine femur	207.0	21.7	512 × 1339	0.18	60.0	122	1.0	Figure 5.8A
4	Bovine Tibia	236.3	33.5	155 × 512	0.50	17.7	198	1.0	Figure 4.6A and 5.10A

*The diameters were measured at the mid-shaft of the bone samples.

(A)

(B)

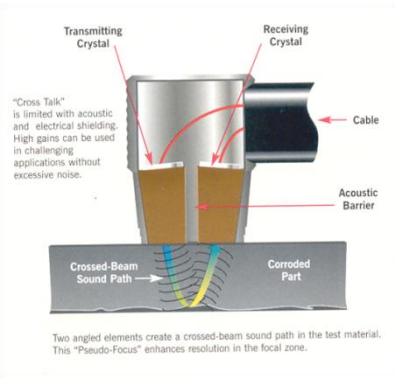

(C)

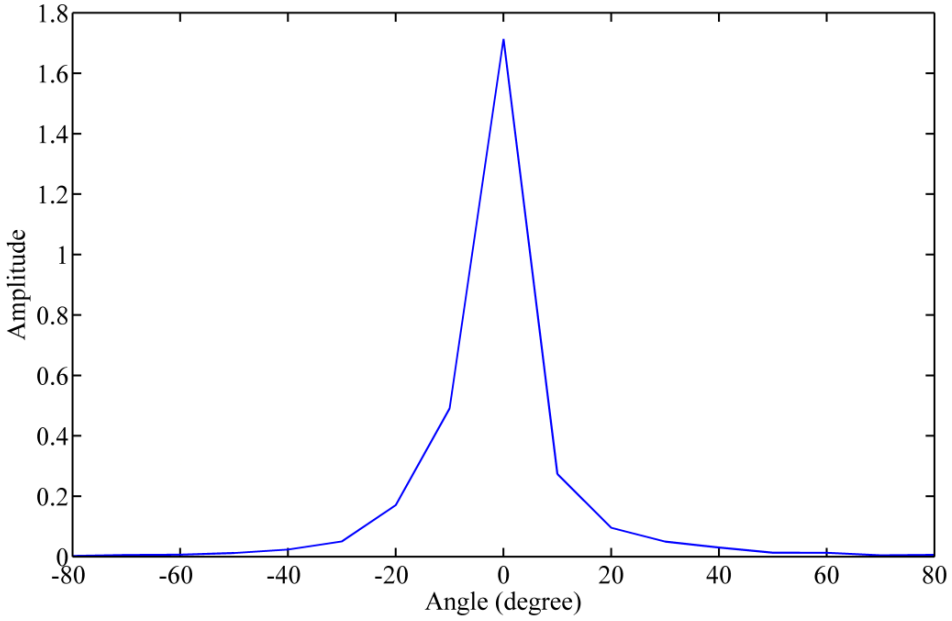

Figure 5.1 The experimental transducer: (A) a CHC706 dual-head P-wave composite transducer; (B) a schematic showing how a dual-head transducer works (Ultrasonic transducers catalog, P6, Panametrics INC, Waltham, MA); (C) the experimental beam radiation pattern. The angle refers to angle of the beam with respect to normal direction to the transducer's active surface.

The pulse/echo mode is usually an easier way to acquire zero-offset data. However, the trigger signals from the transducers operating in the pulse/echo mode can last for more than 4 μs. Then, the echoes from the first interface of the bone samples will be partly covered by the trigger signals and not be easily identified especially when the cortex is thin. In this situation, the dual-head transducer operating in the transmission mode is better suited for the study because it provides shorter trigger signals. The trigger signal of the CHC706 dual-head transducer is less than 1.2 μs. There is a layer of shielding material to protect the crystals, which leads to a measured delay time of 4.94 μs in the receiving signals. The short trigger signal and the delay time will ease the separation of the signals from the trigger signals. However, the delay times must be subtracted from the recording times of the signals for the correct travelling times. During the experiments, acquisition parameters will be held unchanged for each bone sample. The collected signals will be saved and processed further by a desktop PC.

5.2 Estimation of cortical velocity

A good estimate of the background velocity is a crucial step for image reconstruction. In this chapter, we mainly focus on imaging the top cortex. I describe in the following a procedure to estimate the velocity of the cortex using the axial transmission offset data.

5.2.1 Experimental setup

Figure 5.2 shows the experimental setup for the axial transmission technique involving two transducers. Two *P*-wave angle beam transducers (Panametrics V539, Waltham, MA) were matched with two angle wedges (Panametrics

ABWM-7T, Waltham, MA). The transducers have a center frequency of 1.0 MHz with an active 13-cm diameter element. One transducer-wedge system, acting as a transmitter, was fixed and the other set was moved rectilinearly along the long axis of the bone samples at a regular spacing of 1 mm.

Five different angle wedges including 30 °, 45 °, 60 °, 70 °, and 90 ° were used to generate ultrasound at different incident angles. According to the product information (Olympus, Waltham, MA), the wedge angle refers to the refracted shear wave angle in steel measured at 5 MHz (Ultrasonic transducers catalog, P8, Panametrics INC, Waltham, MA). Since the shear wave velocity of steel is 3240 m/s and the cortical velocities of our samples are around 3200 m/s, the wedge angle can approximate the refracted *P*-wave angle in the cortex. For convenience, we use the wedge angle, hereafter, to refer to the refracted *P*-wave within the cortex.

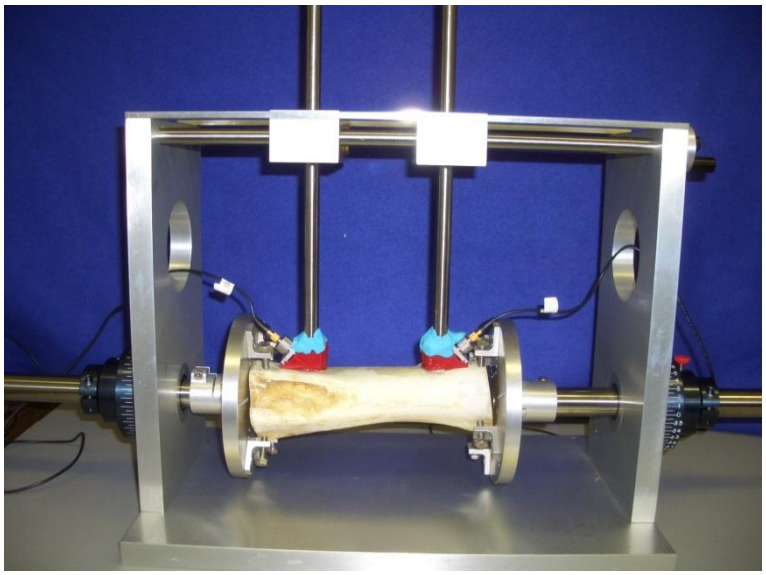

Figure 5.2 The setup for an offset axial transmission experiment.

Ultrasound waves propagate much longer distance within the cortical layer in the offset case than in the zero-offset case and will experience greater attenuation and dispersion. Lower signal-to-noise ratio is expected in the signals. The transducers with lower center frequency should be employed to reduce the effect of attenuation and dispersion. We chose to use 1.0 MHz instead of 2.25 MHz to measure the cortical velocity of bone samples. Born theory does not consider dispersion during the approximation, so the inversion results will not be influenced even if the predicted background velocities are estimated using lower frequency.

Three samples: bovine (Sample 1), cervine (Sample 2), and ovine (Sample 3) were used to estimate cortical velocities of the samples. Depending on the contact surface condition of the samples, the placement of the source-receiver pair and the minimum separation between transducers (or closest offset) varied. The closest offsets for the samples are listed in Table 5.1. For each bone sample, four angle wedges were used, yielding four sets of data. There are more than 50 signal records for each set.

5.2.2 Data analysis

For short offset, the first arriving signal (FAS) is the direct wave travelling from the source to the receiver through the cortical layer. The velocity, *V*, of the FAS can be estimated by

$$V = \frac{X}{t} \tag{5.1}$$

where *X* is the offset and *t* is the travelling time of the FAS. The distance *X* of the *n*'th record can be calculated by knowing the closest offset and the spacing

interval, which is 1 mm in our study:

$$X = \text{closest offset} + (n-1) \times \text{spacing interval}\ .$$

The arriving time t can be estimated by the time of the first peak of the signal. Instead of using a single record, a group of 10 – 20 records and linear least squares regression was used to determine the best-fitted line. The estimated velocity is then given by the 1/slope of the regression line.

As a comparison, a zero-offset based method, similar to the method described in Section 4.2.1, was used to estimate cortical velocity. The thickness of the top cortical layer was provided by the CT images and the travelling times were given by the one-way travelling time of the corresponding echoes. A group of at least 100 records was used and the velocities thus obtained were averaged. Table 5.2 lists the means of the CT-based velocity, which were used as standards or exact values to evaluate the FAS-based velocities.

5.2.3 Results and discussions

Table 5.2 lists the results of estimating cortical velocities for the twelve data sets. Four different wedge angles including $30°$, $45°$, $60°$ and $70°$/$90°$ were used for each bone sample. Since the results for the wedge angles $70°$ and $90°$ do not show significant difference, either one was used for each bone sample. Figure 5.3 shows one group of signals acquired from ovine sample for four different wedge angles. In the cases of $30°$ (Figure 5.3A) and $45°$ (Figure 5.3B), the amplitudes of the FAS travelling directly from source to receiver are smaller than the amplitudes of the late-arriving waves, which are indicated by the red dotted line in Figure 5.3B. Especially for $30°$, the FAS and the late-arriving waves interfere each other, making their identification difficult. This is mainly caused by

beam pattern of the transducer, which leads to less energy propagating along the axial direction when the wedge angle is small. The smaller amplitude will result in lower signal-to-noise ratio, affecting the accuracy of picking the travelling times of the FAS' peaks. With the increase of wedge angle, the beam is tilted more toward the axial direction and the FAS energy become stronger, as shown in the dash line in Figure 5.3C. However, due to the curved surfaces of the bone samples and the bigger contact surfaces of the wedges, good coupling was not possible during the experiments for large wedge angles, 70° and 90°, so the amplitudes of the FAS drop rapidly and the pulses become wider, which is a sign of energy loss and signal dispersion.

Comparing the estimated SOS value of the cortical tissue in Table 5.2, the 60° wedge has the best estimated velocities of the three samples, which are 3163 m/s, 3106 m/s and 3149m/s; and the least errors are 1.4%, 5.0%, and 3.6% respectively. For 30° wedge, the errors relative to standard value are more than 50% in some cases. Comparatively, the 45° and 70°/90° wedges on the average has an error around 30-50% smaller than the error of 30° wedge but still greater than the error of 60° wedge.

Table 5.2 Estimation of cortical velocities by linear regression.

Bone sample	Wedge Angles (°)	Closest offset (mm)	CT-Based Velocity (m/s)	Number of Records Used					
				10		15		20	
				Estimated Velocity (m/s)	Absolute Relative Error* (%)	Estimated Velocity (m/s)	Absolute Relative Error (%)	Estimated Velocity (m/s)	Absolute Relative Error (%)
Bovine (Sample 1)	30, 45, 70	42.5, 34.2, 24.2	3120	4955 - 9894	59 - 217	2470 - 4809	21 - 54	2331 - 5319	17 - 71
	60	34.4		3389	8.6	**3163**	**1.4**	3659	17
Cervine (Sample 2)	30, 45, 90	38.8, 29.4, 13.7	3270	3103 - 5178	11 - 37	2829 - 4117	9.0 - 26	3103 - 5178	5.1 - 58
	60	39.4		2204	33	**3106**	**5.0**	4378	34
Ovine (Sample 3)	30, 45, 90	35.7, 29.5, 12.5	3039	1193 - 7985	15 - 163	3763 - 8152	24 - 168	4607 - 8436	52 - 178
	60	27.2		**3149**	**3.6**	4068	34	4436	46

* The absolute relative error is calculated by dividing the absolute difference between the estimated and CT-based velocities by CT-based velocity.

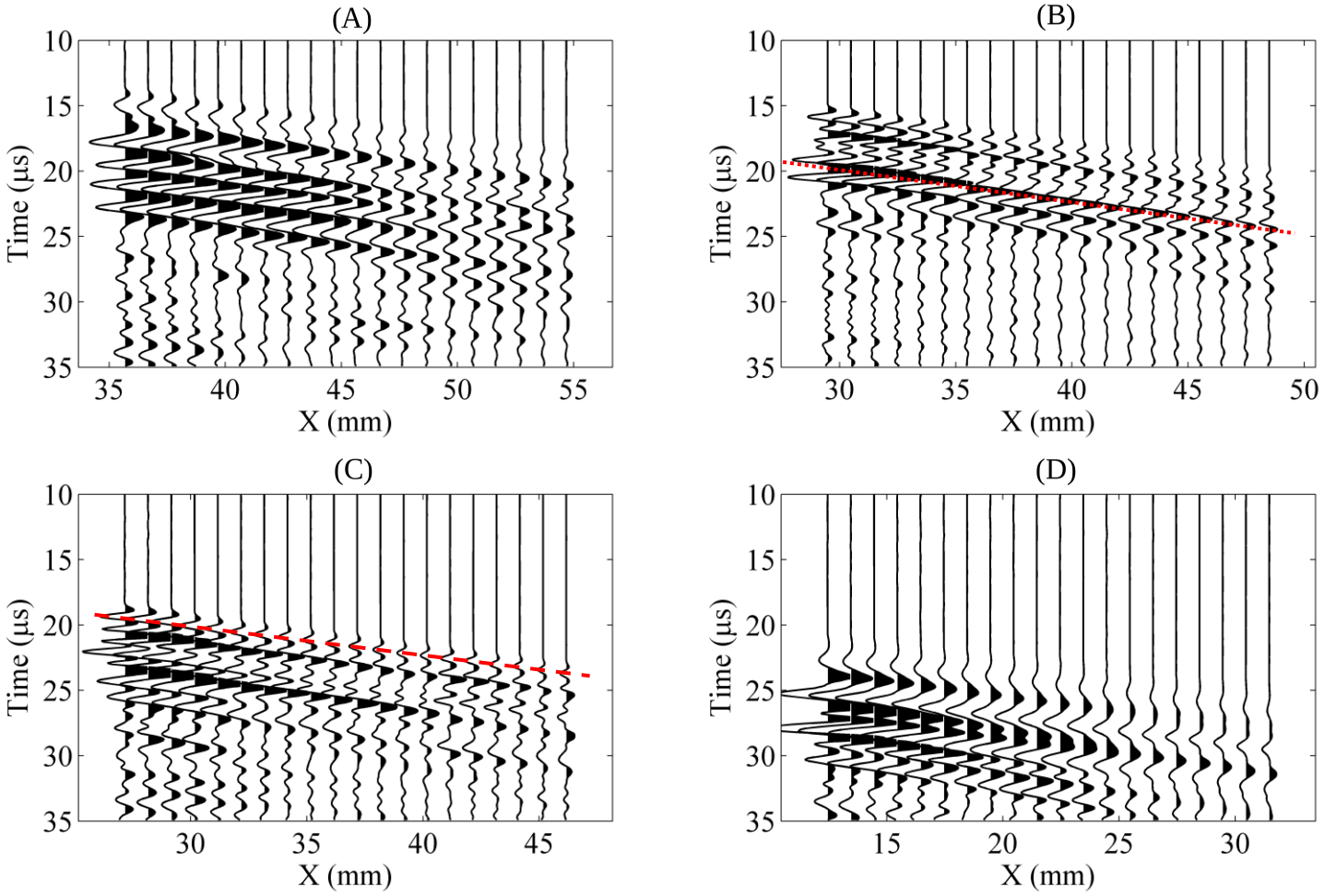

Figure 5.3 The (*x* - *t*) echograms of the ovine sample for four different wedge angles: (A) 30 °, (B) 45 ° (the dotted line indicates the late-arriving waves), (C) 60 ° (the dash line indicates the FAS), and (D) 90 °.

To apply the linear regression method for cortical velocity, a group of the first ten, fifteen and twenty records were used to evaluate the accuracy of the estimation. Even though more than 50 records were collected during the experiment, the FAS can only be observed in the records close to the source with amplitudes decreasing at further offset. Among the number of records used, the group of 15 records works well for the bovine and cervine samples and have smaller errors as compared to the CT-based velocities. The results derived from the first 10 records are less favorable due to perhaps inadequate data points. For the ovine sample, the group of 10 records suggests a more accurate estimation instead. The sample is shorter than the other two samples and more uniform in the mid-shaft, thus fewer records providing better estimation. In case of 20 records, the signals were more interfered by the noise, attenuation due to longer travelling distances, the late arriving waves and surface waves, therefore larger errors in estimation were incurred.

Additionally, the structural characteristics of cortical bone layer are an important factor for the velocity assessment. Figure 5.6A, 5.7A, 5.8A show the CT images for bovine, cervine, and ovine samples respectively. Apparently, the cortical thickness of bovine sample is less uniform along the axial direction and ovine sample shows a slight curvature of the contact surface with the transducers. Comparing the results of SOS estimation listed in Table 5.2, cervine sample presents a more stable and accurate results than the other two bone samples for all wedge angles and number of records. The possible reason is that different from other samples, the cervine sample has a flatter top surface and the cortical layer is more homogeneous and uniformly thick. In this situation, the scattering due to irregular cortex/marrow interface and inhomogeneity is reduced and the FAS will be less influenced by the other signal arrivals.

In summary, the velocity estimation using offset data are more accurate and stable when the wedge angle is 60°. The number of applied experimental records should be selected according to surface condition and length of the samples. Ten to fifteen records are reasonable choice for the assessment. If the curvature of the contact surface is larger, smaller number of records should be used to ensure the transducers to be level during the experiments. Since the structural properties can greatly affect the results, the mid-shaft of long bones, which usually has little presence of cancellous bone, should be considered for the cortical velocity estimation.

5.3 Cortical thickness assessment

In this section, I image the top cortices of the three bone samples and measure their thickness using the reconstructed images. The previously estimated cortex velocity is used for the initial velocity model. Experiments describing data acquisition for zero-offset cases was already presented in Section 5.1.2. Table 5.1 provides information about the closest offset, spatial interval between records, and the total number of records acquired for each sample.

5.3.1 Data analysis and processing

The experimental data requires some data processing prior to inversion. First, the trigger signals were removed from each record; the delay time, intrinsic to the transducer, was deducted from the signal; decimation up to 100 folds was applied to reduce the total number of data samples, decreasing the sampling rate to 20 MHz, i.e. Δt = 0.05 μs with a 10 MHz Nyquist frequency. Trapezoidal bandpass filter with different frequency bands were applied to the data: 0.2/0.5/2.5/3.0 MHz for bovine sample, 0.2/0.7/2.5/3.5 MHz for cervine sample,

and 0.2/0.7/2.5/3.0 MHz for ovine sample respectively. Each record was then normalized by its own maximum amplitude.

Since the top cortical layer was the imaging target, inversion with a constant velocity model was appropriate. Also, only the reflection signals from the cortical/marrow interface were required to invert for the top cortex. A 61-point Hamming window was used to single out the cortex/marrow reflections while eliminating the other signals. Figure 5.4A shows an acquired ultrasound record including all reflections from the interfaces and Figure 5.4B shows the filtered signal containing only the top cortex/marrow reflection.

The internal structure of a bone sample is a continuous medium and the acquired signals are actually the integral responses of reflecting zones instead of single points; unless there is a bone fracture, any large sudden change between neighboring records might not be real. However in experiments, there exist some discontinuities in the records due mainly to equipment-related factors. For example, equipment response may be different when the range of vertical display of the oscilloscope is changed, causing a discontinuity to the records. Figure 5.4C shows a group of original records of the cervine bone sample with some lateral discontinuities (see circled areas) for the cortex/marrow reflections. Here, the records were visually inspected for discontinuities and then replaced by the new records interpolated by the closest two or four records. In case the discontinuity of the data cannot be completely eliminated by the interpolation process, then we will accept the processed data without further manipulation. At the end, the records were interpolated to have the number of records doubled, i.e., 421, 325, and 243 records for the bovine, cervine and ovine samples respectively. Figure 5.4D shows the records from the cervine sample after Hamming-filtering and interpolation.

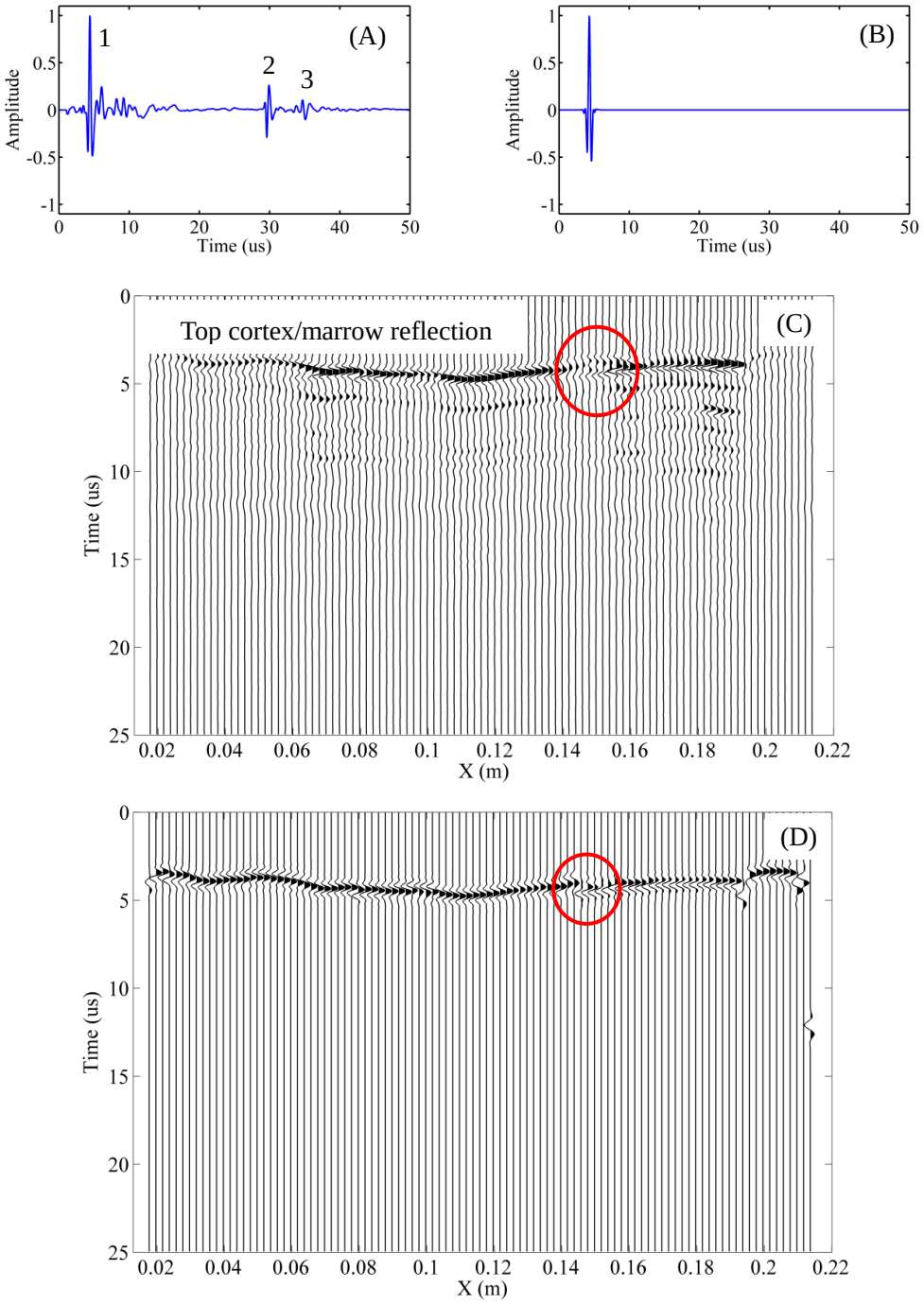

Figure 5.4 Ultrasound signals of the cervine sample (Sample 2): (A) an original time signal including the top cortical/marrow interface (1), the marrow/cortical interface (2), and the cortical/air interface (3); (B) the filtered signal including the top cortex/marrow echo only; (C) an original ultrasound section; (D) a filtered and interpolated ultrasound section with the cortex/marrow reflection only. The red circles in both (C) and (D) indicate the lateral discontinuous area before and after interpolation.

5.3.2 Inversion parameters

Prior to image reconstruction of the three bone samples, proper inversion parameters were selected based on the rationales discussed in Chapter 4. The beam aperture was settled at $\pm 5^\circ$ to decrease the influence of signal scattering and averaging. The frequency range for inversion was from 0.2 to 3.0 or 3.5 MHz depending on the bandpass frequency windows of the applied filters. The numbers of data points used per record are 1883 for the bovine sample, 873 for the cervine sample, and 887 for the ovine sample respectively. The experimental wavelet shown in Figure 4.7 was used. The size of the CT images was used as the dimension of the reconstructed images. Table 5.1 lists further information of the matrix sizes and pixel sizes for each sample.

The velocities, previously estimated from the offset axial transmission data were used to construct the constant background velocity model. For bovine, cervine and ovine samples, the SOS values were respectively 3163 m/s, 3106 m/s and 3149 m/s as listed in Table 5.2.

A damped least squares conjugate gradient (DSLCG) method was used for the inversion procedure. Ten iterations were used based on the results in Chapter 4. Figure 5.5 shows a trade-off curve for 3 iterations using the ultrasound data of the cervine sample. Based on the observation from the curve, the regularization parameter can be specified between 1 and 3. The trade-off curve for the other two data sets showed similar results. Therefore μ=1.5 was used as the regularization parameter for all three bone samples.

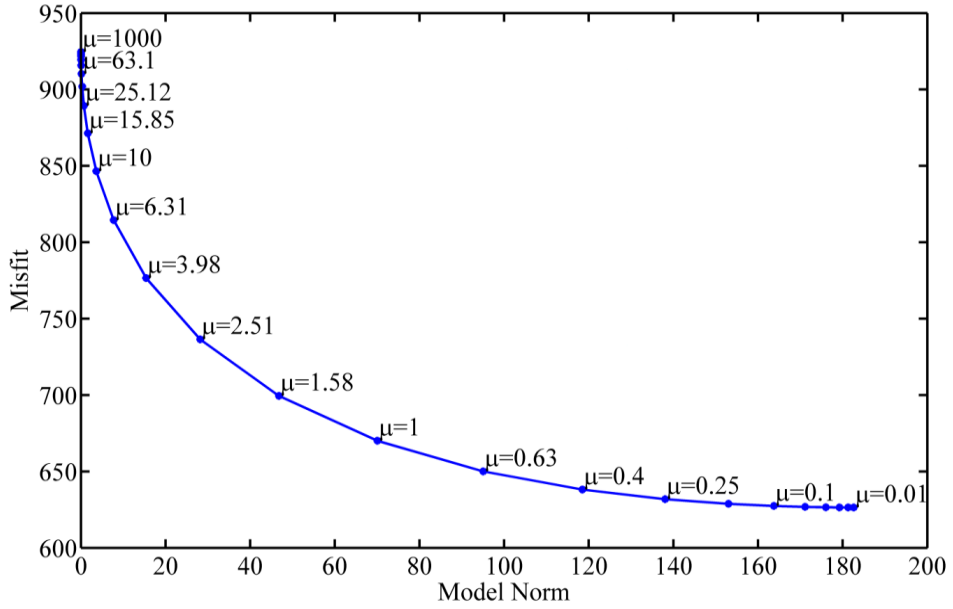

Figure 5.5 A trade-off curve for the cervine bone sample with 3 iterations.

5.3.3 Thickness estimation

The first interfaces between the cortical bone and marrow were reconstructed. Since the bone surfaces, indicated by the source/receiver positions, are known, the distance between these two interfaces is the estimated cortical thickness.

5.3.3.1 Inversion results for bone samples

Figures 5.6, 5.7 and 5.8 demonstrate the inversion results and thickness measurement for the three bone samples. In Part A of all the figures, velocity models converted from the CT images are shown and the red lines indicate the source/receiver (S/R) pair locations on the bone surfaces. Part B of all the figures

presents the reconstructed images of the samples. The black solid lines indicate the bone surfaces, which are the same red lines in part A of the figures. The red lines are the recovered interfaces between cortex and marrow. Part C of all the figures shows the cortical thickness comparison between the CT measurements and the reconstructed image, where the solid lines are the CT results and the asterisks are the ultrasound measurements. The number of thickness measurements is equal to the number of source/receiver pairs because at the S/R positions the cortical thickness was estimated.

Figures 5.6B, 5.7B, and 5.8B show the recovered cortex/marrow interface. The interfaces are segmented and not continuous, showing a few major discontinuities. The inaccuracy of the reconstruction at those break points are attributed mainly to two reasons: the reconstruction noise causing the peaks to be thresholded at different locations and the presence of the discontinuity in the data as discussed previously in Section 5.3.1.

Figure 5.6C shows the thickness comparison between the CT and reconstructed images. There are visually distinct sections where the average thickness levels are different. The sections have distinct break points at Record 60 (x = 0.08m) and 160 (x = 0.19m), where there are few outliers in their neighbourhoods. These outliers should be neglected for thickness estimates as their values deviating far from the norms. Figures 5.7C and 5.8C show the reconstructed interfaces for the cervine and ovine samples, which are smoother and more continuous laterally. The thickness comparison is better and closer than the bovine's comparison.

Among all three samples, the cervine sample yields the best estimation for cortical thickness. As previously mentioned in Section 5.2.3, the possible reason is that the top cortical thickness of the cervine sample is relatively uniform and its

surface is flat. The good coupling between the transducers and the bone surface and the structural homogeneity of the bone sample allow better energy transmission and reflection.

For all inversion results, there are edge artifacts occurring at the both ends. In those areas, large errors exist between the estimated thickness from the reconstructed images and CT images. It may be caused by two factors: larger curvature of the interfaces at the ends of the samples and the presence of cancellous bone at the ends. The latter reduces the homogeneity of the samples, making the assumption of uniform velocity model deviating from the actual bone structure.

Therefore, when estimating the cortical thickness from the reconstructed images, one should avoid using the portion of the image either at the ends or the discontinuous locations. The part of the image corresponding to the mid-shaft of bone sample should be more appropriate.

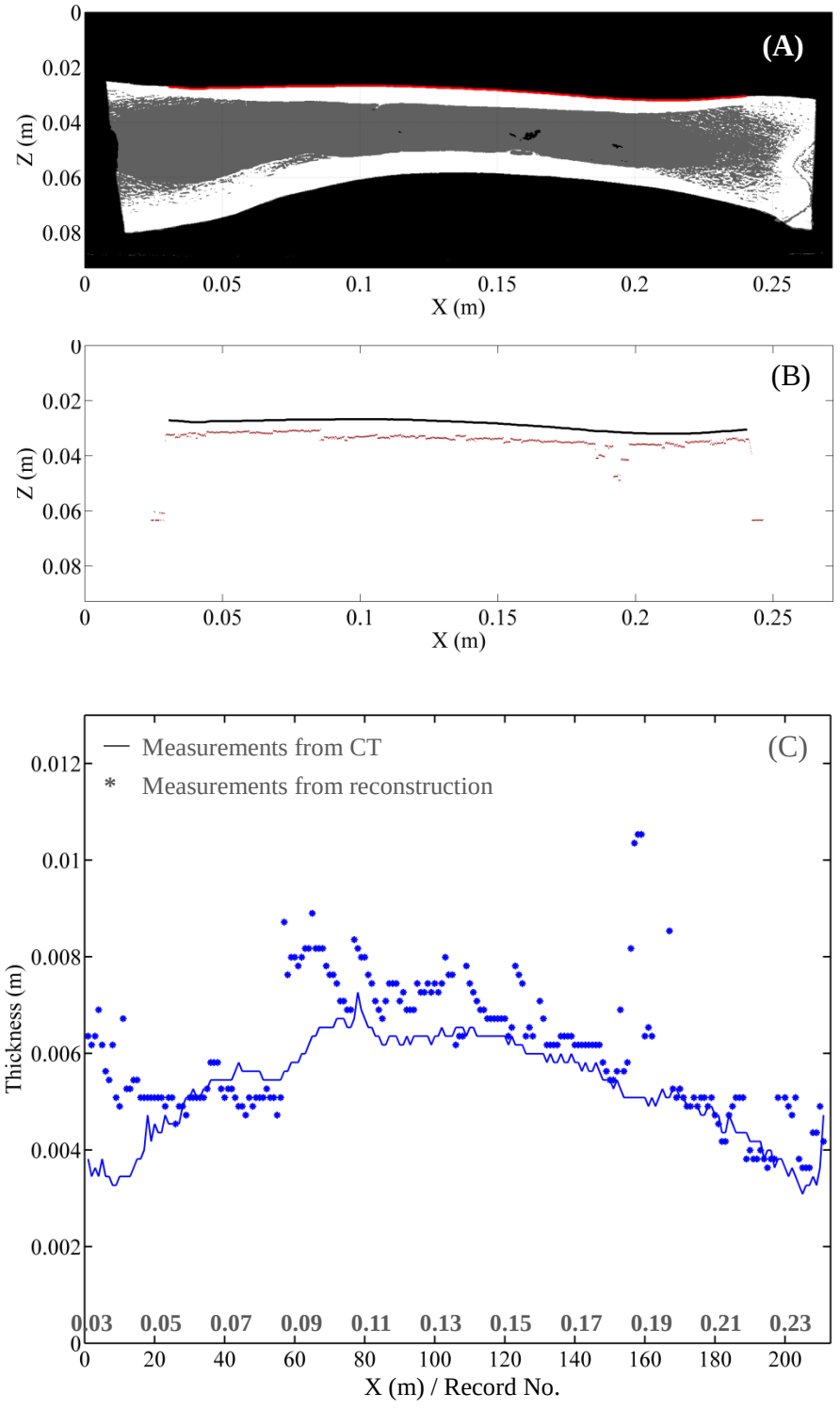

Figure 5.6 The inversion results for the bovine sample: (A) a CT image with source/receiver configurations. The red line indicates the S/R pair locations; (B) the inversion result of the first cortical layer with the black line indicating the bone surface; (C) thickness comparison between the measurements from the CT image and the reconstructed image.

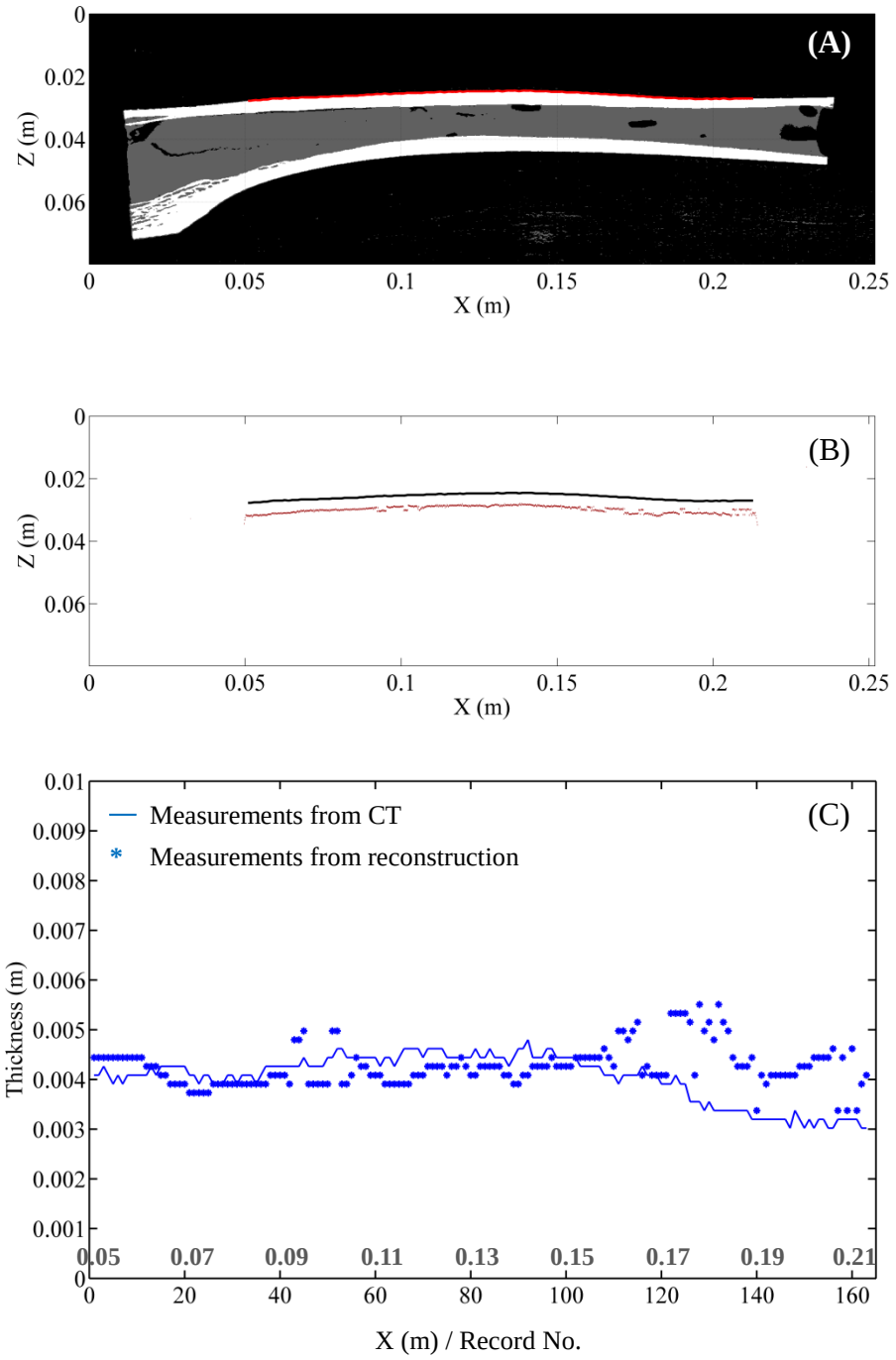

Figure 5.7 The inversion results for the cervine sample: (A) a CT image with source/receiver configurations. The red line indicates the S/R pair locations; (B) the inversion result of the first cortical layer with the black line indicating the bone surface; (C) thickness comparison between the measurements from the CT image and the reconstructed image.

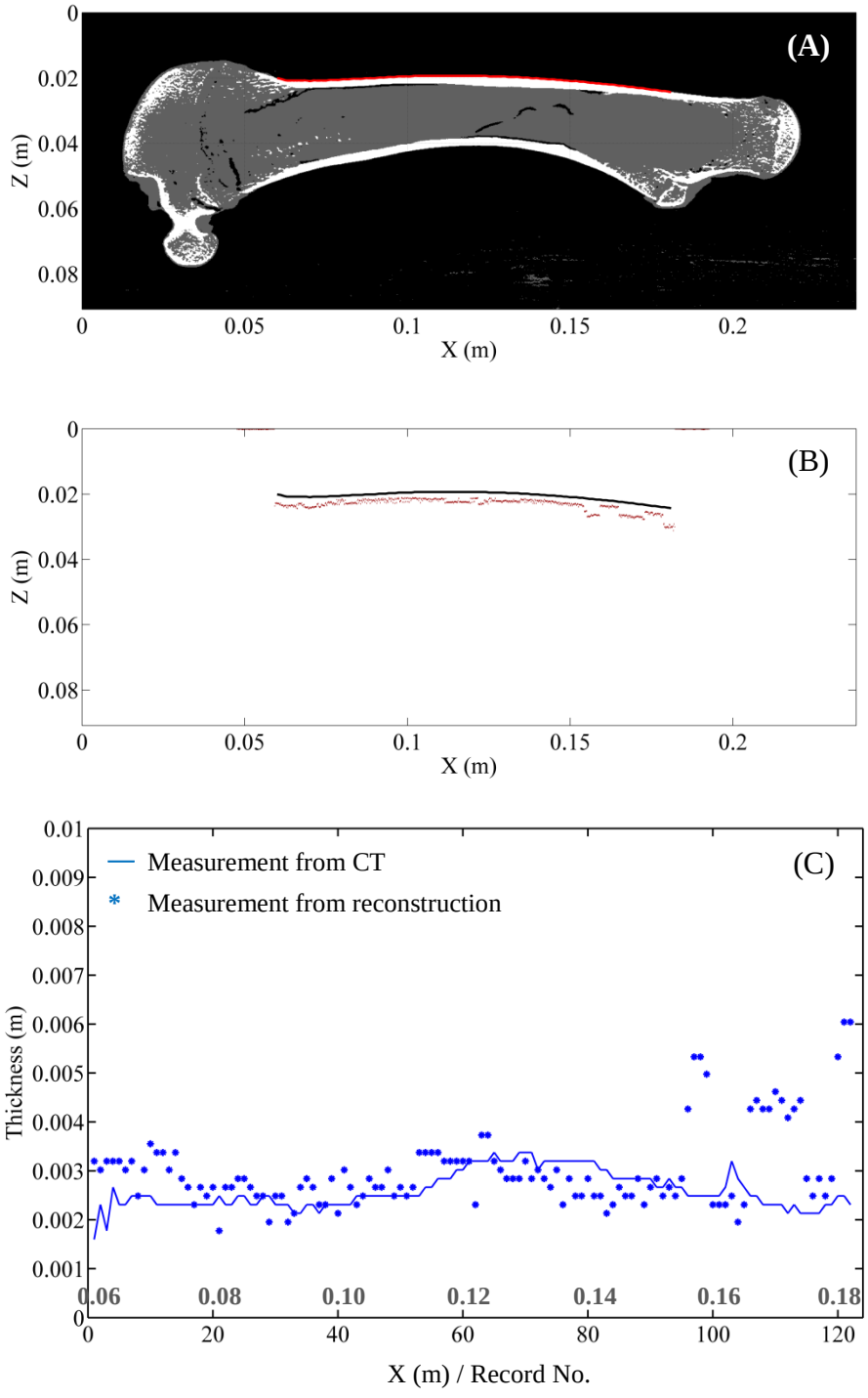

Figure 5.8 The inversion results for the ovine sample: (A) a CT image with source/receiver configurations. The red line indicates the S/R pair locations; (B) the inversion result of the first cortical layer with the black line indicating the bone surface; (C) thickness comparison between the measurements from the CT image and the reconstructed image.

5.3.3.2 Mean thickness measurement and comparison

Figures 5.6C, 5.7C and 5.8C show the point-by-point comparison between the estimated and CT-based thickness at all source/receiver positions. To compare the measurement quantitatively, the mean thickness is calculated by taking the average of the thickness values of a specific number of S/R positions.

Here we define two mean thickness estimates: total mean thickness (TMT) and sectional mean thickness (SMT). TMT uses thickness measurements at all S/R positions. In case the measurements have outliers, the TMT value does not have significant meaning but does offer a quick estimate. SMT is a more meaningful and reliable estimate as it only uses a smaller number of S/R positions when the reconstructed interfaces are not smooth and excludes outliers for the estimation.

Table 5.3 tabulates the mean thickness estimates for the three samples. Expectedly, the TMT errors are larger than the SMT errors. The TMT always has larger errors with large standard deviations for the following two main reasons. First, the estimate uses thickness measurements for a very far range, i.e., the first S/R position is very far away from the last S/R position; the cortex might not be heterogeneous laterally for that distance. Secondly, the estimate uses all thickness measurements even though some of the measurements are not reliable, i.e., outliers. As shown in Table 5.3, most SMT estimates are close to the corresponding CT-based mean thickness. The absolute relative errors between these two mean thickness values are as low as 1.9%, 4.6% and 3.2% for the bovine, cervine, and ovine samples respectively. Therefore the sectional mean is a more reliable and robust parameter to estimate the average thickness of the cortical layer.

As expected, the cervine sample shows the least TMT error of 7% among the three samples. There are more than 30% errors for bovine and ovine samples because the thickness measurements vary greatly along the acquisition distance. Thus choosing a uniform section in the reconstructed image is important for accurate thickness estimate. The cervine sample also has a flatter bone surface and a smoother reconstructed interface, which consequently provides more accurate cortical thickness estimate.

For the bovine sample, the SMT measurement includes three zones delineated by Record 21 - 60, Record 81 - 150 and Record 171 -190 respectively. The first zone (between Record 21 and 60) has the best SMT of 5.4 mm with 1.9% error. The small error in this zone can be attributed to the fact that the cortical velocity was estimated and calculated in the same zone. While one can assume the homogeneity of the bone tissues at smaller measuring distance, the bone tissues can be inhomogeneous at large distances. The cortical velocities vary slightly along the long axis. This can lead to error or inaccuracy in thickness estimation where positions at which the velocity and thickness estimation are far apart. To improve the accuracy of the results, the procedures of velocity estimation and thickness measurement should be performed in the same zone of bone samples. For the other two (cervine and ovine) samples, these procedures were followed in the experiments, and thus better estimates of the cortical thickness were obtained with a good comparison to the CT-based measurements.

The bovine, cervine and ovine bone samples used have average cortical thickness of 5 mm, 4 mm and 3 mm respectively. It has been shown that a cortical thickness of less than 4 mm in humerus bones will indicate a low BMD (Tingart *et al*, 2003). The cortical thickness measurement from the reconstructed images in this study reveals possible potential to estimate thin cortex for osteoporosis.

Table 5.3 Comparison of mean thickness for the three bone samples.

Bone Type	Total mean thickness (mm)			Sectional mean thickness (mm)			
	CT-based mean	Estimate[1]	Absolute Relative Error[2]	Record No. used	CT-based mean	Estimate	Absolute Relative Error
Bovine (Sample 1)	5.3±1.0	7.2±6.5	35.9%	21 - 60	5.3±0.4	5.4±1.0	1.9%
				81 - 150	6.2±0.3	7.4±4.6	19.4%
				171 - 190	4.6±0.3	4.8±0.4	4.4%
Cervine (Sample 2)	4.0±0.5	4.3±0.4	7.5%	40 - 110	4.4±0.2	4.2±0.3	4.6%
Ovine (Sample 3)	2.6±0.4	3.6±0.8	38.5%	61 - 90	3.1±0.2	3.2±0.4	3.2%

[1]The estimates are measured from the reconstructed images.

[2]The absolute relative error is calculated by dividing the absolute difference between the estimated and CT-based value by CT-based value.

5.4 Full inversion of long bone structure

In this section, I use one of the real bone data sets, the bovine tibia data set (Sample 4) to invert for all of its interfaces: cortical/marrow, marrow/cortical and cortical/air. Distorted Born approximation with a variable background velocity is used.

5.4.1 Inversion analysis and processing

The data was processed following the procedures described in Section 4.3.1 and Section 5.3.1 to improve the signal-to-noise ratio and enhance the echoes of the recorded signals. After the triggers were removed from the original data, the signals were decimated with a time interval of 0.05 μs. A bandpass filter of 0.3/0.5/2.0/2.5 MHz was applied to all records to remove the low and high frequency components. The multiple reflections from the first interface (cortical/marrow) were muted. Time gain compensation was applied to increase the amplitude of late-arriving reflection signals from other interfaces in the lower part of the bone sample. Further the major reflections, which will be used for inversion, were singled out by a 71-point Hamming window. As discussed in previous section, interpolation was also used to replace any bad record and reduce spacing interval by inserting records in between. The number of records was increased from 198 to 395 records in this case, to improve image quality of the reconstructed images.

Figure 5.9 shows portion of the time signals before (Figure 5.9A) and after processing (Figure 5.9B). The reflection responses from the two lower interfaces (marrow/cortical and cortical/air) could be seen after time gain compensation. Figure 5.10A illustrates the CT image of the bone sample. Due to the long

preservation time, the bone sample was dehydrated and there were large cavities in the marrow close to the right end of the bone sample. Under this circumstance, ultrasound wave can hardly penetrate further in the bone structure, and therefore, there were very little responses at the latter part of the signal beyond x = 0.16m as seen in Figure 5.9B. Simultaneously, the presence of cancellous bone close to epiphyses greatly attenuated ultrasound waves so the waves couldn't travel longer distance. These factors will influence the inversion results, which will be discussed later.

Similar inversion parameters were selected as those used in Section 5.3.2. The beam aperture was $\pm 5^\circ$ and the frequency range for inversion used was set from 0.3 to 2.5 MHz. The number of data points for each record was 1799. The dimension of image matrix was 155×512 with 0.5 mm pixel size. After interpolation, the number of record was 395. The DLSCG method was used with 4 and 10 for the regularization parameter and iteration number respectively. The SOS for cortical bone was still assigned as 3441m/s, 1434 m/s for marrow, and 0 for air. The same tables of ray tracing results used in Section 4.3 and 4.4 were recalled to provide the travelled distance and travelling time estimates.

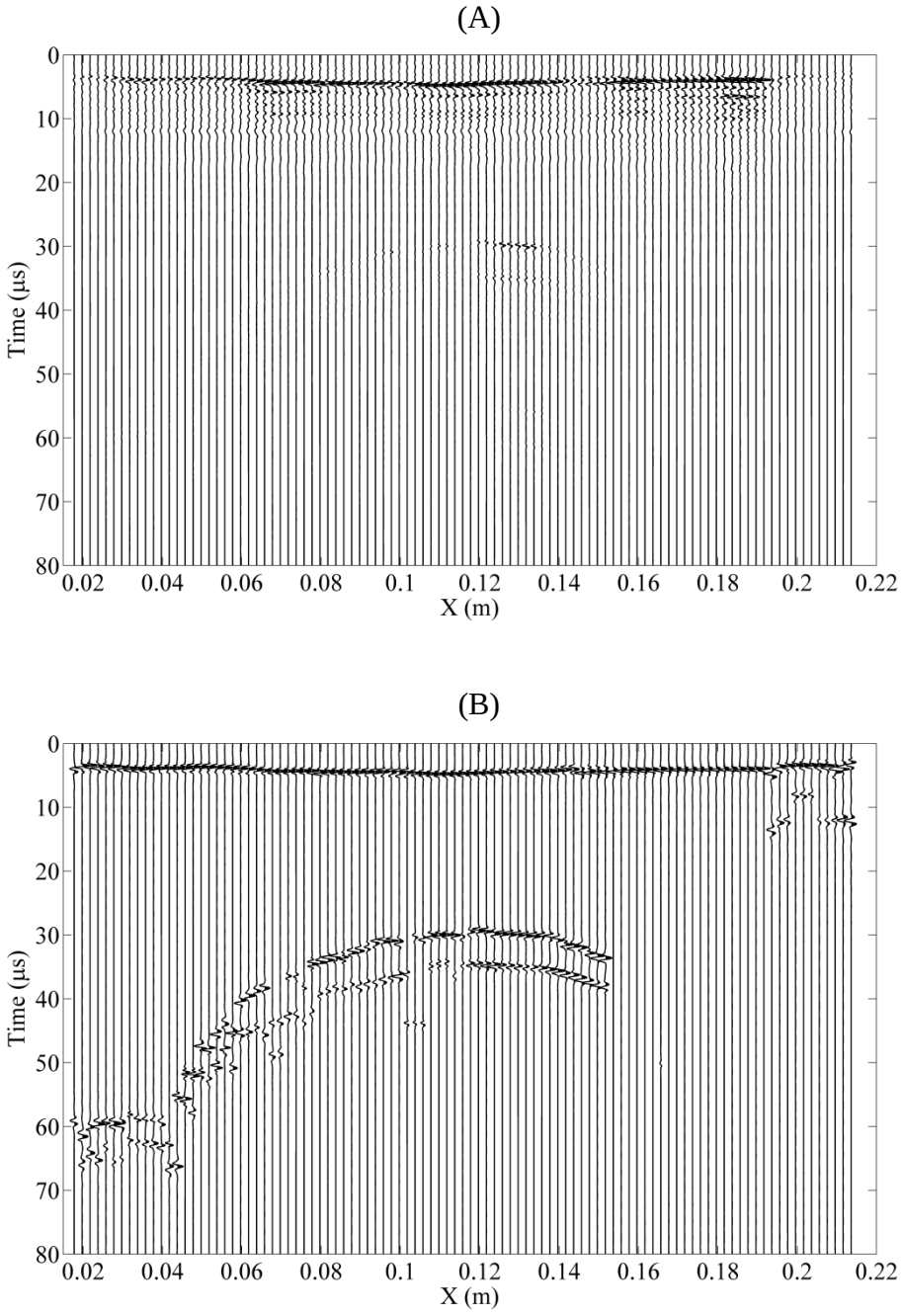

Figure 5.9 Experimental data of bovine tibia bone (Sample 4): (A) a section of the original time signals; (B) the same section of the records after processing. The records are self-normalized.

5.4.2 Inversion results and discussions

Figure 5.10B shows the reconstructed image using the data set shown in Figure 5.9B. In the figure, the red points indicate the pixel values of the reconstructed interfaces and the blue solid lines are the best-fitted seven-order polynomial curves for the three interfaces. Figure 5.10C shows the reconstructed interfaces superimposed on the original CT-converted velocity model. To emphasize the interfaces, the CT-converted velocity model instead of the CT image was used for the comparison.

Among the three, the first cortical/marrow interface is faithfully reconstructed. The interface is continuous and smooth and almost overlaps with the corresponding interface in the converted velocity model.

For the other two interfaces, the reconstructed interfaces are made up of largely dispersive dots, and the contour of the interfaces can only be identified with the aid of imaging enhancement techniques. The curve-fitting is only effective in the range where the true inversion results can be achieved. The agreement is also less favourable comparing to the first cortical/marrow interface. The agreement is better in the middle part of the image where the curvature of the bone structure is minimal. Toward the left, the structure curves sharply and the agreement is poor.

There are at least three main reasons for the misfit. The first two reasons have been discussed in Section 4.4 where I analyzed a full inversion of a simulated data set. I will repeat them here. First, part of the discrepancy arises from the replacement of a true velocity profile by its smooth version for ray tracing. Smoothing a velocity model will introduce small inaccuracy to the model itself but the accumulated error to the calculated travelling times and distances can

be large when the travelled distances are longer, especially for the deeper structures. Therefore the lower interfaces are not imaged accurately. Secondly, a homogeneously-layered model is used for an inhomogeneously-layered bone structure. The discrepancy between the model and the real bone samples due to existence of cancellous bone and curved interfaces will influence the accuracy of the interface reconstruction. Lastly, the presence of material absorption, air cavities, and scattering due to heterogeneities and curved interface in the real data will decrease the SNR of the recorded signals.

The best fitted curves thus obtained can only be a rough estimate of the interfaces. In reality, the amplitudes of scattered signals recorded by the transducer in the zero-offset case are very small. The reconstruction will never be expected in area below these curved interfaces. If there is any, the results will not be trustworthy.

Due to the influences of large cavities in the structure and cancellous bone, the lower interfaces in the right part of image were not successfully reconstructed. Although the cavities will not appear in human bone in *vivo*, other interferences, such as soft tissue, blood vessels in marrow, can decrease the amplitude intensity of the signals and generate similar effects as observed in this experiment.

In summary, it is difficult to faithfully reconstruct the lower interfaces of the bone sample. The energy strength of the echo from those interfaces is usually weak or nonexistent and thus, the signal-to-noise ratio is lower. Nevertheless, the first cortical/marrow interface can be well reconstructed, which enables us to estimate the cortical thickness.

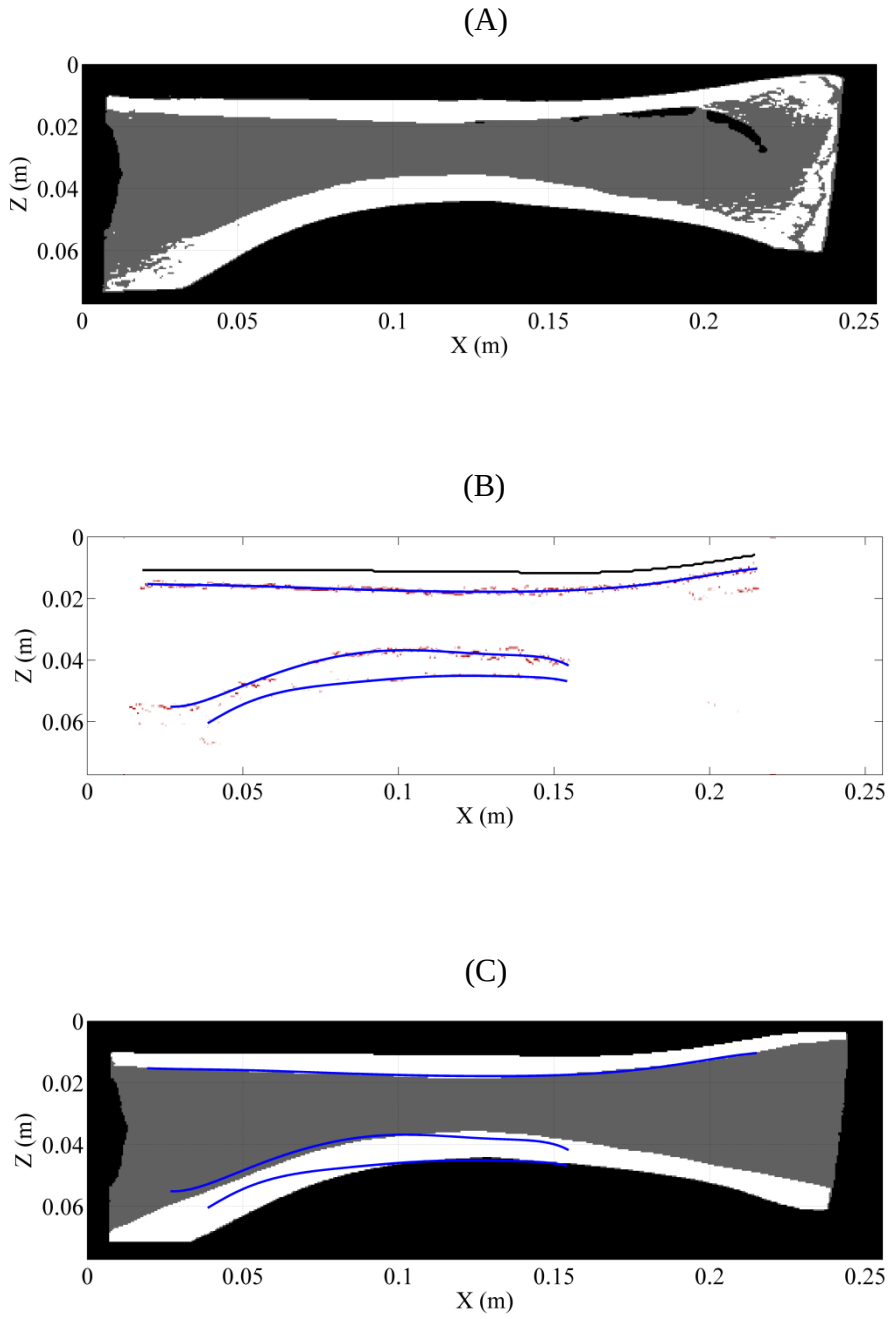

Figure 5.10 Full inversion of the bovine tibia bone (Sample 4): (A) a CT image; (B) the reconstructed interfaces with the best-fitted curves for the interfaces; (C) the velocity bone model (constructed from (A)) with the best-fitted curve superimposed.

Chapter 6

Conclusions

A set of ultrasound imaging algorithms and procedures based on the Born scattering theory was developed to image the internal structures of long bones such as femur and tibia. The inversion methodologies were applied to image bone data from simulation and real animal bone samples and to estimate the top cortical thickness from the reconstructed images. The cortex thickness is one of the important parameters for osteoporosis diagnosis.

Three major topics were discussed in the thesis: (1) the feasibility and robustness of the algorithms and the selection of the inversion parameters; (2) the cortical thickness estimation using the inversion methods based on the constant background velocity; (3) the full reconstruction of the long bones based on distorted Born method using variable background velocity model.

Acoustical wave equation was used in the formalism. The assumption is valid because (1) the acquisition is the zero-offset configuration where the source and receiver are at the same location, (2) the interfaces are almost parallel, especially in the mid-shaft of the bone sample, and (3) the received signals mainly consist of strong longitudinal waves. The inversion algorithms and methods were validated by applying the operations to simulated data sets generated by the forward operator (using bovine femur model), convolution, and finite-difference full wave solution (using the bovine tibia model). The difference between the synthetic data and predicted data is very insignificant.

Signal processing play an important role prior to inversion. Proper

processing steps can greatly increase the signal-to-noise ratio of the signal, enhance the the quality of reconstructed images and reduce computation effort. Based on this study, decimation is required to reduce the temporal sampling rate and thus the number of data points. Bandpass filters should be used to remove the unwanted low and high frequency components. Gain compensation enhances the echo strength from the deeper structures of the bone samples. Hamming filter windows the primary pulses and selects them for inversion purpose. The interpolation procedure replaces bad records and inserts interpolated records to reduce spatial interval.

Proper selection of inversion parameters is an important step to achieve good reconstructed results. Signal length or number of data points determines the frequency sampling interval, Δf, and should be long enough so that Δf is not too coarse, compromising the image quality. Small aperture around $\pm 5\text{-}10\,^{\circ}$ is enough to provide more pixels for the reconstruction without incurring significant computation cost and inclusion of other scattered energies. Smaller pixel size yields better resolution of the reconstructed images but might negatively affect image contrast. Therefore a compromise among the image resolution, image quality, and computation effort should be reached when the pixel size and temporal sampling rate are determined. Finally, the damped least squares method with conjugate gradient implementation (DLSCG) is suitable for long bone imaging because it considers minimization of both the data misfit and model norm, thus providing some degrees of smoothness to the reconstructed solutions.

Accurate estimation of cortical velocity is important to building a good background velocity model for the inversion. The cortical velocity can be estimated using the offset axial transmission method. Data should be acquired on a visually flat bone surface and in the mid-shaft of the bone samples. The method

relies on picking the FAS signals. Proper wedge angle will provide the best signal discrimination. For our data set, 60° wedge angle was our choice. Usually, ten to fifteen records are reasonable for linear regression. The errors between the estimated SOS and CT-based velocity are as low as 1.4%, 5.0%, and 3.6% for three different long bone samples, respectively.

The structural properties can greatly influence the inversion results, thus affecting the measurement of cortical thickness. The procedures of velocity estimation and thickness measurement should be advisedly performed in the approximate location of bone samples. Lateral discontinuities might happen across the reconstructed interfaces. The mean thickness is a good index to assess the cortical thickness and should be evaluated within a segment where the thickness values do not change significantly. Visual inspection of smoothness of the reconstructed interfaces will provide a good quality control to pick the range of records used for sectional mean thickness (SMT) estimate. The estimated SMT values are close to the CT-based measurements with discrepancies of 1.9%, 4.6% and 3.2% for bovine, cervine and ovine samples respectively. Therefore the SMT is a more reliable and robust parameter to estimate the thickness of bone cortex.

In comparison with the top cortex/marrow interface, the reconstruction of the lower interfaces (marrow/cortex and cortex/air) interfaces are less fortunate. This is mainly caused by lower signal strength due to longer distances travelled and larger curvatures. These two factors lead to the severe refractions and attenuation along the wave propagating paths and thus weaken the recorded echoes. Another factor is due to the intrinsic assumption of the Born-based methodology, which requires a smooth velocity background. Therefore, velocity-smoothing will create inaccuracy to the calculated travelling times and distances.

In summary, the proposed imaging method is a promising tool to estimate top cortical thickness with good accuracy. The average values of cortical thickness, thus recovered in this thesis, are around 5 mm, 4 mm and 3 mm corresponding to bovine, cervine and ovine samples respectively. The precision of the thickness estimation can be as good as 0.1 mm. Cortex thickness is highly related with the bone quality in the proximal diaphysis (Tingart *et al,* 2003). The cortical thickness measurement based on the ultrasound reconstructed images reveals possible potential to estimate small cortical thickness during osteoporosis.

The ultrasound imaging method presented in this thesis is novel in the area of bone imaging. There are mainly two groups engaging in this type of ultrasound imaging research in hard tissues: one led by Dr. Lasaygues in CNRS of Marseilles, France and one by Dr. Le in the University of Alberta, Edmonton Canada (this group). While two groups used similar Born-based scattering and inversion methods to invert for bone internal structures, the acquisition configuration and thus the nature of data set are different. Dr. Lasaygues focuses on tomographic configuration with the transducers deployed around the long bone sample. This group focuses on the axial transmission configuration where the transducers deployed collinearly on one side of the bone surface. The method has the potential to provide tissue parameter estimation in the pixel scale rather than the global estimation by the conventional ultrasound techniques. However, our study is still focused on the theoretical and limited *in vitro* studies and far behind the clinical application for the diagnosis of osteoporosis.

There are at least four identified areas which should be considered in future studies to improve the imaging methods.

1. Data acquisition: the current acquisition method relies on moving a transducer manually from one position to another and is not suitable for clinical

study. A linear array with 64 - 128 transducer elements should be considered. This will speed up the acquisition time significantly and reduce patient motion artifacts. In addition, the array transducer can decrease the measurement range to 5-8 cm while keeping sufficient number of signals, which will increase the spatial acquisition sampling rate and thus improve the image quality. However, since the transducer elements will function simultaneously, the interference during wave propagation needs to be considered in the imaging algorithms.

2. Soft-tissue artifacts: The effect of overlying soft tissues should have influence on the cortex/marrow reflected signals, and further signal processing will be the main focus to distinguish the reflection echoes from different interfaces. For the offset axial transmission data, the soft tissue will affect the picking of the FAS signals. In this case, the head wave might be a solution for the cortical velocity estimation. This is an important area which needs careful research effort.

3. Implementing the Edge-Preserving Regularization constraints will improve the sharpness of the reconstructed interfaces and thus provide a better estimation for interface position and cortical thickness. This constraint will also be useful to image fractures.

4. Programming and computation: Matlab programming is a drawback for the computing speed. The processing time will be greatly decreased when other languages such as C++, FORTRAN are used for the signal processing and reconstruction. A work station instead of a desktop PC will improve the computation efficiency. The real-time measurement including data acquisition and analysis, image reconstruction and thickness assessment in less than 10 minutes is possible to fulfill the clinical diagnostic needs.

Reference

Aster R C, Borchers B and Thurber C H, 2005, *Parameter estimation and inverse problems*, Elservier Inc, Chapter 4 and 6.

Baran D T, Kelly A M, Karellas A, Gionet M, Price M, Leahey D, Steuterman S, Mcsherry B, Roche J, 1988, Ultrasound attenuation of the Os calcis in women with osteoporosis and hip fracture, *Calcif Tissue Int*, **43**, 138-142.

Barnett E and Nordin B E C, 1960, The radiological diagnosis of osteoporosis: A new approach, *Clinical Radiology*, **11(3)**, 166-174.

Beylkin G, 1985, Imaging of discontinuities in the inverse scattering problem by inversion of a causal generalized Radon transform, *Journal of Mathematical Physics*, **26(1)**, 99-108.

Beylkin G and Burridge R, 1990, Linearized inverse scattering problems in acoustics and elasticity, *Wave Motion*, **12(1)**, 15-52.

Beylkin G, Oristaglio M and Miller D, 1985, Spatial resolution of migration algorithms, *Acoustical Imaging*, **14**, 155-168.

Bhatia R, *Matrix Analysis*, Springer,1996.

Bloom R A, 1980, A comparative estimation of the combined cortical thickness of various bone sites, *Skeletal Radiology*, **5(3)**, 167-170.

Bloom R A and Laws J W, 1970, Humeral cortical thickness as an index of osteoporosis in women, *Br J Radiol*, **43(512)**, 522-527.

Bonnick S L and Lewis L A, 2002, *Bone densitometry for technologists*, Human

Press Inc.

Bossy E, Talmant M and Laugier P, 2002, Effect of bone cortical thickness on velocity measurements using ultrasonic axial transmission: A 2D simulation study, *The Journal of the Acoustical Society of America*, **112(1)**, 297-307.

Bossy E, Talmant M and Laugier P, 2004, Three-dimensional simulations of ultrasonic axial transmission velocity measurement on cortical bone models, *The Journal of the Acoustical Society of America*, **115(5)**, 2314-2324.

Brekhovskikh L M, 1980, *Waves in layered media*, Academic press Inc..

Bumrerraj S and Katz J L, 2001, Scanning Acoustic Microscopy Study of Human Cortical and Trabecular Bone, *Annals of Biomedical Engineering*, **29(12)**, 1034-1042.

Camus E, Talmant M, Berger G, Laugier P, 2000, Analysis of the axial transmission technique for the assessment of skeletal status, *J. Acoust. Soc. Am*, **108(6)**, 3058-3065.

Castriota-Scanderbeg E and Dallapiccola B, 2005，*Abnormal skeletal phenotypes: from simple signs to complex diagnoses*, Springer.

Chaffai S, Padilla F, Berger G, Laugier P, 2000, In vitro measurement of the frequency-dependent attenuation in cancellous bone between 0.2 and 2 MHz, *J. Acoust. Soc. Am*. **108(3)**, 1281-1289.

Chaffa S, Peyrin F, Nuzzo S, Porcher R, Berger G and Laugier P, 2002, Ultrasonic characterization of human cancellous bone using transmission and backscatter measurements: relationships to density and microstructure, *Bone*, **30(1)**, 229-237.

Chappard C, Laugier P, Fournier B, Roux C, Berger G, 1997, Assessment of the relationship between broadband ultrasound attenuation and bone mineral density at the calcaneus using BUA imaging and DXA, *Osteoporosis International*, **7(4)** , 316-322.

Claerbout J F, 1992, *Earth soundings analysis : processing versus inversion*, Blackwell Scientific Publications.

Devaney A J, 1983, A Computer Simulation Study of Diffraction Tomography, *Biomedical Engineering, IEEE Transactions on BME*, **30(7)**, 377-386.

Duric N, Littrup P, Babkin A, Chambers D, Azevedo S, Pevzner R, Tokarev M, Holsapple E, Rama O, and Duncan R, 2005, Development of ultrasound tomography for breast imaging: technical assessment, *Medical Physics*, **32(5)**, 1375-1386.

Duric N, Littrup P, Poulo L, Babkin A, Pevzner R, Holsapple E, Rama O, and Glide C, 2007, Detection of breast cancer with ultrasound tomography: first results with the Computed Ultrasound Risk Evaluation (CURE) prototype, *Medical Physics*, **34(2)**, 773-785.

EFFO and NOF, 1997, Who are candidates for prevention and treatment for osteoporosis? *Osteoporos Int*, **7**, 1-6.

Evans R A, McDonnell G D, Schieb M, 1978, Metacarpal cortical area as an index of bone mass, *Br J Radiol*, **51(606)**, 428-431.

Ewing W M, Jardetzky W S and Press F, 1957, *Elastic waves in layered media*, McGraw-Hill book company Inc..

Fung Y C, 1977, *A first course in continuum mechanics*, Prentice-Hall Inc..

Funke M, Kopka L, Vosshenrich R, Fischer U, Ueberschaer A, Oestmann J W, Grabbe E, 1995, Broadband ultrasound attenuation in the diagnosis of osteoporosis: correlation with osteodensitometry and fracture, *Radiology*, **194**, 77-81

Genant H K, Faulkner K G, Fuerst T, Gluer C C, 1996, 1996 Controversies in the diagnosis of osteoporosis, *82nd RSNA Scientific Annual Meeting* (Chicago, IL), 28.

Glide C, Duric N, Littrup P, 2007, Novel approach to evaluating breast density utilizing ultrasound tomography, *Medical Physics*, **34(2)**, 744-753.

Guillermin R, Lasaygues P, Sessarego J P and Wirgin A, 2001, Inversion of synthetic and experimental acoustical scattering data for the comparison of two reconstruction methods employing the Born approximation, *Ultrasonics*, **39(2)**, 121-131.

Greenleaf J F, 1983, Computerized tomography with ultrasound, *Proceedings of the IEEE*, **71(3)**, 330-337.

Greenleaf J F and Bahn R C, 1981, Clinical imaging with transmissive ultrasonic computerized tomography, *IEEE Trans Biomed Eng*, **28(2)**, 177-185.

Hakulinen M A, Day J S, Toyras J, Weinans H, Jurvelin J S, 2006, Ultrasonic characterization of human trabecular bone microstructure, *Phys. Med. Biol.* 51, 1633-1648

Hansen Per C, 1998, *Rank-deficient and discrete ill-posed problems*, SIAM.

Hasegawa K, Turner C and Burr D, 1994, Contribution of collagen and mineral to the elastic anisotropy of bone, *Calcified Tissue International*, **55(5),** 381-386.

Hasegawa K, Turner C H, Recker R R, Wu E and Burr D B, 1995, Elastic properties of osteoporotic bone measured by scanning acoustic microscopy, *Bone*, **16(1)**, 85-90.

Hestenes M R and Stiefel E, 1952, Methods of conjugate gradients for solving linear systems, *Journal of Research of the National Bereau of Standards*, **49(6)**, 409-436.

Jacques P. Brown, R. G. J., and The Scientific Advisory Council of the Osteoporosis Society of Canada (2002), 2002, "2002 clinical practice guidelines for the diagnosis and management of osteoporosis in Canada." *CMAJ*. **167**(10), S1-S34.

Jenson F, Padilla F, Bousson V, Bergot C, Laredo J D, Laugier P, 2006, *In vitro* ultrasonic characterization of human cancellous femoral bone using transmission and backscatter measurements: Relationships to bone mineral density, *J. Acoust. Soc. Am*. **119(1)**, 654-663.

Johnell O and Kanis J A, 2006, An estimate of the worldwide prevalence and disability associated with osteoporotic fractures. *Osteoporos Int* **17**, 1726-1733.

Kak A C and Slaney M，*Principles of Computerized Tomographic Imaging*，IEEE Press, 1988，Chapter 3.

Katz J L and Meunier A, 1993, Scanning Acoustic Microscope Studies of the Elastic Properties of Osteons and Osteon Lamellae, *Journal of Biomechanical Engineering*, **115(4B)**, 543-548.

Klotzbuecher C M, Ross P D, 2000, Landsman P B, Abbott T A, Berger M, Patients with prior fractures have an increased risk of future fractures: a summary of the literature and statistical synthesis. *J Bone Miner Res* **15**, 721-739.

Langton C M, 1996, The clinical role of BUA for the assessment of osteoporosis: A new hypothesis. *Clinical Rheumatology*, **15(4)**, 414-415.

Langton C M, Ali A V, Riggs C M, Evans G P, Bonfield W, 1990, A contact method for the assessment of ultrasonic velocity and broadband attenuation in cortical and cancellous bone, *Clinical Physics and Physiological Measurement*, **11(3)**, 243-249.

Langton C M and Njeh C F, 2004, *The physical measurement of bone*, Institute of Physics Publishing.

Langton C M, Palmer S B, Porter R W, 1984, The measurement of broad-band ultrasonic attenuation in cancellous bone, *Eng Med* **13**, 89-91.

Lasaygues P, 2006, Assessing the cortical thickness of long bone shafts in children, using two-dimensional ultrasonic diffraction tomography, *Ultrasound in Med.& Biol* **32(8)**, 1215-1227.

Lasaygues P, 2007, Compound quantitative ultrasonic tomography of long bones using wavelet analysis, *Acoustical imaging*, 223-229.

Lasaygues P and Le Marrec L, 2008, Ultrasonic reflection tomography vs. canonical body approximation: experimental assessment of an infinite elastic cylindrical tube, *Ultrasonic Imaging*, **30(1)**, 29-43.

Lasaygues P and Lefebvre J P, 2000, Bone imaging by low frequency ultrasound reflection tomography, *Acoustical imaging*, **25**, 507-513.

Lasaygues P and Lefebvre J P, 2001, Cancellous and cortical bone imaging by reflected tomography, *Ultrasonic imaging*, **23**, 55-70.

Lasaygues P, Ouedraogo E, Gindre M, Talmant M, Laugier P and Lefebvre J P,

2004, Quantitative ultrasound tomography of long bones: distorted Born iterative process, *Acoustical imaging*, 555-561.

Lasaygues P, Ouedraogo E, Lefebvre J P, Gindre M, Talmant M and Laugier P, 2005, Progress towards *in vitro* quantitative imaging of human femur using compound quantitative ultrasonic tomography, *Physics in medicine and biology* **50**, 2633-2649.

Laugier P, 2006, Quantitative ultrasound of bone: looking ahead, *Joint Bone Spine*, **73(2)**, 125-128.

Lay T and Wallace T C, 1995, *Modern global seismology*, Academic Press INC.

Le L H., Gu J, Yu P. and Zhang C, 2010, Probing long bones with ultrasonic body waves, *Applied Physics Letter*, **96(11)**, 41021-3.

Lefebvre F, Deblock Y, Campistron P, Ahite D, Fabre J J, 2002, Development of a new ultrasonic technique for bone and biomaterials in vitro characterization, *J Biomed Mater Res (Appl Biomater)* **63**, 441-446.

Lin J D, Chen J F, Chang H Y, Ho C, 2001, Evaluation of bone mineral density by quantitative ultrasound of bone in 16862 subjects during routine health examination, *Br J Radiol*, **74(883)**, 602-606.

Lippmann, B A and Schwinger, J, 1950, Variational Principles for Scattering Processes. I. *Physical Review*, **79(3)**, 469-480.

Lobel P, Blanc-Fraud L, Pichot Ch and Barlaud M, 1997, A new regularization scheme for inverse scattering, *Inverse problems*, **13**, 403-410.

McDonald K, Little P, Pearcy M, Adam C, 2009, Relative Roles of Cortical and Trabecular Thinning in Reducing Osteoporotic Vertebral Body Stiffness: A

Modeling Study, *13th International Conference on Biomedical Engineering*, 1757-1760.

Menke W, 1989, *Geophysical Data Analysis: Discrete Inverse theory*, Academic Press Inc., Chapter 3.

Miller D, Oristaglio M, Beylkin G, 1987, A new slant on seismic imaging: Migration and Integral geometry, *Geophysics*, **52**, 943-964.

Moilanen P, Kilappa V, Nicholson P H F, Timonen J, Cheng S, 2004, Thickness sensitivity of ultrasound velocity in long bone phantoms, *Ultrasound in Med. & Biol*, **30(11)**, 1517-1521.

Moilanen P, Nicholson P H F, Kilappa V, Cheng S and Timonen J, 2006, Measuring guided waves in long bones: Modeling and experiments in free and immersed plates, *Ultrasound in Medicine & Biology*, **32(5)**, 709-719.

Moilanen P, Nicholson P H F, Kilappa V, Cheng S and Timonen J, 2007, Assessment of the cortical bone thickness using ultrasonic guided waves: Modelling and in vitro study, *Ultrasound in Medicine & Biology*, **33(2)**, 254-262.

Moilanen P, Talmant M, Bousson V, Nicholson P H F, Cheng S, Timonen J and Laugier P, 2007a, Ultrasonically determined thickness of long cortical bones: Two-dimensional simulations of in vitro experiments, *The Journal of the Acoustical Society of America*, **122(3)**, 1818-1826.

Moilanen P, Talmant M, Nicholson P H F, Cheng S, Timonen J and Laugier P, 2007b, Ultrasonically determined thickness of long cortical bones: Three-dimensional simulations of in vitro experiments, *The Journal of the Acoustical Society of America*, **122(4)**, 2439-2445.

Morse P M and Feshbach H, 1953, *Methods of theoretical physics Part.II*, McGraw-Hill Book Company Inc., 1064-1106.

Muller M, Moilanen P, Bossy E, Nicholson P H F, Kilappa V, Timonen J, Talmant M, Cheng S, Laugier P, 2005, Comparison of three ultrasonic axial transmission methods for bone assessment , *Ultrasound in Med. & Biol*. **31(5)**, 633-642.

Naghizadeh M and Sacchi M D, 2009, f-x adaptive seismic-trace interpolation, *Geophysics*,**74(1)**, V9-V16.

Nemeth, T, Wu, C, Schuster, G T, 1999, Least-squares migration of incomplete reflection data, *Geophysics*, **64**, 208-221.

Nicholson P H F, 2008, Ultrasound and the biomechanical competence of bone, *Ultrasonics, Ferroelectrics and Frequency Control, IEEE Transactions on*, **55(7)**, 1539-1545.

Nicholson P H F, Moilanen P, Karkkainen T, Timonen J and Cheng S, 2002, Guided ultrasonic waves in long bones: modelling, experiment and *in vivo* application, *Physiological Measurement*, **23(4)**, 755-768.

Nicholson P H F, Muller R, Cheng X G, Ruegsegger P, Van Der Perre G, Dequeker J, Boonen S, 2001, Quantitative ultrasound and trabecular architecture in the human calcaneus, *J. Bone Miner. Res.* **16(10)**, 1886-1892.

Ouedraogo E, Lasaygues P, Lefebvre J P, Talmant M, Gindre M and Laugier P, 2002, Multi-step compensation technique for ultrasound tomography of bone, *Acoustical imaging*, **26**, 153-160.

Parker R L, 1994, *Geophysical inverse theory*, Princeton University Press.

Papoulis A, and Chamzas C, 1979, Improvement of range resolution by spectral extrapolation, *Ultrasonic Imaging*, **1(2)**, 121-135.

Pratt R G, Huang L, Duric N and Littrup P, 2007, Sound-speed and attenuation imaging of breast tissue using waveform tomography of transmission ultrasound data, *Medical Imaging 2007: Physics of Medical Imaging, San Diego, CA, USA, SPIE*, **V6510**, 65104S-12

Protopappas V C, Fotiadis D I and Malizos K N, 2006, Guided ultrasound wave propagation in intact and healing long bones, *Ultrasound in Medicine & Biology*, **32(5)**, 693-708.

Raum K, ReiBauer J and Brandt J, 2004, Frequency and resolution dependence of the anisotropic impedance estimation in cortical bone using time-resolved scanning acoustic microscopy, *Journal of Biomedical Materials Research Part A* **71A(3)**, 430-438.

Riggs B L, Melton L J III, Robb R A, Camp J J, Atkinson E J, Peterson J M, Rouleau P A, McCollough C H, Bouxsein M L and Khosla S, 2004, Population-based study of age and sex differences in bone volumetric density, size, geometry, and structure at different skeletal sites, *Journal of Bone and Mineral Research*, **19(12)**, 1945-1954.

Ricker N, 1953, The form and laws of propagation of seismic wavelets, *Geophysics*, **18(1)**, 10-40.

Rocca F and Woodward M J, 1987, Wave-equation Tomography: II, *Stanford Exploration Project Report*, **57**, 25–47.

Shannon C E, 1998, Communication in the presence of noise, *Proc. Institute of Radio Engineers*, 37(1), 1949, 10–21. Reprint as classic paper in: *Proc. IEEE*,

86(2), 447-457.

Shearer P M, 1999, *Introduction to seismology*, Cambridge university press, 36-38.

Siffert R S, Kaufman J J, 2007, Ultrasonic bone assessment: “The time has come”, *Bone*, **40**, 5-8.

Spitz S, 1991, Seismic trace interpolation in the F-X domain, *Geophysics*, **56(6)**, 785-794.

Strelitzki R, Metcalfe S C, Nicholson P H F, Evans J A, Paech V, 1999, On the ultrasonic attenuation and its frequency dependence in the os calcis assessed with a multielement receiver, *Ultrasound in Med. & Biol.* **25(1)**, 133-141.

Ta D, Huang K, Wang W and Wang Y, 2005, Predict Ultrasonic Backscatter Coefficient in Cancellous Bone by Theory and Experiment, *IEEE-EMBS 27th Annual International Conference of the Engineering in Medicine and Biology Society*, Shanghai, China, 1131-1134.

Taylor J R, 1952, *Scattering theory*, John Wiley & Son, Inc.

Tingart M J, Apreleva M, von Stechow D, Zurakowski D, Warner J J P, 2003, The cortical thickness of the proximal humeral diaphysis predicts bone mineral density of the proximal humerus, *J Bone Joint Surg Br*, **85-B(4)**, 611-617.

Tortora G J and Grabowski S R, 1993, *Principles of anatomy and physiology*, HarperCollins College Publisher.

Toyras J, Nieminen M T, Kroger H, Jurvelin J S, 2002, Bone mineral density, ultrasound velocity, and broadband attenuation predict mechanical properties of trabecular bone differently, *Bone*, **31(4)**, 503-507.

Virtama P. and Mahonen H, 1960, Thickness of the Cortical Layer as an Estimate of Mineral Content of Human Finger Bones, *Br J Radiol*, **33(385)**, 60-62.

Virtama P and Kallio E, 1961, Bone pattern in experimental osteoporosis of the rat: Roentgenologic studies, *Ann Med Exp Biol Fenn*, **39**, 154-164.

Virtama P and Telkka A, 1962, Cortical thickness as an estimate of mineral content of human humerous and femur, *Br J Radiol*, **35**, 632-633.

Wang S F, Chang C Y, Shih C and Teng M M, 1997, Evaluation of tibial cortical bone by ultrasound velocity in oriental females, *Br J Radiol*, **70(839)**, 1126-30.

Waters, K R, Hughes M S, Mobley, J, Brandenburger G H, Miller J G, 2000, On the applicability of Kramers-Kronig relations for ultrasonic attenuation obeying a frequency power law, *J Acoust Soc Am*, **108(2)**, 556-63.

Wear K A, 1999, Frequency dependence of ultrasonic backscatter from human trabecular bone: Theory and experiment, *The Journal of the Acoustical Society of America*, **106(6)**, 3659-3664.

Wear K A, 2000, Temperature dependence of ultrasonic attenuation in human calcaneus, *Ultrasound in Med. & Biol*. **26(3)**, 469-472.

Weglein A B, 1982, Multidimensional seismic analysis: migration and inversion, *Geoexploration*, **20**, 47-60.

Werner P, 2005, Knowledge about osteoporosis: assessment, correlates, and outcomes, *Osteoporosis Int.***16**, 115-127.

Wuster C, Hadji P, 2001, Use of quantitative ultrasound densitometry (QUS) in male osteoporosis, *Calcif Tissue Int*. **69**, 225-228.

Yilmaz O, 1987, *Seismic data processing*, Society of Exploration Geophysicists.

Young H, Howey S, Purdie D W, 1993, Broadband ultrasound attenuation compared with dual-energy X-ray absorptiometry in screening for postmenopausal low bone density, *Osteoporosis International*, **3(3)**, 160-164.

Youzwishen C F, 2001, *Non-linear sparse and blocky constraints for seismic inverse problems* (MSc), University of Alberta, Edmonton, Canada.

Youzwishen C F and Sacchi M D, 2006, Edge Preserving Imaging, *Journal of Seismic Exploration*, **15(4)**, 45-58

Zheng R, Le L H, Sacchi M D, Ta D, Jar, B P Y and Lou E, 2007, Spectral Ratio Method to Estimate Broadband Ultrasound Attenuation of Cortical Bones Using Multiple Reflections, *Phys. Med. Biol*. **52**, 5855-5869.

Zheng R, Le L H, Sacchi M D, and Lou E, 2009, Broadband Ultrasound Attenuation Measurement of Long Bone Using Peak Frequency of the Echoes, *submitted to IEEE Transaction on Ultrasonics, Ferroelectrics, and Frequency Control*, **56(2)**, 396-400.

Zimmerman M C, Prabhakar A, Chokshi B V, Budhwani N and Berndt H, 1994, The acoustic properties of normal and imbedded bovine bone as measured by acoustic microscopy, *Journal of Biomedical Materials Research*, **28(8)**, 931-938.